Deformation Behavior of Tungsten Single Crystals During Wedge Nanoindentation - a Numerical Study

Zur Erlangung des akademischen Grades eines

DOKTORS DER INGENIEURWISSENSCHAFTEN (Dr.-Ing.)

von der KIT-Fakultät für Maschinenbau des

Karlsruher Instituts für Technologie (KIT)

angenommene

DISSERTATION

von

M.Sc. Tillmann Volz

Tag der mündlichen Prüfung:	19.05.2020
Hauptreferent:	Prof. Dr. rer. nat. Oliver Kraft
Korreferentin:	Prof. Dr. mont. Sabine M. Weygand

Abstract

The present work aims at the numerical investigations on the plastic deformation behavior of tungsten single crystals on the microscale, based on finite-element (FE) wedge nanoindentation simulations. These numerical studies on plasticity of body-centered cubic materials in the range of nanometers to few micrometers require not only an incorporation of a crystal plasticity model to describe slip dominated plastic deformation in the FE-simulations but moreover, the consideration of geometrically necessary dislocations (GND) and non-Schmid effects. Thus, an existing crystal plasticity model was extended to determine gradients of plastic shear and non-Schmid effects for the implementation of enhanced FE-simulations of wedge nanoindentation. A comprehensive evaluation of the influence of GNDs and non-Schmid effects on the plastic deformation response of the single crystal was performed under plane strain conditions. Dependent on the applied model, a significant difference in the stress state, the plastic shear on active slip systems and material pile-up around the indenter was observed. In contrast, solely slight deviations in the density of GNDs and crystal lattice rotation under the residual imprint were found. With the gradient-based crystal plasticity model, a size dependency of the plastic deformation could be described in addition. Further, a comparison between numerical and experimental results regarding GNDs, crystal lattice rotation and the residual geometry of the indent was performed. A very good agreement between the experimental and simulated deformed geometry of the specimen was found in the crystal plasticity simulation. The comparison of the GND density and lattice rotation in the region under the indenter flanks showed a good agreement as well. However, all numerical simulations overestimate both, the crystal lattice rotation and density of GNDs that occur in the region under the indenter tip.

Kurzfassung

Ziel der vorliegenden Arbeit war die numerische Untersuchung des plastischen Verformungsverhaltens von Wolfram Einkristallen während eines Nanoindentierungsversuchs mit Hilfe von Finite-Element Simulationen. Die Herausforderung bei numerischen Simulationen des plastischen Verformungsverhaltens von kubisch-raumzentrierten Materialien auf der Mikroebene liegt nicht nur in der Notwendigkeit eines Materialmodells, um die gleitdominierte plastische Verformung des Kristalls zu beschreiben, sondern zusätzlich darin, Gradienten der plastischen Scherung und Nicht-Schmidsche Effekte zu berücksichtigen. Deshalb wurde in dieser Arbeit ein vorhandenes Modell der Kristallplastizität erweitert, um auch Nicht-Schmidsches Verhalten und das Auftreten von geometrisch notwendigen Versetzungen in FE-Simulationen berücksichtigen zu können. Mit diesen erweiterten Kristallplastizitätsmodellen wurde detailliert untersucht, wie sowohl Nicht-Schmidsches Verhalten als auch das Auftreten von geometrisch notwendigen Versetzungen das plastische Verformungsverhalten in einem ebenen Dehnungszustand beeinflusst. Abhängig von dem verwendeten Materialmodell ergaben sich stark unterschiedliche Simulationsergebnisse für den vorherrschenden Spannungszustand, die plastische Scherung auf aktiven Gleitsystemen und die Materialanhäufung an der Oberfläche der indentierten Probe. Im Gegensatz dazu wurde in den verschiedenen Simulationen eine gute Übereinstimmung der Dichte der geometrisch notwendigen Versetzungen und der Gitterrotation gefunden. Das gradientenbasierte Materialmodell ermöglichte zudem die Beschreibung der Größenabhängigkeit des plastischen Verformungsverhaltens abhängig von der gewählten Indentierungstiefe. Zusätzlich wurden die numerischen Ergebnisse der Dichte der geometrisch notwendigen Versetzungen und der Gitterrotation unter dem Indenter mit experimentellen Versuchsergebnissen verglichen. Dabei konnte eine sehr gute Übereinstimmung der Geometrie der verformten Probe zwischen der Kristallplastizitätssimulation und dem experimentellen Ergebnis festgestellt werden. Eine gute Übereinstimmung wurde ebenfalls für den Vergleich der

Gitterrotation und der Dichte der geometrisch notwendigen Versetzungen für alle Materialmodelle und dem Experiment gefunden, allerdings nur in den Bereichen rechts und links des Indenters. Direkt unter der Indenterspitze wurden in den Simulationen weit höhere Werte berechnet als im Experiment auftraten.

Contents

Nomenclature

Abbreviation

BCC	body-centered cubic
CP	crystal plasticity
DDD	discrete dislocation dynamics
EBSD	electron backscatter diffraction
FCC	face-centered cubic
FE	finite-element
FIB	focused ion beam
GND	geometrically necessary dislocations
INC	increment
IPT	integration point
ISE	indentation size effects
KAM	kernel average misorientation
KINC	number of increment
MBSGCP	mechanism-based strain gradient crystal plasticity
MD	molecular dynamics
N	node
NSLPTL	number of slip systems
NOSCP	non-Schmid crystal plasticity
PAN	Peirce Asaro Needleman hardening model
SDV	solution-dependent state variables
SSD	statistically stored dislocations
STATEV	state variable
UMAT	user-material subroutine
URDFIL	user subroutine to read the results file
UEXTERNALDB	user subroutine to manage user-defined external databases and calculate model-independent history information

Greek characters

α_{T}	material parameter
α, β	slip system
γ	plastic shear
$\dot{\gamma}$	plastic shear rate
$\dot{\gamma}_0$	reference shear rate
$\nabla\gamma$	gradient of plastic shear
ε	strain
μ	coefficient of friction
ρ	density
$\boldsymbol{\sigma}$	stress tensor
τ	shear stress
τ_0	initial shear stress
τ_{c}	critical resolved shear stress
τ_s	saturation stress, Schmid contribution to shear stress
τ_{ns}	non-Schmid contribution to shear stress
$\varphi_1, \boldsymbol{\Phi}, \varphi_2$	Euler angles following Bunge
$\boldsymbol{\psi}, \xi, \eta, \rho$	local coordinates
$\boldsymbol{\Omega}$	plastic spin
$\boldsymbol{\Omega}^e$	elastic part of the plastic spin
$\boldsymbol{\Omega}^p$	plastic part of the plastic spin
ω	in-plane lattice rotation

Latin characters

$\boldsymbol{A}$	contact area
a_1, a_2, a_3	material parameter for non-Schmid simulations
$\boldsymbol{b}$	Burgersvector
C_{11}, C_{12}, C_{44}	elastic constants
$\boldsymbol{D}$	rate of stretching
$\boldsymbol{D}^e$	elastic part of the rate of stretching
$\boldsymbol{D}^p$	plastic part of the rate of stretching
$\boldsymbol{D}_\mathrm{s}$	rate of stretching in the conventional CP simulation
$\boldsymbol{F}$	deformation gradient
F	load on indenter
$\boldsymbol{F}^e$	elastic part of the deformation gradient
$\boldsymbol{F}^p$	plastic part of the deformation gradient
$\dot{\boldsymbol{F}}^p$	rate of the plastic part of the deformation gradient
f	approximation function
G	shear modulus
g	current strength
$\boldsymbol{g}$	gravity load
g_GND	current strength contributions by GNDs
g_SSD	current strength contributions by SSDs
g_T	total current strength
$\dot{g}_\mathrm{c}^\alpha$	critical shear stress rate
H	hardness
H_0	hardness at infinite indentation depth
h	indentation depth
h_max	maximum indentation depth
$h_{\alpha\beta}$	hardening module
h_0	initial hardening modulus
$\boldsymbol{J}$	Jacobian matrix
$\boldsymbol{L}$	velocity gradient
l	intrinsic length scale, length
l_0	initial length

$\boldsymbol{L}^p$	plastic flow rate
$\boldsymbol{m}$	normal to slip plane
$\dot{\boldsymbol{m}}$	derivative of slip direction
$\boldsymbol{m}^{\mathrm{i}}$, $\boldsymbol{m}_{\mathrm{i}}$	initial normal to slip plane
$\boldsymbol{m}^{\mathrm{c}}$, $\boldsymbol{m}_{\mathrm{c}}$	current normal to slip plane
$\boldsymbol{m}_1$	unit vector perpendicular to {110} planes
N	shape function
n	rate sensitivity exponent
n_{G}	density of GNDs
$\boldsymbol{P}_{\mathrm{mod}}$	sum of the Schmid and non-Schmid tensor
$\boldsymbol{P}$, $\boldsymbol{P}_{\mathrm{s}}$	Schmid tensor
$\boldsymbol{P}_{\mathrm{ns}}$	non-Schmid tensor
$\boldsymbol{P}^{\mathrm{eff}}$	effective Schmid tensor based on the combination of two slip systems
q	relation of the latent- and self-hardening
$\boldsymbol{R}$, $\boldsymbol{O}$	rotation matrix
$\boldsymbol{r}$	local coordinate
$\boldsymbol{s}$	slip direction
$\dot{\boldsymbol{s}}$	derivative of slip direction
$\boldsymbol{s}^{\mathrm{i}}$, $\boldsymbol{s}_{\mathrm{i}}$	initial slip direction
$\boldsymbol{s}^{\mathrm{c}}$, $\boldsymbol{s}_{\mathrm{c}}$	current slip direction
T	temperature
t	time
$\boldsymbol{t}$	traction
$\boldsymbol{u}$	rotation axis
$\boldsymbol{u}_{\mathrm{IPT}}$	displacement of integration points
$\boldsymbol{u}_{\mathrm{N}}$	displacement of nodes
w, b, h	width, length, height
x_{L}, y_{L}, z_{L}	local coordinates
x_{G}, y_{G}, z_{G}	global coordinates

1 Introduction and outline

The wish for highly sophisticated technical systems caused an ever increasing demand on high performance structural materials. This constitutes the need for advanced numerical simulations to characterize the physical behavior of materials under thermal and mechanical loads in ever greater detail. In particular, the miniaturization of components, e.g. in microelectronics, electro-mechanical microsystems and optical and medical devices requires numerical simulations on the microscale based on material models capable of incorporating microstructural features. Beside this, the design of a particular microstructure may be necessary for macroscopic components that experience severe heat and mechanical loads, like e.g. turbine blades, which requires again the possibility to model the microstructures of materials and their influence on the mechanical response.

In the course of material research for nuclear fusion reactors, there is particular demand on numerical studies on tungsten and tungsten based alloys. They are currently seen as the most promising candidates for so-called first wall materials for components that face the nuclear fusion. On the one hand, their high density, high melting point and high heat conductivity make them well suited materials for components that have to withstand severe high heat flux and significant neutron irradiation (Linsmeier et al. 2017). On the other hand, an application of tungsten is limited by its temperature dependent deformation behavior, i.e. the brittle-to-ductile transition far above room temperature, that various body-centered cubic (bcc) materials exhibit. A detailed understanding of the deformation behavior and fracture mechanism at the microscale are therefore necessary and indispensable for an application. However, for further investigations of e.g. the fracture toughness on the microscale or the incorporation of a temperature dependency in the simulations, an approach to describe the materials deformation behavior regarding for the size effect and a violation of Schmid's law (Schmid 1924) is a prerequisite.

These challenges are addressed in the course of this thesis by numerical studies

based on the crystal plasticity (CP) constitutive model as a starting point. The CP model incorporated in the framework of the finite-element method (CPFE) enables an integration of the anisotropic deformation of single crystals and dislocations in the continuum field of deformation (Roters et al. 2010). Thereby, problems with complex boundary conditions can be solved based on computational tools of continuum mechanics making the CPFE the powerful tool it is. However, the model of crystal plasticity lacks an intrinsic length scale and is therefore not able to account for the size effect which influences the deformation response on the micrometer length-scale significantly. Furthermore, the model is based on Schmid's law which is violated for bcc materials (Christian 1983).

Hence, beyond the CP model, two material models, namely the mechanism-based strain gradient (MBSGCP) and non-Schmid crystal plasticity (NOSCP) models were used in this thesis for numerical microscale studies on the plastic deformation of tungsten single crystals. The mechanism-based strain gradient crystal plasticity (MBSGCP) constitutive model accounts for size dependency by introducing a density of geometrically necessary dislocations (GND) corresponding to gradients of plastic shear. The NOSCP, uses a modified formulation for the determination of the resolved shear stress, the driving force of dislocation motion, following the atomistic studies of Gröger et al. (Gröger et al. 2008b).

This thesis aims at a contribution to a more detailed characterization of tungsten at the microscale by applying the crystal plasticity, the MBSGCP and the NOSCP within the finite-element method for numerical simulations of wedge nanoindentation, a well-established method for the investigation of an abundance of material properties at the microscale. In the course of this thesis, the deformation under the indenter is characterized by the activity of slip systems, the crystal lattice rotation and the density of geometrically necessary dislocations, all determined with the three models to study the influence of additional hardening due to geometrically necessary dislocation and non-Schmid effects on the plastic deformation response of tungsten single crystals.

Outline of this thesis

Chapter 2 serves as an overview of the general deformation behavior of tungsten and gives an introduction to experimental nanoindentation and its numerical simulation. Further, a brief summary of the physical background of the conventional, the mechanism-based strain gradient and non-Schmid model is given together with the mathematical formulations. Last, the determination of the crystal lattice rotation is described.

Chapter 3 gives a comprehensive description of the implementation of the mechanism-based strain gradient crystal plasticity subroutine as an extension of the conventional CP subroutine by Huang (Huang 1991). The MBSGCP subroutine was used for a first simulation of a simple bar under traction and gravity load for an evaluation.

Chapter 4 contains a summary of the experimental nanoindentation, regarding the sample preparation and indentation procedure, performed by J. Wang at the Karlsruhe Institute of Technology. The experimental results were used for a comparison to the numerical results calculated in this thesis.

Chapter 5 gives an overview over the applied crystal orientations and the three simulation models used in this work, namely the brick-shaped, the single-layer and the bridge-shaped model. The brick-shaped model was used together with the conventional and non-Schmid subroutine. For the computationally more expensive MBSGCP simulation, the single-layer model was used. For the comparison of experimental and numerical results, the bridge-shaped model was used together with the conventional and non-Schmid CP subroutines.

Chapter 6 contains the results of active slip systems, stress state, increments of plastic shear, crystal lattice rotation and the GND density calculated in the midsection of the brick-shaped model for both, the $[0\bar{1}0]$ and [123] orientation, with the conventional crystal plasticity subroutine. With the two orientations, the dependency of the indentation direction and deformation behavior was investigated. The $[0\bar{1}0]$ simulation results served as reference for the study of the influence of strain gradients and non-Schmid effects on the plastic deformation behavior.

Further, the single-layer model was used together with the MBSGCP subroutine and the $[0\bar{1}0]$ oriented single crystal. A comparison of the mechanism-based strain gradient and conventional crystal plasticity simulation was performed regarding the slip system activities, stress state, crystal lattice rotation and GND density. In addition, the indentation size effect was studied in detail with the MBSGCP material model.

Moreover, the influences of non-Schmid effects on the plastic deformation behavior was studied with the non-Schmid version of CP together with the brick-shaped model and the $[0\bar{1}0]$ oriented tungsten single crystal. The activities of slip systems, the stress state, increments of plastic shear, crystal lattice rotation, GND density, material pile-up and load-displacement curve were analyzed in the midsection and compared to the conventional CP results.

The last part of chapter 6 contains the results of the deformed geometry after indentation, the crystal lattice rotation and the density of geometrically necessary dislocations determined with the bridge-shaped model together with both, the conventional CP and non-Schmid material model. The simulations were performed with the $[0\bar{1}0]$ oriented tungsten single crystal. The results of the two simulations were compared to the experiments conducted by J. Wang.

2 Theory and background

2.1 Plastic deformation of tungsten

Plastic deformation in single crystals is generally caused by dislocation motion on close-packed planes in close-packed directions, i.e. planes with the highest density of atoms and directions with the smallest atom spacing. The slip directions, denoted by the vector ***s***, correspond to the Burgersvector ***b*** of a dislocation. Slip planes are denoted by the vector ***m***, perpendicular to slip directions. Motion of dislocation requires a driving force, namely the shear stress, resolved on the slip plane in the slip direction. According to Schmid (Schmid 1924), slip occurs if the resolved shear stress τ^{α} on slip system α, caused by an external load, reaches a critical shear stress τ_c^{α}:

$$\tau^{\alpha} = \boldsymbol{P}^{\alpha} : \boldsymbol{\sigma} = \tau_c^{\alpha}. \tag{2.1}$$

Here, $\boldsymbol{\sigma}$ is the stress tensor and $\boldsymbol{P}$ the Schmid tensor, defined by the slip plane normal $\boldsymbol{m}$ and slip direction $\boldsymbol{s}$ for a slip system α:

$$\boldsymbol{P}^{\alpha} = \frac{1}{2}(\boldsymbol{m}^{\alpha} \otimes \boldsymbol{s}^{\alpha} + \boldsymbol{s}^{\alpha} \otimes \boldsymbol{m}^{\alpha}). \tag{2.2}$$

In opposite to face-centered cubic (fcc) materials, where the operating slip systems consists of {111} planes and ⟨110⟩ directions, in body-centered cubic structures like e.g. iron, chromium and tungsten, dislocation motion is in ⟨111⟩ directions and the Burgersvector is of ½⟨111⟩ type but potentially on the {110}, {112} and {123} family of planes. However, atomistic studies have shown, that {110} planes are the principle slip planes in bcc materials (Gröger et al. 2008a; Gröger et al. 2008b; Gröger and Vitek 2008) which are shown together with the closed packed ⟨111⟩ direction in the bcc unit cell in figure 1.

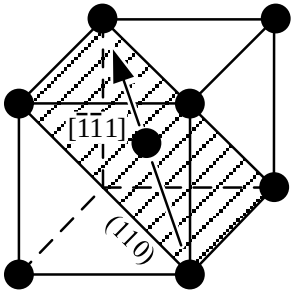

Figure 1: {110} slip plane with the ⟨111⟩ slip direction in the unit cell of the bcc crystal

The motion of dislocation is dependent on the critical shear stress which is the Peierls stress at T = 0 K in bcc crystal structures but decreases with increasing temperature. This is because thermal motion of atoms promotes the dislocation motion and thereby justify the strong temperature dependency of bcc materials and their brittle-to-ductile transitions (Gottstein 2014).
Because of their compact core structure, screw dislocations require a high critical stress to be moved (on the order of 1 GPa at T = 0 K). Non-screw dislocations however, have a much higher mobility within the bcc crystal and their motion forms long screw dislocation segments. Thus, the plastic deformation of bcc structures is mainly dominated by the motion of screw dislocations (Christian 1983). Screw dislocation cores in bcc materials spread into three {110} planes and a motion requires a recombination of the non-planar dislocation core (Vitek 2004). Two types of screw dislocation core structures exist (see Vitek 2004 for a detailed description and visualization of the structures), the so-called degenerate and non-degenerate core. The degenerate core structure can be translated to an energetically equivalent configuration by a rotation around the [10$\bar{1}$] axis. This core spreads asymmetrically into the ($\bar{1}$01), (0$\bar{1}$1) and ($\bar{1}$10) planes. The non-degenerate core does not exhibit such a symmetry and spreads into the ($\bar{1}$01), (0$\bar{1}$1) and ($\bar{1}$10) planes, too. For the non-planar spreading of the core, necessary for a dislocation motion, a prior transformation is necessary. This transformation is affected by stresses in the slip direction on planes other than the slip plane and shear stresses perpendicular to

the slip direction (Duesbery 1984; Duesbery and Vitek 1998), i.e., Schmid's law is violated at low temperatures for bcc materials. Gröger et al. formulated a yield criterion that incorporates stresses perpendicular to the slip direction that affects the magnitude of the critical resolved shear stress of this slip system (Gröger et al. 2008b). This criterion was modified by Weinberger et al. (Weinberger et al. 2012) for an incorporation in the crystal plasticity constitutive model. A modified version of this formulation was used in this thesis as the basis for non-Schmid simulations and is described in detail in chapter 2.4.

2.2 Fundamentals of nanoindentation testing and simulation

Comparable to macroscopic hardness test, like e.g. Brinell, Rockwell or Vickers, nanoindentation is a non-destructive testing method that consists basically of touching a material with unknown properties with a harder indenter whose mechanical properties are known. The basis of most nanoindentation investigations are the so-called load-displacement curves being the fingerprints of a tested material. A typically load-displacement curve as determined in nanoindentation tests is shown in figure 2 b). Unlike in macroscopic hardness tests, the indentation depth in nanoindentation experiments is typically in the range of nanomenters up to few micrometers and the reaction force on the indenter therefore in the range of millinewton. In nanoindentation, usually the hardness of small volumes and thin films is of interest. In macroscopic hardness tests it is possible to determine the residual imprint visually (e.g. the diagonals of the quadratic residual imprint in the Vickers hardness test). It is used for the determination of the hardness defined as force divided by the contact area. In nanoindentation tests, the hardness is defined as the load on the indenter divided by the projected area of the imprint. The projected area is usually determined indirectly, based on the penetration measurements together with the known indenter geometry since a visual measurement is not possible. There is a great variety of indenter shapes that can be used in nanoindentation tests, e.g. cylindrical, conical, spherical, wedge-shaped and four-sided pyramid

indenters as well as the Berkovich (Berkovich 1951) and Knoop indenter (Knoop et al. 1939). Dependent on the investigations, a suited one has to be chosen. A commonly used is the Berkovich indenter, a three-sided pyramid with the same surface area to depth ratio as the Vickers indenter. An advantage of the Berkovich indenter are the three sides that meet at one single point which is not necessarily the case for a four-sides pyramid. For the investigations in this work however, a wedge indenter is chosen. Its decisive advantage are plane strain conditions that can occur in a plane normal to the indenter tip dependent on the boundary conditions and orientation of the single crystal. A comprehensive description and study of the crystal orientation and strain states is performed in the chapter 6.1.2 in this work.

Nanoindentation testing devices were significantly improved regarding the precision over the last decades and it has become a standard method which is widely used in research laboratories by many scientists whose aim is not solely the determination of the hardness of coatings and small volumes of material but many other microstructural parameters as well. Further properties of interest are e.g. the elastic modulus, strain hardening exponents, viscoelastic properties, fracture toughness, piling-up, sinking-in (see figure 2 a)) and together with methods like e.g. electron backscattering diffraction (EBSD), the determination of crystal lattice rotation and the density of geometrically necessary dislocations.

Pioneering work in the field of analysis of nanoindentation testing data was made by W. Oliver and G. Pharr. A comprehensive description of load-displacement based determination of hardness and elastic modulus can be found in their fundamental work (Pharr and Oliver 1991; Oliver and Pharr 1992; Pharr 1998; Pharr and Bolshakov 2002; Oliver and Pharr 2004). Both parameters, the load on the indenter and the displacement, are usually determined continuously over the indentation process by the indentation devices and appropriate software. The continuous stiffness measurement (CSM) method (Pethica and Oliver 1988) is today state of the art in nanoindentation devices to provide a continuous determination of the contact area, hardness and elastic modulus over the indentation process. In the CSM, an oscillation is applied to the in-

denter with amplitudes of few nanometers, much smaller than the actual indentation depth. Based on the oscillation, i.e. small loading and unloading cycles, the contact stiffness can be determined from the unloading slope continuously and so, the hardness and elastic modulus of the tested specimen.

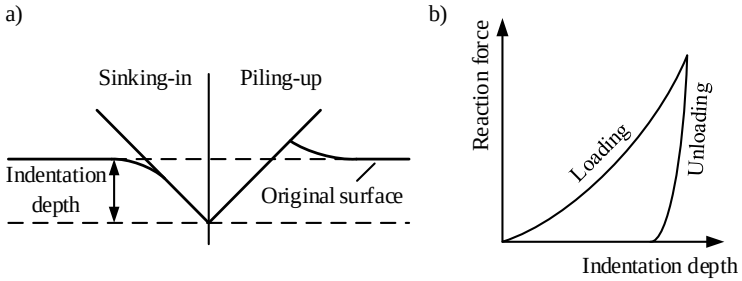

Figure 2: a) piling-up and sinking-in around an indenter; b) typical load-displacement determined in nanoindentation with loading and unloading part

Beside experimental nanoindentation, FE-simulations were widely used to investigate the deformation response of a material numerically as it is indented. A selection of relevant publications for the present work is given in the following. Volz et al. e.g. studied the slip system activity and lattice rotation (Volz et al. 2018). Yao studied the deformation behavior of single crystal tungsten by crystal plasticity FE-simulations of spherical and Berkovich indentation (Yao 2012). Demiral et al. investigated the surface topography of a body-centered cubic metallic material around indents (Demiral et al. 2013) and the crystal lattice rotation (Demiral et al. 2014) numerically using a mechanism-based strain gradient crystal plasticity model. Gerday et al. focused on the numerical modelling of a bcc alloy and investigated nanoindentation curves and pile-up and sink-in patterns (Gerday et al. 2009). Numerical investigations of micro texture evolution and mechanical properties of a face-centered cubic (fcc) material (aluminum) were carried out by Liu et al. (Liu et al. 2015). Indentation studies on copper regarding the effects of the crystallographic orientation, the indenter angle and contact conditions on the load-displacement curves were

studied by Zahedi et al. using the finite element method (Zahedi et al. 2012).
Other models to simulate the plastic deformation behavior are three-dimensional discrete dislocation dynamics (DDD), (Arsenlis et al. 2007; Ghoniem et al. 2000; Kubin et al. 1992; Schwarz 1999; Weygand et al. 2002; Zbib et al. 1998) and molecular dynamics (MD) (Alder and Wainwright 1959; Marx and Hutter 2000). The models are applied at different length- and time scales. J_2-plasticity or crystal plasticity are at the upper end of the time and length scale. J_2-plasticity finite-element simulations are today the most important tool for practical engineering problems. But since it does not care about the microstructure of a material, which influence the deformation behavior significantly at smaller length scales, an application is only convenient down to a certain length and time scale. It is best suited for length scales in the range of millimeters to meters and time scales from milliseconds to hours (Roters et al. 2010).
A lower scale model is the DDD method. It describes the motion and interaction of dislocations (line defects within a crystal lattice) resulting in plastic deformation. So it accounts for the microstructure and phenomena like the anisotropy of crystalline materials are well described. The length and time scale in the DDD method are usually in the range of 0.1 µm – 10 µm and 1 µs – 1 ms, respectively (Sills et al. 2016). For even lower scales, MD is best suited. It can describe the structure of defects in a crystal lattice and is therefore usually applied to problem setups smaller than few micrometers and time scales lower than milliseconds. So the plastic deformation response of tungsten single crystals in the region around the indenter at indentation depth of several micrometers and time scales up to minutes is best described by the crystal plasticity finite element method. It incorporates dislocation driven plastic deformation into the finite element method and thereby offers the possibility to regard for the anisotropic plastic deformation behavior of a crystal lattice in a continuum mechanical framework.
However, experimental nanoindentation has shown that metallic materials exhibit an indentation size effect (ISE), stating that the hardness of a metal increases as the indentation depth decreases (following e.g. (Nix 1989, 1997; Guzman et al. 1993; Stelmashenko et al. 1993; Atkinson 1995; Ma and Clarke 1995; Poole et al. 1996; Swadener et al. 2002)), as shown in figure 3 a). The

ISE may be caused by the friction between the indenter and the specimen (Li et al. 1993), strain-hardening from the sample preparation, residual stresses or errors in the determination of the contact area, especially at very small indentation depths (Fischer-Cripps 2011). Particularly in nanoindentation FE-simulation, the determination of the area is challenging and was comprehensively described by Volz et al. (Volz et al. 2017). However, even if all these mentioned effects can be excluded, the indentation size effect still occurs in nanoindentation experiments. The reason are severe strain gradients in the stress field under the indenter at small indentation depths. The plastic flow in this region does not solely depend on the strain state but also on the gradients of strain. These gradients are associated with the so-called geometrically necessary dislocations that arise from the geometry of the indenter as it is pushed into the sample as shown in figure 3 b).

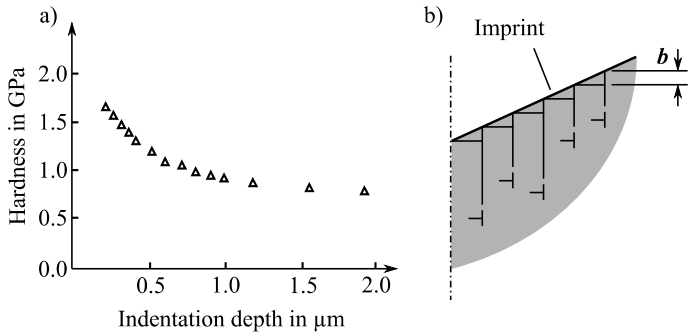

Figure 3: a) indentation size effect of (111) single crystal copper determined by McElhaney et al. (McElhaney et al. 1998); b) geometrically necessary dislocations in the plastic zone around the indent following Fischer-Cripps (Fischer-Cripps 2011)

For higher indentation depth strain gradients decrease and become insignificant, explaining the ISE. The wish to regard for the indentation size effect in the simulations motivated the implementation of the mechanism-based strain gradient crystal plasticity subroutine in this work.

The violation of Schmid's law and the indentation size effect were the motivation for the extensions of the user-material subroutine (UMAT) for crystal plasticity, implemented by Huang (Huang 1991) and modified by Kysar (Kysar 1997), to account for non-Schmid effects and gradients of plastic shear. Figure 4 visualizes the so-called MBSGCP and NOSCP subroutines developed in this work, based on the determination of strain gradients and non-Schmid terms.

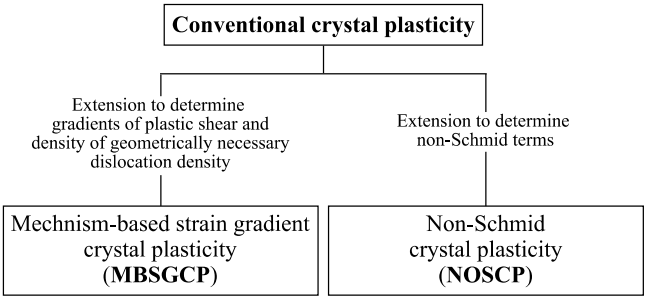

Figure 4: Extensions of the conventional crystal plasticity for the numerical investigations of the plastic deformation of tungsten performed in this work

2.3 Conventional crystal plasticity

The numerical investigations performed in this work are based on the crystal plasticity model introduced by Rice (Rice 1971), Hill and Rice (Hill and Rice 1972) and Asaro and Rice (Asaro and Rice 1977) which is based on the Taylor dislocation model (Taylor 1938). The first FEM based investigations using a strain rate-independent crystal plasticity model was carried out by Peirce et al. (Peirce et al. 1982; Peirce et al. 1983), the first rate-dependent investigation by Asaro and Needleman in 1989 (Asaro and Needleman 1989). Two years later, Huang (Huang 1991) implemented a user-material subroutine for finite element simulations in the software package ABAQUS that is used in this work. The basics of the implementation are given in the following.

In finite non-linear plasticity, the deformation gradient is in general decomposed multiplicatively following Lee (Lee 1969):

$$\boldsymbol{F} = \boldsymbol{F}^{\mathrm{e}}\boldsymbol{F}^{\mathrm{p}}, \tag{2.3}$$

where $\boldsymbol{F}^{\mathrm{e}}$ is the elastic part that causes elastic stretching and rotation of the lattice and $\boldsymbol{F}^{\mathrm{p}}$ is the plastic part that causes plastic shear but leaves the crystal lattice undistorted (see figure 5).

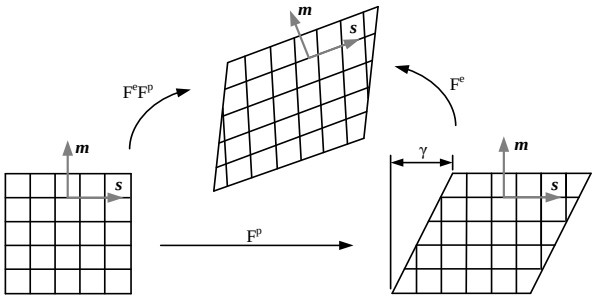

Figure 5: Multiplicative decomposition of the deformation gradient $\boldsymbol{F}$ into the plastic and elastic parts $\boldsymbol{F}^{\mathrm{p}}$ and $\boldsymbol{F}^{\mathrm{e}}$

The rate of change of $\boldsymbol{F}^{\mathrm{p}}$ is related to the slipping rate $\dot{\gamma}^{\alpha}$ of slip system α by the expression:

$$\boldsymbol{L}^{\mathrm{p}} = \dot{\boldsymbol{F}}^{\mathrm{p}}\boldsymbol{F}^{\mathrm{p}-1} = \sum_{\alpha} \dot{\gamma}^{\alpha}\, \boldsymbol{s}^{\alpha}\boldsymbol{m}^{\alpha}. \tag{2.4}$$

The velocity gradient $\boldsymbol{L}$ is related to the deformation gradient $\boldsymbol{F}$ and the symmetric rate of stretching $\boldsymbol{D}$ and the unsymmetrical spin tensor $\boldsymbol{\Omega}$ by:

$$\boldsymbol{L} = \dot{\boldsymbol{F}}^{-1}\boldsymbol{F} = \boldsymbol{D} + \boldsymbol{\Omega}. \tag{2.5}$$

$\dot{\boldsymbol{F}}^{\mathrm{e}}\boldsymbol{F}^{\mathrm{e}-1}$ and $\dot{\boldsymbol{F}}^{\mathrm{p}}\boldsymbol{F}^{\mathrm{p}-1}$ can be divided in $\boldsymbol{D}$ and $\boldsymbol{\Omega}$:

$$\dot{\boldsymbol{F}}^{\mathrm{e}}\boldsymbol{F}^{\mathrm{e}-1} = \boldsymbol{D}^{\mathrm{e}} + \boldsymbol{\Omega}^{\mathrm{e}} \text{ and } \dot{\boldsymbol{F}}^{\mathrm{p}}\boldsymbol{F}^{\mathrm{p}-1} = \boldsymbol{D}^{\mathrm{p}} + \boldsymbol{\Omega}^{\mathrm{p}}. \tag{2.6}$$

The elastic part causes rotation and stretching of the lattice. In a deformed state, the current slip directions and planes are defined as:

$$\boldsymbol{s}^{\alpha} = \boldsymbol{F}^{\mathrm{e}}\boldsymbol{s}_{\mathrm{i}}^{\alpha} \text{ and } \boldsymbol{m}^{\alpha} = \boldsymbol{m}_{\mathrm{i}}^{\alpha}\boldsymbol{F}^{\mathrm{e}-1}, \tag{2.7}$$

where $\boldsymbol{s}_{\mathrm{i}}^{\alpha}$ and $\boldsymbol{m}_{\mathrm{i}}^{\alpha}$ are the slip directions and slip plane vectors of slip system α in the initial state and $\boldsymbol{s}^{\alpha}$ and $\boldsymbol{m}^{\alpha}$ in the current state respectively. By differentiation one finds:

$$\dot{\boldsymbol{s}}^{\alpha} = \dot{\boldsymbol{F}}^{\mathrm{e}}\boldsymbol{s}^{\alpha} \text{ and } \dot{\boldsymbol{m}}^{\alpha} = \boldsymbol{m}^{\alpha}\dot{\boldsymbol{F}}^{\mathrm{e}-1}. \tag{2.8}$$

Based on Schmid's law, the following rate-dependent formulation is applied for the plastic shear rate on slip system α:

$$\dot{\gamma}^{\alpha} = \dot{\gamma}_0^{\alpha} sgn(\tau^{\alpha}) \left|\frac{\tau^{\alpha}}{g^{\alpha}}\right|^{n}. \tag{2.9}$$

In this equation, $\dot{\gamma}_0^{\alpha}$ is the reference shear rate, τ^{α} is the resolved shear stress, g^{α} the current strength of the slip system and n the rate sensitivity exponent.

The evolution equation:

$$\dot{g}^{\alpha} = \sum_{\beta} h_{\alpha\beta}\,\dot{\gamma}^{\beta} \tag{2.10}$$

describes the increase of the critical shear stress on every slip system α as a follow of plastic deformation, dependent on the hardening module $h_{\alpha\beta}$ and the

plastic shear rate $\dot{\gamma}^{\beta}$. If $\alpha = \beta$, self-hardening and if $\alpha \neq \beta$, latent hardening occurs. In case of latent hardening, secondary slip systems also strengthen. The hardening module describing self-hardening was proposed by Peirce, Asaro and Needleman (Peirce et al. 1982) as:

$$h_{\alpha\alpha} = h(\gamma) = h_0 sech^2 \left| \frac{h_0 \gamma}{\tau_s - \tau_0} \right|, \tag{2.11}$$

where γ denotes the cumulative plastic shear on all slip systems, h_0 is the initial hardening modulus and τ_0 the initial shear stress value which is equal to the initial value of the shear strength $g^{\alpha}(0)$. The relation of the latent- and self-hardening is described by the parameter q:

$$h_{\alpha\beta} = q h(\gamma). \tag{2.12}$$

In the equation, q describes the latent hardening effect (hardening on slip system α caused by slip on slip system β).

2.4 Non-Schmid crystal plasticity

The extension of the conventional crystal plasticity subroutine to incorporate non-Schmid effects (motivated in chapter 2.1) for the simulation of tungsten single crystals at the microstructure is based on the atomistic simulations of Gröger et al. (Gröger et al. 2008b). They defined the following yield criterion for slip in bcc single crystals:

$$\begin{aligned} \tau_c = {} & \boldsymbol{s}^{\alpha} \cdot \boldsymbol{\sigma m}^{\alpha} + a_1 \boldsymbol{s}^{\alpha} \cdot \boldsymbol{\sigma m}_1^{\alpha} + a_2 (\boldsymbol{m}^{\alpha} \times \boldsymbol{s}^{\alpha}) \cdot \boldsymbol{\sigma m}^{\alpha} \\ & + a_3 (\boldsymbol{m}_1^{\alpha} \times \boldsymbol{s}^{\alpha}) \cdot \boldsymbol{\sigma m}_1^{\alpha}, \end{aligned} \tag{2.13}$$

where $\boldsymbol{m}_1^{\alpha}$ is the unit vector that stands perpendicular to {110} planes. This vector makes an angle of -60° with the reference plane $\boldsymbol{m}^{\alpha}$. The constant material parameters a_1, a_2 and a_3 were determined by Gröger et al. (Gröger et al. 2008b) in atomistic calculations. For tungsten, the parameters are $a_1 = 0$, $a_2 = 0.56$ and $a_3 = 0.75$. The first term in equation (2.13) is the Schmid stress that acts on the slip plane in slip direction. The second term represents a contribution due to the twinning and anti-twinning asymmetry. The third and fourth term describe stresses perpendicular to the dislocation core. The last three terms are thereby non-Schmid terms which do not contribute to the driving force but act on the dislocation core and alter the critical resolved shear stress that is necessary for dislocation motion. To facilitate the incorporation of (2.13) into a crystal plasticity formulation, Weinberger et al. (Weinberger et al. 2012) re-wrote the equation as a set of projection tensors. Beside the Schmid tensor $\boldsymbol{P}_{\mathrm{s}}^{\alpha}$, they defined a non-Schmid projection tensor $\boldsymbol{P}_{\mathrm{ns}}^{\alpha}$:

$$\begin{aligned}\boldsymbol{P}_{\mathrm{ns}}^{\alpha} = a_1(\boldsymbol{s}^{\alpha} \otimes \boldsymbol{m}_1^{\alpha}) + a_1(\boldsymbol{m}^{\alpha} \times \boldsymbol{s}^{\alpha}) \otimes \boldsymbol{m}^{\alpha}. \\ + a_3(\boldsymbol{m}_1^{\alpha} \times \boldsymbol{s}^{\alpha}) \otimes \boldsymbol{m}_1^{\alpha}\end{aligned} \tag{2.14}$$

This allows to express equation (2.13) in the following form:

$$\tau_{\mathrm{c}} = \boldsymbol{P}_{\mathrm{s}}^{\alpha} : \boldsymbol{\sigma} + \boldsymbol{P}_{\mathrm{ns}}^{\alpha} : \boldsymbol{\sigma}. \tag{2.15}$$

In this way, stresses that do not act in the slip direction (non-Schmid stresses) add to the total driving force on a dislocation:

$$\tau^{\alpha} = \boldsymbol{P}_{\mathrm{s}}^{\alpha} : \boldsymbol{\sigma} + \boldsymbol{P}_{\mathrm{ns}}^{\alpha} : \boldsymbol{\sigma} = \tau_{\mathrm{s}} + \tau_{\mathrm{ns}}. \tag{2.16}$$

Following the former consideration, the rate-dependent formulation for the plastic shear rate in the conventional crystal plasticity model can be modified:

$$\dot{\gamma}^{\alpha} = \dot{\gamma}_0^{\alpha} sgn(\tau^{\alpha}) \left| \frac{\boldsymbol{P}_{\mathrm{s}}^{\alpha} : \boldsymbol{\sigma} + \boldsymbol{P}_{\mathrm{ns}}^{\alpha} : \boldsymbol{\sigma}}{g^{\alpha}} \right|^{n}. \tag{2.17}$$

As mentioned above, solely slip on the {110}⟨111⟩ slip systems is expected. However, instead of working with 12 slip systems, where each system can be activated in positive and negative slip direction, 24 slip systems are generated in the non-Schmid subroutine that was used in this work and only positive slip on these slip systems is allowed. Adding up the plastic shear γ^{α} of slip on each two collinear slip systems which only differ in the sign of their slip direction gives a value which can be directly compared to the plastic shear computed with the conventional CP subroutine. Table 1 lists the slip plane normals and slip directions of the 24 slip systems together with the unit vectors $\boldsymbol{m}_1^{\alpha}$ defined in the non-Schmid simulation.

Per definition, one of the 24 slip systems can only be active if the Schmid contribution $\tau_{\mathrm{s}}^{\alpha}$ to the overall resolved shear stress is positive. In case of negative values, a slip system is regarded to be inactive independent of the value and sign of the non-Schmid contribution $\tau_{\mathrm{ns}}^{\alpha}$. During the indentation process, the Schmid part $\tau_{\mathrm{s}}^{\alpha}$ can alter from a negative to a positive value. Consequently, slip on this slip system gets activated. If the Schmid shear stress undergoes a sign change at a point of the indentation process and the non-Schmid contribution $\tau_{\mathrm{ns}}^{\alpha}$ at this time has a high and positive value, exceeding the Schmid contribution by far, a sudden high activity of this slip system may occur, resulting in a very high stress. In the course of this work, it was found that such conditions occur in the non-Schmid simulation resulting in a termination of the calculation. Therefore, the equation (2.17) was modified to:

$$\dot{\gamma}^{\alpha} = \dot{\gamma}_0^{\alpha}\ sgn(\tau^{\alpha}) \left| \frac{\sqrt{(\boldsymbol{P}_{\boldsymbol{s}}^{\alpha} : \boldsymbol{\sigma})^2 + (\boldsymbol{P}_{\mathrm{s}}^{\alpha} : \boldsymbol{\sigma})(\boldsymbol{P}_{\mathrm{ns}}^{\alpha} : \boldsymbol{\sigma})}}{g^{\alpha}} \right|^{n}. \tag{2.18}$$

This formulation avoids an abrupt increase of plastic shear on a slip system during the indentation simulation. The weighting function leads to an underestimation of the non-Schmid effects. However, the reformulation is seen as an appropriate way to make the non-Schmid formulation usable in the nanoindentation simulations with its complex stress state under the indent.

Table 1: Slip systems following Gröger et al. (Gröger et al. 2008b) defined in the non-Schmid simulations

	Reference-system	s^α	m^α	m_1	α	Reference-system	s^α	m^α	m_1
1	$(01\bar{1})[111]$	$[111]$	$[01\bar{1}]$	$[\bar{1}10]$	13	$(01\bar{1})[\bar{1}\bar{1}\bar{1}]$	$[\bar{1}\bar{1}\bar{1}]$	$[01\bar{1}]$	$[10\bar{1}]$
2	$(\bar{1}01)[111]$	$[111]$	$[\bar{1}01]$	$[0\bar{1}1]$	14	$(\bar{1}01)[\bar{1}\bar{1}\bar{1}]$	$[\bar{1}\bar{1}\bar{1}]$	$[\bar{1}01]$	$[\bar{1}10]$
3	$(1\bar{1}0)[111]$	$[111]$	$[1\bar{1}0]$	$[10\bar{1}]$	15	$(1\bar{1}0)[\bar{1}\bar{1}\bar{1}]$	$[\bar{1}\bar{1}\bar{1}]$	$[1\bar{1}0]$	$[0\bar{1}1]$
4	$(\bar{1}0\bar{1})[\bar{1}11]$	$[\bar{1}11]$	$[\bar{1}0\bar{1}]$	$[\bar{1}\bar{1}0]$	16	$(\bar{1}0\bar{1})[1\bar{1}\bar{1}]$	$[1\bar{1}\bar{1}]$	$[\bar{1}0\bar{1}]$	$[01\bar{1}]$
5	$(0\bar{1}1)[\bar{1}11]$	$[\bar{1}11]$	$[0\bar{1}1]$	$[101]$	17	$(0\bar{1}1)[1\bar{1}\bar{1}]$	$[1\bar{1}\bar{1}]$	$[0\bar{1}1]$	$[\bar{1}\bar{1}0]$
6	$(110)[\bar{1}11]$	$[\bar{1}11]$	$[110]$	$[01\bar{1}]$	18	$(110)[1\bar{1}\bar{1}]$	$[1\bar{1}\bar{1}]$	$[110]$	$[101]$
7	$(0\bar{1}\bar{1})[\bar{1}\bar{1}1]$	$[\bar{1}\bar{1}1]$	$[0\bar{1}\bar{1}]$	$[1\bar{1}0]$	19	$(0\bar{1}\bar{1})[11\bar{1}]$	$[11\bar{1}]$	$[0\bar{1}\bar{1}]$	$[\bar{1}0\bar{1}]$
8	$(101)[\bar{1}\bar{1}1]$	$[\bar{1}\bar{1}1]$	$[101]$	$[011]$	20	$(101)[11\bar{1}]$	$[11\bar{1}]$	$[101]$	$[1\bar{1}0]$
9	$(\bar{1}10)[\bar{1}\bar{1}1]$	$[\bar{1}\bar{1}1]$	$[\bar{1}10]$	$[\bar{1}0\bar{1}]$	21	$(\bar{1}10)[11\bar{1}]$	$[11\bar{1}]$	$[\bar{1}10]$	$[011]$
10	$(10\bar{1})[1\bar{1}1]$	$[1\bar{1}1]$	$[10\bar{1}]$	$[110]$	22	$(10\bar{1})[\bar{1}1\bar{1}]$	$[\bar{1}1\bar{1}]$	$[10\bar{1}]$	$[0\bar{1}\bar{1}]$
11	$(011)[1\bar{1}1]$	$[1\bar{1}1]$	$[011]$	$[\bar{1}01]$	23	$(011)[\bar{1}1\bar{1}]$	$[\bar{1}1\bar{1}]$	$[011]$	$[110]$
12	$(\bar{1}\bar{1}0)[1\bar{1}1]$	$[1\bar{1}1]$	$[\bar{1}\bar{1}0]$	$[0\bar{1}\bar{1}]$	24	$(\bar{1}\bar{1}0)[\bar{1}1\bar{1}]$	$[\bar{1}1\bar{1}]$	$[\bar{1}\bar{1}0]$	$[\bar{1}01]$

2.5 Strain gradient crystal plasticity

Motivated by the size effect, a variety of strain gradient models were developed to regard for size dependency of plastic deformation over the last decades. Fleck and Hutchinson (Fleck and Hutchinson 1993) developed a phenomenological plasticity law where stress is not solely a function of strain but also strain gradients. They linked the gradients of plastic strain to the geometrically necessary dislocations (GND) introduced by Nye (Nye 1953) and (Ashby 1970). An example following Arsenlis and Parks (Arsenlis and Parks 1999), explaining the link between GNDs and non-uniform plastic deformation is shown in figure 6. A non-uniform deformation of the material section shown in figure 6 a) can be described by introducing an intermediate state (figure 6

b)) in which the section is divided into two similar parts which are plastically deformed so that $\gamma_1 < \gamma_2$ i.e. a gradient of strain occurs between the two sections, beside lattice rotation, two edge dislocations must be introduced for compatibility reasons as shown in figure 6 c). These introduced dislocations are GNDs occurring in the crystal to ensure homogenous plastic deformation in non-uniformly deformed areas. Whereas GNDs accumulate in regions with non-uniform strain states, statistically stored dislocations are uniformly generated and distributed within the crystal lattice. SSDs accumulate evenly in the crystal by random mutual trapping and therefore cause isotropic hardening of the material (Ashby 1970). The occurrence of GNDs in regions with non-uniform deformation however, i.e. additional obstacles in these regions, lead to a local, non-homogenous increase of the mechanical strength.

Following Niordson and Hutchinson (Niordson and Hutchinson 2003), strain gradient plasticity theories developed and used in the last decades can be divided into two classes, so-called lower-order theories with conventional stresses and boundary conditions (Bassani 2001; Arsenlis and Parks 1999; Busso et al. 2000; Han et al. 2005; Meissonnier et al. 2001; Yefimov and van der Giessen 2005) and higher theories involving additional stresses and boundary conditions. (Fleck and Hutchinson 1993, 2001, 1997; Borst and Mühlhaus 1992; Gao et al. 1999; Fleck et al. 1994; Huang et al. 2000a; Huang et al. 2000b). For the numerical strain gradient plasticity investigations in this work, a lower order approach is seen as favorable since the classical finite element method with standard element types can be used as no additional stresses or boundaries conditions are necessary. Further, an incorporation of the strain gradient model into the crystal plasticity model is necessary to account for the single crystals anisotropy. A lower order formulation based on the Peach-Koehler force and the dislocation density tensor, meeting the mentioned requirements was developed by Han et al. (Han et al. 2005). Based on this model, Demiral (Demiral 2012) implemented a user subroutine and investigated spherical nanoindentation and micro pillar compression of bcc single crystals numerically. Siddiq et al. (Siddiq et al. 2007) investigated the fracture of bicrystals with the mechanism-based strain gradient crystal plasticity model

following Han et al. (Han et al. 2005). Lee and Chen (Lee and Chen 2010) used the mechanism-based strain gradient model to simulate the size effect in the micro-indentation process of single crystal copper.

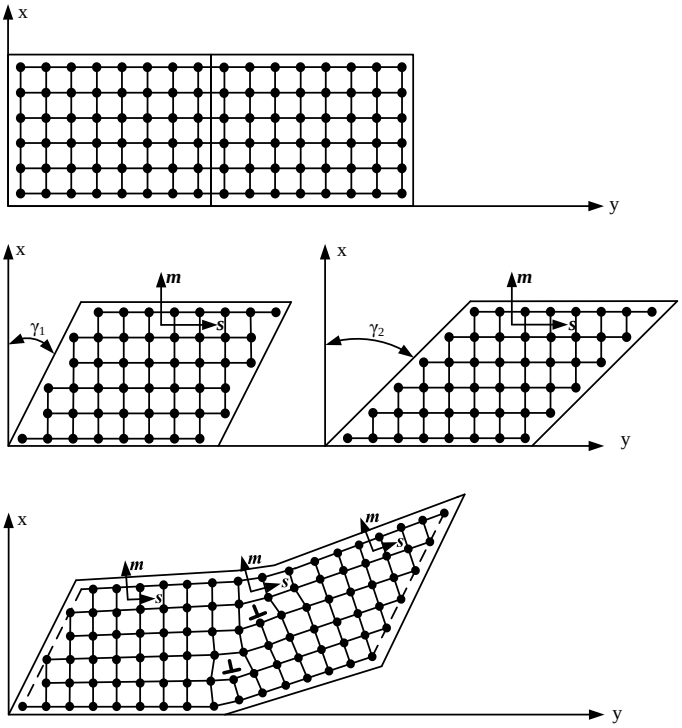

Figure 6: Introduction of GNDs for geometric compatibility in non-uniformly deformed regions

The increase in strength due to GNDs is accounted for in the crystal plasticity model following Han et al. (Han et al. 2005) by the determination of the total current strength g_{T}^{α} on a slip system α as the square root of the sum of the squares of the current strength contributions by SSDs and GNDs, denoted $g_{\mathrm{SSD}}^{\alpha}$ and $g_{\mathrm{GND}}^{\alpha}$:

$$g_T^\alpha = \sqrt{(g_{SSD}^\alpha)^2 + (g_{GND}^\alpha)^2}. \tag{2.19}$$

In the classical crystal plasticity, the evolution of the current slip resistance due to strain hardening on a slip system is given by:

$$\dot{g}_S^\alpha = \sum_\beta h_{\alpha\beta}\,\dot{\gamma}^\beta, \tag{2.20}$$

which only considers hardening due to SSDs. To account for the contribution of the geometrically necessary dislocations, their effective density n_G is needed. In the formulation following Han et al. (Han et al. 2005), the effective density is calculated by:

$$n_G^\alpha = \left| \boldsymbol{m}^\alpha \times \sum_\beta \boldsymbol{s}^{\alpha\beta} \nabla\gamma^\beta \times \boldsymbol{m}^\beta \right|, \tag{2.21}$$

where $\nabla\gamma$ is the gradient of the plastic shear and $\boldsymbol{s}^{\alpha\beta} = \boldsymbol{s}^\alpha \cdot \boldsymbol{s}^\beta$ ('·' denotes the scalar product). It has to be mentioned, that the unit of this effective density is μm^{-1} instead of the usually used μm^{-2}. The intrinsic length scale is introduced in the formulation in the equation for the slip resistance due to GNDs:

$$g_{GND}^\alpha = \tau_0 \sqrt{l n_G^\alpha}. \tag{2.22}$$

In this equation, τ_0 is the reference slip resistance and l the intrinsic length scale given by the following equation:

$$l = \frac{\alpha_T^2 \, G^2 \, b}{(\tau_0)^2}, \tag{2.23}$$

where the parameter α_T is ranging usually between 0.2 to 0.5, G is the shear modulus and b the magnitude of the Burgersvector.

2.6 Crystal lattice rotation

The crystal lattice rotation is of particular importance in this work since it characterizes the plastic deformation of the specimen and can be used for a comparison with experimental results determined in EBSD studies. Beyond that, it is the basis for further investigations of the density of geometrically necessary dislocations via the kernel average misorientation method (KAM).
In general, the lattice rotates during deformation which is visualized in figure 7. Two initially connected segments (ABCD) and (EFGH) are assumed to have the same slip system characterized by the slip direction $\boldsymbol{s}$ and slip plane normal $\boldsymbol{m}$. The two segments are assumed to undergo a different amount of plastic shear, described by the plastic part of the deformation gradient $\boldsymbol{F}^{\mathrm{p}}$. Thus, the two separated segments are translated into an intermediate deformation state. For compatibility reasons, elastic stretching and rotation α_z of the segments described by $\boldsymbol{F}^{\mathrm{e}}$ are necessary to transfer the two segments from the intermediate state into a shape in which the segments can be merged (represented by the two grey segments in the two bottom pictures of the figure 7).
The rotation matrix $\boldsymbol{R}$ is defined as a rotation from the initial to the current crystal configuration and can be determined as described in detail in appendix A.3. In crystallography, usually one of three ways are used to describe the rotation (Gottstein 2014). Crystal directions can be given that are parallel to the specimen's axes. A second way is the specification of a rotation axis and a rotation angle around this axis. A third possibility way are the three Euler angles. For the investigations in this work, the latter two are used. The Euler

angles following Bunge φ_1, Φ and φ_2 (Z-X-Z convention) can be calculated from the rotation matrix $\boldsymbol{R}$ based on the following relation:

$$\boldsymbol{R} = \begin{bmatrix} cos(\varphi_1)cos(\varphi_2) - sin(\varphi_1)sin(\varphi_2)\cos(\Phi) & sin(\varphi_1)cos(\varphi_2) - cos(\varphi_2)\sin(\varphi_1)\sin(\Phi) & \sin(\varphi_2)\sin(\Phi) \\ -cos(\varphi_1)\sin(\varphi_2) - sin(\varphi_1)\cos(\varphi_2)\cos(\Phi) & -sin(\varphi_1)\cos(\varphi_2) - cos(\varphi_1)\cos(\varphi_2)\cos(\Phi) & \cos(\varphi_2)\sin(\Phi) \\ \sin(\varphi_1)\sin(\Phi) & -\cos(\varphi_1)\sin(\Phi) & \cos(\Phi) \end{bmatrix}. \quad (2.24)$$

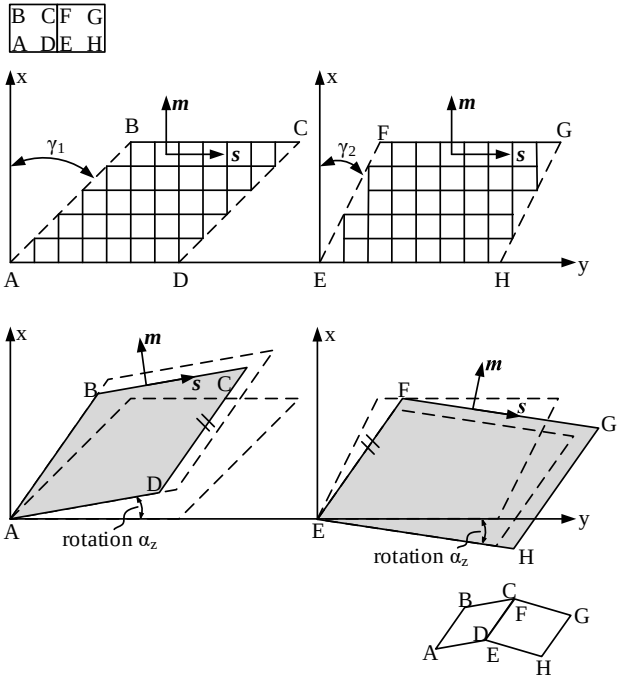

Figure 7: Intermediate states of deformation: a) different amount of pure shear of the two segments ABCD and EFGH, as described by $\boldsymbol{F}^{\mathrm{p}}$; b) elastic stretch and rotation needed to join the segments as described by $\boldsymbol{F}^{\mathrm{e}}$

Based on the rotation matrix, the three Euler angles can be determined following the three expressions:

$$\varphi_1 = \arctan\left(\frac{R_{31}}{R_{32}}\right) \tag{2.25}$$

$$\varphi_2 = \arctan\left(\frac{R_{13}}{R_{23}}\right) \tag{2.26}$$

$$\Phi = \arccos(R_{11}). \tag{2.27}$$

The special case of Φ being zero (or R_{11} being one) has to be considered separately to avoid a division by zero. In the case of $\Phi = 0$, the first and the second rotation (Φ and φ_1) are set zero and φ_2 is calculated based on R_{21} an R_{11}:

$$\frac{R_{21}}{R_{11}} = \tan(\varphi_2) \rightarrow \varphi_2 = \arctan\left(\frac{R_{21}}{R_{11}}\right). \tag{2.28}$$

For the determination of the rotation axis $\boldsymbol{u}$ and angle θ, following Gottstein (Gottstein 2014) , the relations between the matrix components and $\boldsymbol{u}$ and θ can be used:

$$\boldsymbol{R} = \begin{bmatrix} (1-u_1^2)\cos(\theta)+u_1^2 & u_1u_2(1-\cos(\theta))+u_3\sin(\theta) & u_1u_3(1-\cos(\theta))-u_2\sin(\theta) \\ u_1u_2(1-\cos(\theta))-u_3\sin(\theta) & (1-u_2^2)\cos(\theta)+u_2^2 & u_2u_3(1-\cos(\theta))+u_1\sin(\theta) \\ u_2u_3(1-\cos(\theta))+u_2\sin(\theta) & u_1u_3(1-\cos(\theta))-u_1\sin(\theta) & (1-u_3^2)\cos(\theta)+u_3^2 \end{bmatrix}. \tag{2.29}$$

The following two equations were used to determine the axis and angle in this work:

$$\theta = \arccos\left(\frac{Tr(\boldsymbol{R})-1}{2}\right), \tag{2.30}$$

$$\boldsymbol{u} = \begin{pmatrix} u_1 \\ u_2 \\ u_3 \end{pmatrix} = \begin{pmatrix} R_{32} - R_{23} \\ R_{13} - R_{31} \\ R_{21} - R_{12} \end{pmatrix}. \tag{2.31}$$

To be able to visualize the lattice rotation due to indentation, crystal plasticity user subroutine was extended. At each integration point, the orientation of the lattice in the deformed configuration is compared to the lattice orientation in the undeformed configuration. The rotation matrix $\boldsymbol{R}$ between these configurations is computed, which allows to obtain the axis of rotation with its rotation angle as well as Euler angles as described above.

3 Implementation

The extension of the conventional crystal plasticity subroutine for the determination of plastic shear gradients and the density of geometrically necessary dislocation is described in detail in this chapter. The mathematical formulations of the mechanism-based strain gradient crystal plasticity to determine the gradients of plastic shear in the finite-element framework are outlined. The sequence in which the user and utility subroutines are called are visualized in a flow chart for an overview of the extension. Further, a first simulation of a simple bar under traction and gravity load was performed with the MBSGCP subroutine for an evaluation of the implementation.

3.1 User subroutine

The constitutive laws presented in chapter 2 are implemented in the commercial finite element software package ABAQUS (Dassault Systèmes) via user subroutines. In every increment a user subroutine is called for every integration point (IPT). It is provided inter alia with the actual stress components, solution-dependent state variables (SDVs), coordinates of the IPT, the strain and time increment. These values are used for user-defined calculations. The subroutine updates the stresses and SDVs according to the implemented constitutive laws, calculates the Jacobian matrix $\delta\boldsymbol{\sigma}/\delta\boldsymbol{\varepsilon}$ and passes the results back. Data is only provided for integration points for which the user subroutine is called. Beside the user material subroutine, utility subroutines provided by ABAQUS are necessary to write and read output data to the result file.

3.2 Mechanism-based strain gradient crystal plasticity

Basis of the mechanism-based strain gradient implementation is the conventional crystal plasticity subroutine written by Huang (Huang 1991). All necessary extensions to the crystal plasticity subroutine according to the theory of Han et al. (Han et al. 2005) were written in Fortran 77. The implementation was performed for the general purpose linear brick elements C3D8 with 2 × 2 × 2 integration points and C3D8R elements with one integration point (see figure 8). The node and integration point numbering follows the convention shown in the figure. Dependent on the chosen element type, the procedure to determine necessary nodal values of plastic shear differs and both methods are described in this chapter. As mentioned above, the core idea of the mechanism-based strain gradient crystal plasticity formulation is the determination of an effective density of GNDs analog to the Peach–Koehler force in dislocation theory and to incorporate the additional strengthening due to GNDs in the constitutive law via the Taylor relation. The determination of strain gradients, i.e. the density of geometrically necessary dislocations in this work is based on the derivatives of shape functions (see appendix A.1) within finite elements and the calculation of averaged nodal values of plastic shear. A downside of this method is a higher computational effort because all nodal coordinates and averaged plastic shear values must be determined. However, this is accepted and outweighed by the possibility to use a commercial finite-element software with the possibility of using standard element types and simple model creations.

In the finite element method, field variables within every element are interpolated between nodes via shape functions, denoted N^{i} in the following. Table 2 lists the shape functions applicable for the chosen linear brick element type in local coordinates, denoted $\boldsymbol{\psi}$ or (ξ,η,ρ) in this work. So the displacement $\boldsymbol{u}_{\mathrm{IPT}}$, as an example, can be determined at integration points within an element with the nodal values $\boldsymbol{u}_{\mathrm{N}}$ and shape functions, following the equation:

$$\boldsymbol{u}_{IPT} = N^i(\boldsymbol{\psi})\boldsymbol{u}_N^i \quad \text{(sum over } i\text{)}. \tag{3.1}$$

The chosen element types possess same number of nodes and shape functions, whereas the number of integration points differs (eight in the C3D8 and one in the C3D8R element). One property of shape functions of an element is that they are one at one node of the element and zero at all other nodes (Bathe 1996). Per definition, the first shape function N^1 has the value one at the node with the local number one, shape function two, has the value one at the node number two and so on. The eight linear shape functions for linear brick elements are listed in the following table 2.

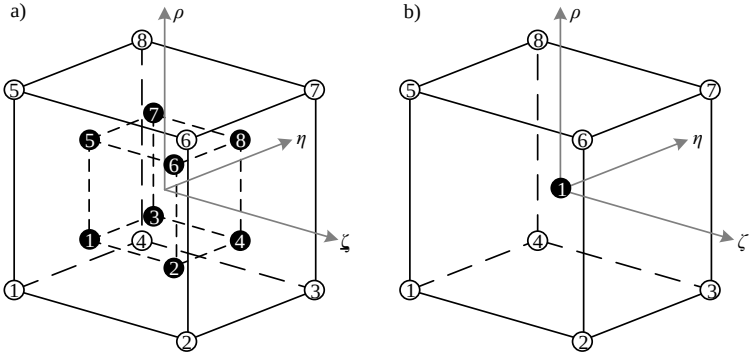

Figure 8: a) C3D8 element with eight nodes and eight integration points with local numbering b) C3D8R element with the unique integration point and the eight nodes with local numbering

Table 2: Shape functions expressed in local coordinates (ξ,η,ρ) for linear brick elements

i	N^i	i	N^i
1	$\frac{1}{8}(1-\xi)(1-\eta)(1-\rho)$	5	$\frac{1}{8}(1-\xi)(1-\eta)(1+\rho)$
2	$\frac{1}{8}(1+\xi)(1-\eta)(1-\rho)$	6	$\frac{1}{8}(1+\xi)(1-\eta)(1+\rho)$

3	$\frac{1}{8}(1+\xi)(1+\eta)(1-\rho)$	7	$\frac{1}{8}(1+\xi)(1+\eta)(1+\rho)$
4	$\frac{1}{8}(1-\xi)(1+\eta)(1-\rho)$	8	$\frac{1}{8}(1-\xi)(1+\eta)(1+\rho)$

3.2.1 Determination of plastic shear gradients

Like the displacement $\boldsymbol{u}$ shown in equation (3.1), the plastic shear on slip system α at an integration point $\gamma^{\alpha}_{\mathrm{IPT}}$ can be determined from nodal values $\gamma^{\alpha}_{\mathrm{N}}$ via the expression:

$$\gamma^{\alpha}_{\mathrm{IPT}} = N^{i}(\boldsymbol{\psi})\gamma^{\alpha i}_{\mathrm{N}} \quad \text{(sum over } i\text{)}. \tag{3.2}$$

In case of the chosen linear element type, the superscript i is a variable ranging from 1 to 8 referring to eight nodes and the eight shape functions. The derivatives of plastic shear regarding the global coordinates can be determined with the derivatives of the shape functions N:

$$\nabla\gamma^{\alpha}_{\mathrm{IPT}} = \frac{\partial\gamma^{\alpha}_{\mathrm{IPT}}}{\partial\boldsymbol{x}} = \frac{\partial\gamma^{\alpha}_{\mathrm{IPT}}}{\partial\boldsymbol{\psi}}\frac{\partial\boldsymbol{\psi}}{\partial\boldsymbol{x}} = \frac{\partial(N^{i}(\boldsymbol{\psi})\gamma^{\alpha\mathrm{i}}_{\mathrm{N}})}{\partial\boldsymbol{\psi}}\frac{\partial\boldsymbol{\psi}}{\partial\boldsymbol{x}}. \tag{3.3}$$

$\nabla\gamma^{\alpha}_{\mathrm{IPT}}$ is the gradient of the plastic shear of slip system α and $\boldsymbol{x}$ denotes the global coordinates (x,y,z). The expression of the global with respect to the local coordinates $\partial\boldsymbol{x}/\partial\boldsymbol{\psi}$ is called Jacobian matrix $\boldsymbol{J}$ so that the expression for the gradient of plastic shear can be written as:

$$\nabla\gamma^{\alpha}_{\mathrm{IPT}} = (N^{i}(\boldsymbol{\psi})\nabla_{\boldsymbol{\psi}})\gamma^{\alpha i}_{\mathrm{N}}\boldsymbol{J}^{-1} \quad \text{(sum over } i\text{)}. \tag{3.4}$$

In the expression, the term denoting the derivative of shape function in terms of the nabla operator $\nabla_{\boldsymbol{\psi}}$ can be rewritten:

$$N^i(\boldsymbol{\psi})\nabla_{\boldsymbol{\psi}} = \left(\frac{\partial N^i(\boldsymbol{\psi})}{\partial \xi}, \frac{\partial N^i(\boldsymbol{\psi})}{\partial \eta}, \frac{\partial N^i(\boldsymbol{\psi})}{\partial \rho}\right). \tag{3.5}$$

Not only field variables like displacement and plastic shear are connected between nodes and integration points via the shape functions but also the global coordinates $\boldsymbol{x}$:

$$\boldsymbol{x}_{IPT} = N^i(\boldsymbol{\psi})\boldsymbol{x}_N. \tag{3.6}$$

For the implementation in the subroutine, the Jacobian matrix is expressed dependent on the derivative of the linear shape functions following (Liang and Dunne 2009):

$$\boldsymbol{J} = \sum_{k=1}^{8} \begin{bmatrix} x_i \\ y_i \\ z_i \end{bmatrix} \otimes \begin{bmatrix} N_{i,\xi} \\ N_{i,\eta} \\ N_{i,\rho} \end{bmatrix}. \tag{3.7}$$

The inverse of the Jacobian matrix $\boldsymbol{J}^{-1}$ is calculated for every integration point of every element using Cramer's rule.

3.2.2 Averaging scheme

With the chosen element type, the displacements are interpolated linearly. As the strain $\boldsymbol{\varepsilon}$ is a derivative of the displacement $\boldsymbol{u}$, the strain is constant within elements. The same holds for the plastic shear γ^{α}. Consequently, the gradients of plastic shear within an element are zero. To be able to obtain plastic shear gradients in an element without the need of introducing higher order elements, nodal values of plastic shear of adjoining elements are averaged. These nodal values are subsequently used to calculate gradients of plastic shear at integration points of elements. The underlying idea of this approach is that plastic shear may differ significantly in adjoining elements as visualized in figure 9

showing a simple model consisting of four one-dimensional elements. By averaging the nodal values of a field variable, here the plastic shear, of adjoining elements sharing the same node, discontinuities at the nodes are eliminated. With the averaged values, the gradients of plastic shear can be determined within elements.

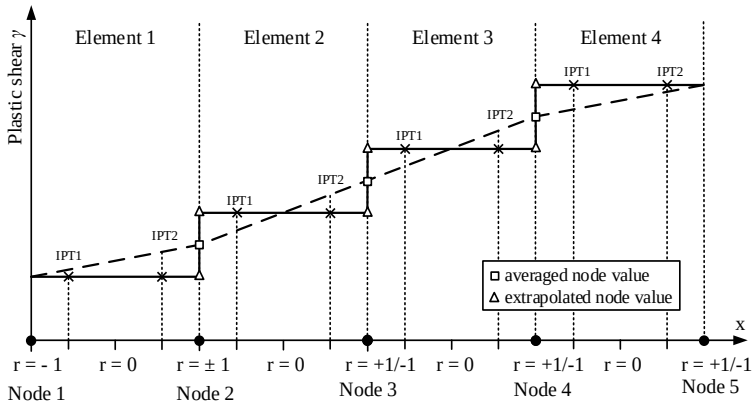

Figure 9: Actual and averaged nodal values of a field variable along four one-dimensional elements

3.2.3 Procedure overview

The extensions to be able to compute the plastic shear gradients can be divided into four steps executed in four different subroutines as described in the following (related to the flow chart of figure 10). For the steps necessary to calculate plastic shear gradients, in the output section of the input file, the global coordinates of all nodes have to be written to the result file in every increment via the keyword *NODE FILE. The necessary information about global element numbering and attached nodes are written to the result file by default and can be read at the end of every element together with the global node coordinates as described below in more detail.

Writing the plastic shear to a common block (UMAT): This step is necessary since all nodal values of plastic shear of an element have to be available to calculate the gradients of plastic shear at an integration. To the knowledge of the author, the only way to make the nodal values available i.e. share data, (here the plastic shear) at integration points between subroutines is to store the data in common blocks which are available in Fortran 77 (Stanford University 1995). This step is performed for the first time in the initial increment of the simulation the position denoted by the global integration point number. At the end of the first increment when the subroutine was called for every integration point, *"Gammaint1"* contains all global node numbers together with the plastic shear values. The values are used at the end of the increment to calculated the averaged values.
In the second increment, the averaged values of plastic shear at integration points are available for the first time for further calculations. According to the procedure in the initial increment, the plastic shear of every integration point is again written to *"Gammaint1"* in the second and all other increments to follow. The old values from the previous increment can be overwritten since they are no longer needed after the averaging scheme. It has to be noted that in this procedure, values from the previous increment of the plastic shear are used for operations in the current increment. However, by the knowledge of the author of this thesis, there is no alternative procedure to be in line to make all integration point values accessible.

Reading data from the result file (URDFIL): For the averaging of the nodal plastic shear values, the global element numbers with attached nodes must be known and are therefore read from the input file uniquely at the end of the first increment. These global node numbers are stored in the common block called *"Nodelem"* together with global number of the eight attached nodes. As mentioned, the global node numbers and attached nodes are written to the result file by default. Furthermore, the global coordinates of all element nodes that were written to the result file as described above, are read together with the global node numbers from the result file and saved in another common block

named *"Coordsk"*. These data are needed for the calculation of the inverse of the Jacobian matrix.

Averaging the nodal values (UEXTERNALDB): The averaging scheme is performed in the utility subroutine UEXTERNALDB which is called at the end of every increment. First, the integration point values of plastic shear have to be assigned to the element nodes. In case of C3D8R elements, the single integration point value is directly allocated to all eight element nodes. In case of the C3D8 elements, the extrapolation scheme following Busso (Busso et al. 2000) is applied to determine the nodal values:

$$\gamma_{IPT}^{\alpha i} = N^{i}(\boldsymbol{\psi})\gamma_{N}^{\alpha}. \tag{3.8}$$

The subroutine runs through all global element numbers in ascending order. Starting at the first element, the single integration point value of the element is assigned to all eight nodes in case of C3D8R elements. For C3D8 elements, the extrapolation scheme is applied. After this operation, the global element number, the global numbers of the eight attached nodes (from *"Nodeelem")* and the eight nodal values of plastic shear of the element are known. The next step is to save the nodal values of plastic shear in the common block "*Allgamma1"* at the position denoted by the global node number. This procedure is performed for every element. As a node is shared by different elements, its global node number is found several times as the subroutine runs through all elements. Every time a global node number appears, its plastic shear values is added at the position denoted by the global node number in "*Allgamma1"* and not overwritten. Additionally, a counter at the same position in the common block "*Nodeadjel"* is increased by one. Finally, "*Allgamma1"* contains the added up plastic shear values for all nodes which are then divided by the value of the corresponding counter in "*Nodeadjel"*. These averaged values are again saved in "*Allgamma1"* and used in the following increment to determine the gradients of plastic shear.

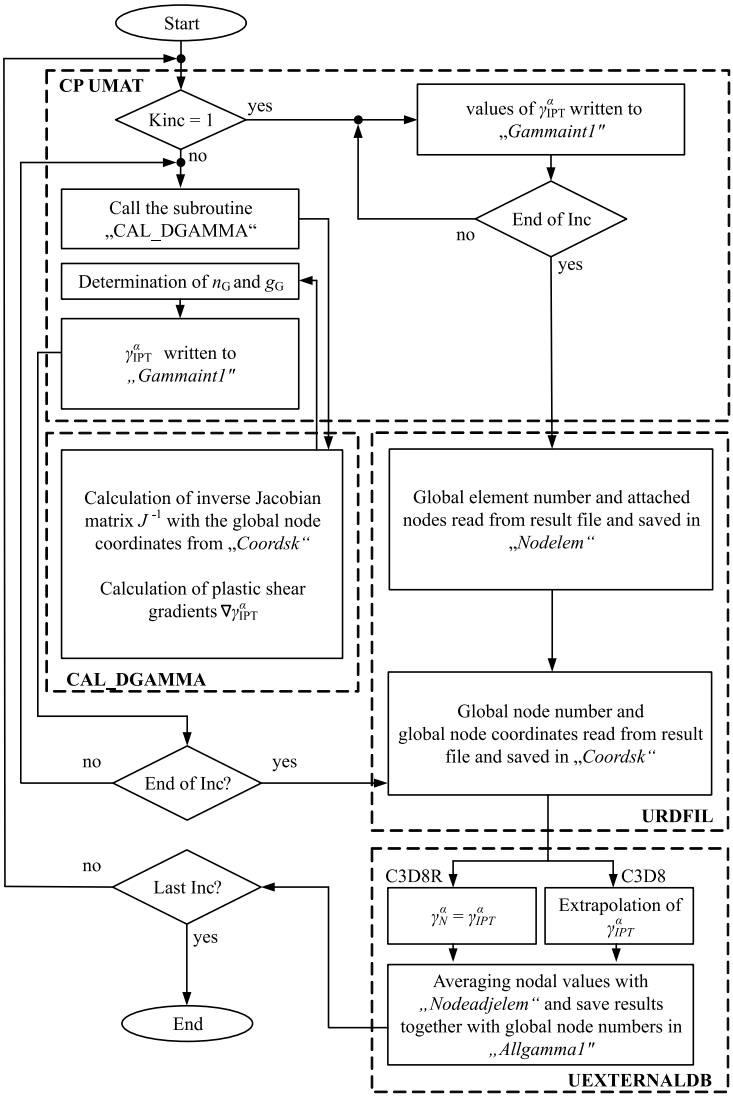

Figure 10: Flow chart of the MBSGCP extension as an addendum to the conventional crystal plasticity user-material subroutine

Calculation of plastic shear gradients (CAL_DGAMMA): In all increments other than the initial, the calculation of the gradients is the first step. For this, the subroutine CAL_DGAMMA is called in which the inverse of the Jacobian matrix and the gradients of the plastic shear are calculated based on the data of the previous increment. This procedure is performed every time the subroutine is called for an integration point in the current increment.

The implementation of the mechanism-based strain gradient crystal plasticity was performed for both, the C3D8 and the C3D8R elements. However, only the elements with reduced integration are used in this thesis. The reasons are the lower cost of computational time and more stability in non-linear simulation with contact.

All common blocks used in this work are listed in appendix A.2.

3.3 Influence of gradients of plastic shear on a bar under tensile and gravity load

For an evaluation of the mechanism-based strain gradient crystal plasticity implementation regarding strain gradients and the ability to describe the size dependency, simple bar-shaped ten element model were set up with different lengths and cross sections (figure 11). Simulations with the conventional and mechanism-based strain gradient crystal plasticity were performed and compared. The simple bar-shaped model is inspired by the analytical investigations of Huang et al. (Huang et al. 2004). The model consists of ten regular hexahedron shaped elements (C3D8R) with the side length h (see figure 11). The four nodes at the top of the bar are fixed in all three directions, whereas the four nodes at the bottom of the bar are fixed in the z- and x-direction but unconstrained in the y-direction. Two loads were defined, namely a traction on the bottom surface of the bar and a gravity load to induce a gradient along the y-direction. A value of 0.8 mN/µm^2 was chosen for the traction $\boldsymbol{t}$ in the negative y-direction. The gravity load $\boldsymbol{g}$ was set to 4.25 $\cdot 10^{14}$ µm/s^2 for the smallest bar with a length of 0.1 µm and decreased for the larger models. Together with the

gravity load, the density of tungsten $\rho = 19.3 \cdot 10^{15}$ kg/µm^3 was defined. For the investigation of the size dependency, five models with different side lengths h and overall length l_0, ranging from 0.1 to 100 µm were set up. The dimensions of the bars are listed together with the loads in the following table 3. The overall length of the bar l_0 in the different models is always ten times the side length h of one element. To achieve the same stress conditions in the different sized bars, with different lengths and cross-sections, the traction $\boldsymbol{t}$ on the bottom face was defined constant in all models. The analytic equation for the calculation of the stress distribution $\sigma(x) = \boldsymbol{t} + \rho \boldsymbol{g} x$, shows that the gravity load $\boldsymbol{g}$ needs to be reduced by the same factor as the length of the bars is increased (listed in table 3) for the same stresses within the bars.

Table 3: Dimensions and loads defined in the ten element bar simulations

l_0 in µm	$h \times h$ in µm^2	$\boldsymbol{g}$ in $\frac{\mu m}{s^2}$	$\boldsymbol{t}$ in $\frac{mN}{\mu m^2}$
0.1	0.01 × 0.01	$4.25 \cdot 10^{14}$	0.8
0.25	0.0125 × 0.0125	$1.7 \cdot 10^{14}$	0.8
1.0	0.1 × 0.1	$4.25 \cdot 10^{13}$	0.8
10.0	1.0 × 1.0	$4.25 \cdot 10^{12}$	0.8
100.0	10.0 × 10.0	$4.25 \cdot 10^{11}$	0.8

The material parameters for the simulation correspond to those chosen in the single-layer MBSGCP wedge nanoindentation simulation described in chapter 5. Moreover, slip was defined to occur on the {110}⟨111⟩ slip systems.

The conventional crystal plasticity model does not regard for an internal length scale. Hence, the same linear stress distribution in all differently sized bars leads to the same strain conditions and no dependency on the length of the bar occurs. However, the gradient of ε_{xx} increases with decreasing length of the bars. The mechanism-based strain gradient crystal plasticity model accounts for this fact by calculating higher strengthening on slip systems as the gradients increase and thus accounts for a size-dependency.

The formulation of the mechanism-based strain gradient crystal plasticity contains an intrinsic length scale that defines a border under which a size dependency occurs:

$$l = \frac{\alpha^2 G^2 b}{{g_0}^2}. \tag{3.9}$$

For tungsten, the empirical coefficient α was set 0.3, the shear modulus μ = 160 GPa, the magnitude of the Burgersvector b = 0.27 nm and the reference slip resistance g_0 = 210MPa in this equation. With these values, the intrinsic length scale l = 14 µm was calculated. Simulations with characteristic lengths (length of the bar) under 14 µm will therefore exhibit a size dependency. The models described above were used to simulate bars under traction and gravity load. The crystal orientation was defined so that the local and global coordinates coincident (see figure 11). The loading duration was set to 1 s with a constant increment size of 0.001 s. Figure 12 shows the total cumulative plastic shear along the bar in the y-direction for all models using the mechanism-based strain gradient and the conventional crystal plasticity subroutine. The total cumulative plastic shear is a measure for the plastic deformation of the bar and therefore well suited for an investigation of the size dependency. The figure shows that the cumulative shear stress along an edge of the bar in y-direction is the same for MBSGCP simulation of the bar with 100 µm length and the conventional crystal plasticity simulations. The results show that in the conventional CP simulation, no size dependency occurs. With the MBSGCP a slight decrease of the cumulative plastic shear occurs for the bar with the length of 10 µm in comparison to the 100 µm long bar. As the length of the bar is further decreased, the occurring cumulative plastic shear decreases significantly and is only about 30% as the length is decreased from 100 µm to 0.1 µm by the factor of 1000. The reason for the decline can be explained by the additional hardening occurring on slip systems due to GNDs. The smaller the length of the investigated bar, the higher the occurring gradients of plastic shear and with that the density of GNDs. Consequently, the strengthening on

slip systems increases and with that the resistance of the bar against plastic deformation increases as well. For all bars, the maximum plastic shear on slip systems occurs about 3.5 µm under the clamping of the bar where the maximum necking occurs.

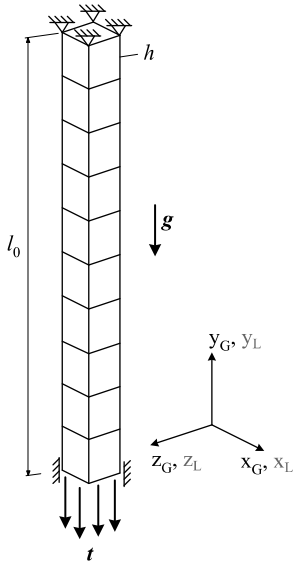

Figure 11: Ten element bar-shaped model for the investigation of strain gradients and size dependency with the defined gravity load and traction on the bottom face of the bar

The comparison of cumulative plastic shear shows a small difference between the 100 µm and 10 µm long bars but a significant decrease as the lengths of the rods decreases to 1 µm, 0.25 µm and 0.1 µm. This observation confirms the calculated intrinsic length scale of about 14 µm, meaning that above this vale no size-dependency occurs.

Figure 12 shows in addition the elongation $\Delta l/l_0$ of the different bars dependent on the loading duration on the right. The curves of all conventional CP simulations and the ones from the MBSGCP 10 µm and 100 µm simulations are

similar. With decreasing length of the bars, the results of the MBSGCP simulations show a significant decrease of $\Delta l/l_0$, confirming the higher strengthening of slip systems at smaller length of the bars.
Figure 13 shows the plastic shear on the twelve slip systems plotted over the true distance in y-direction. The simulation results show that for all models, four slip systems are not activated. Four slip systems, namely number 2, 5, 11 and 12 are positive and slip systems 1, 6, 7 and 8 are negative, following the ABAQUS internal numbering. The shapes of the curves exhibit a symmetry with respect to the x-axis.

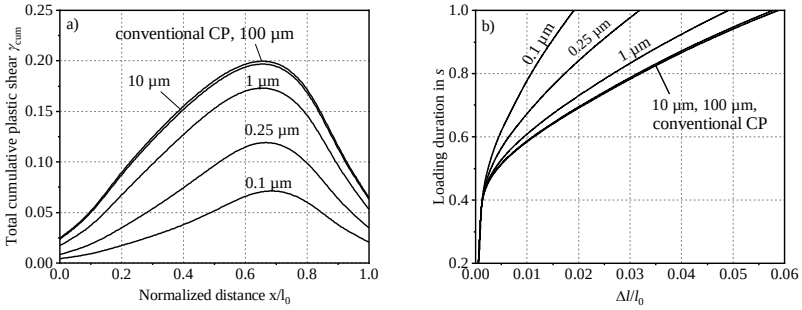

Figure 12: a) total cumulative plastic shear along the bars in y-direction; b) plastic strain along the different bars in y-direction

For further investigations of the strain gradients, two approximation function $f^1(x) = -f^2(x)$ drawn as dotted line in figure 13 were fitted to the curves, following:

$$f^1(x) = -0.252x^5 - 0.61x^4 + 0.42x^3 - 0.09x^2 + 0.035x + 0.002. \qquad (3.10)$$

The derivatives of the functions $f^1(x)$ and $f^2(x)$ are shown in Figure 13. In addition, the graph shows the simulation results of the plastic shear gradient in y-direction along an edge of the bar. Both, the analytical calculated derivatives of the approximation functions and the simulation results for the plastic shear

gradients in y-direction are similar. This proves the ability of the subroutine to calculate the plastic shear gradients accurate.

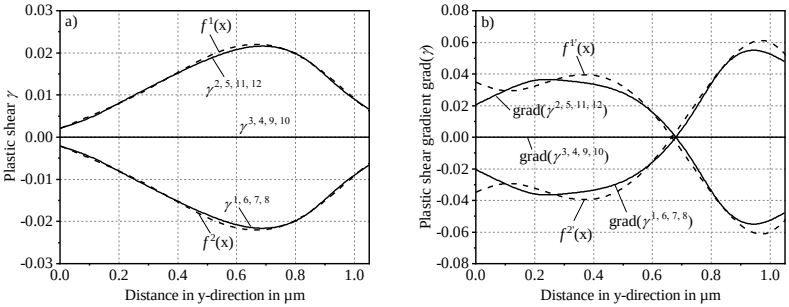

Figure 13: a) plastic shear on each slip system along the edge of the bar with the length of 1 µm in y-direction; b) derivatives of the functions $f^1(x)$ and $f^2(x)$ together with the computed strain gradients along the edge of the bar with the length of 1 µm in y-direction

4 Summary of experimental results

The numerical results of this work are compared to the nanoindentation experiments performed by J. Wang at the Institute of Applied Materials (IAM-WBM) at the Karlsruhe Institute of Technology (KIT). The comparison is performed in chapter 6.6 for the deformed geometry, crystal lattice rotation and density of geometrically necessary dislocations for the bridge-shaped model. A comprehensive description of the sample fabrication, preparation and experimental indentation procedure can be found in the Phd-thesis of Wang, which was in the completion parallel to this work. A brief summary of the experiments is given in the following.

The static wedge nanoindentation test was performed using a Nano Indenter G200 (Agilent Technologies, Keysight, KLA-Tencor) and a 90° diamond nanoindenter. A load-controlled indentation process to achieve different constant strain rates was chosen. The maximum indentation depth in the wedge nanoindentation test was set to 2 µm.
The fabrication of the sample, called bridge in the following, was performed by Wang in two steps, first the preparation of the surface of the single crystal and second the actual cutting of the bridge. In the first step, the surface was mechanically polishing using SiC-paper and subsequently cloth and diamond suspension. Last, the surface was electrolytically polished. In the second step, focused ion beam (FIB) was used to cut the final form of the bridge shown in figure 14 a) before the indentation test was performed. The geometry of the experiment is shown in figure 14 before and after the indentation in a) and b), respectively. The bridge has a length of approximately 22.26 µm and a width of 3.507 µm.

For the determination of the crystal lattice rotation and GND density, FIB was used to cut the TKD lamella, representing the midsection, with a width of about 200 nm after the indentation (see Figure 14 b)). The lamella was then used for the following EBSD investigations to determine the initial crystal orientation

and lattice rotation under the indent after the indentation. The crystal lattice rotation data were used for the further investigations of the distribution and density of geometrically necessary dislocations.

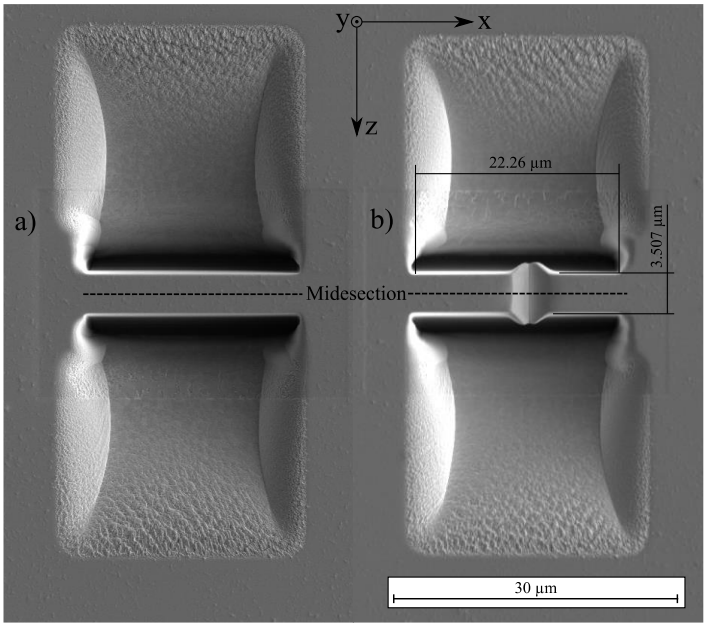

Figure 14: a) initial shape of the bridge before the indentation; b) residual imprint in the bridge after indentation with the 90° wedge indenter

The investigations via EBSD carried out by Wang revealed a normal to the indented surface (global y-direction in figure 14) parallel to an edge of the unit cell, i.e. a ⟨100⟩ direction. Furthermore, a surface diagonal, corresponding to a $\langle\bar{1}10\rangle$ direction was determined to be parallel to the global x-direction. The specimen's geometry and crystal orientation were the basis for the definition of the so-called bridge shaped model used for the numerical wedge nanoindentation simulations.

5 Finite element modeling

For the numerical investigation of wedge nanoindentation using the conventional, non-Schmid and strain-gradient crystal plasticity model, suited FE-models are necessary. Therefore, three models were set up, namely the brick-shaped model, the single-layer model and the bridge-shaped model, each discretized with general purpose linear brick elements with reduced integration (C3D8R). A comprehensive element study was performed to guarantee and independence of results on the mesh. The results of the study can be found in appendix A.8 to A.10. While the brick-shaped model is used with the conventional and non-Schmid CP as material law, the single-layer model is applied in the mechanism-based strain gradient crystal plasticity simulation. The two models were used for principal investigations of the deformation behavior of tungsten. The bridge-shaped model was set up for simulations to be compared with experimental results using the conventional and non-Schmid crystal plasticity material model. The analysis was mainly performed in the midsection of the three models (highlighted in figure 16, figure 17 and figure 18) where all models have the same mesh in the contact region. The first part of this chapter covers the chosen crystal orientation for the investigations. Secondly the three different models are described in detail and finally, the material parameters used for the simulations are listed at the end of this chapter.

5.1 Crystal orientation

The investigations in this work were performed for two crystal orientations, namely the $[0\bar{1}0](101)$ and $[123](11\bar{1})$ orientation (called $[0\bar{1}0]$ and [123] orientation, respectively in the following). The first vector denotes the direction of indentation and the second the normal to the midsection in which the results

are evaluated (see figure 15) in the crystal coordinate system. In both orientation, the indenter is aligned parallel to the global [001] direction and indents the crystal in global [010] direction.

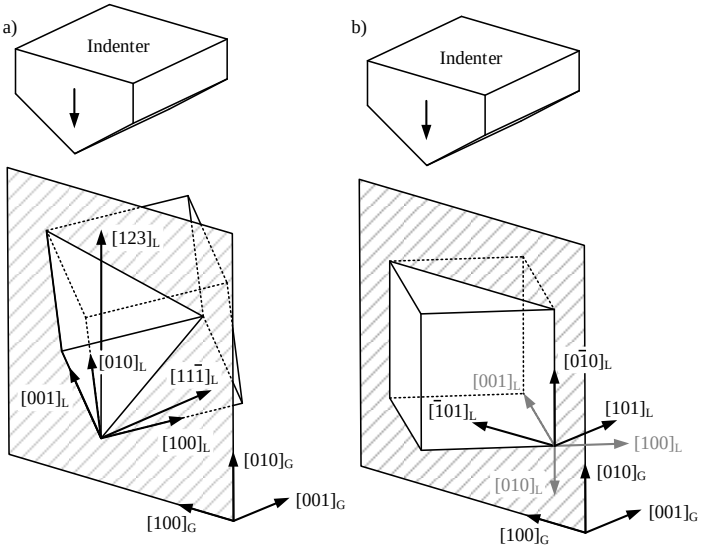

Figure 15: Visualization of the [123] and [010] oriented single crystal in a) and b) with respect to the midsection and the indenter tip parallel to the global (0$\bar{1}$0) direction

5.2 Brick-shaped model

This model consists of two parts, namely the rigid 90° wedge indenter with a flat tip and the deformable specimen shaped like a brick giving this model its name. The dimensions of the specimen are h = 40 µm, l = 80 µm and w = 70 µm (see figure 16). The dimensions of the specimen are chosen to guarantee that boundaries do not influence the simulation results. The indenter is modelled as an analytic surface. The exact shape of the indenter tip is not important as long as it is smaller than the minimal node distance since contact between

the indenter and the specimen is only determined between nodes and the analytic surface (Reuber et al. 2014). The indenter tip radius in the experiments is about 100 nm which corresponds to the minimal node distance in the simulation and is therefore assumed to have no influence on the simulation results.

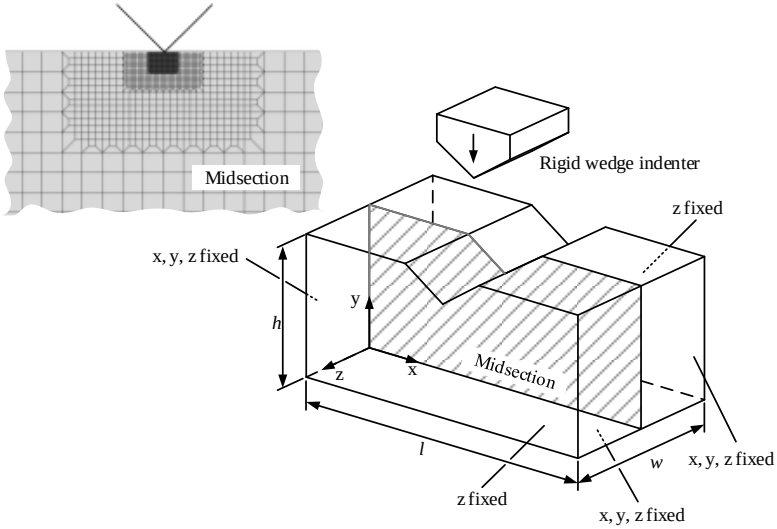

Figure 16: Brick-shape model with boundary conditions and the refined FE-mesh in the midsection of the model

The nodes on the front, the back and the top surface of the specimen are free in all directions, while those on the sides and the bottom are fixed in all directions. A displacement boundary condition is defined for the indenter to simulate the displacement controlled indentation process. The direction of indentation is parallel to the global $[0\bar{1}0]$ direction. The contact between the indenter and the specimen is defined as hard contact with Coulomb friction. Eight layers of elements were defined in the global z-direction with a length of 8.75 µm. Right underneath the indenter, where the indenter and specimen are in contact, the mesh is much finer than in the unaffected regions (see figure 16) in order

to keep computational time reasonable. The minimal element size under the indenter is 0.1 µm in the y-direction and 0.1 µm in the x-direction. Overall, the specimen is discretized by 19024 C3D8R elements.

5.3 Single-layer model

The single-layer model consists of the specimen and the 90° rigid wedge indenter. While the length l = 80 µm and the height h = 40 µm are the same than as in the brick-shaped model, the width w, discretized with only one element, is solely 0.1 µm. The wideness corresponds to the size of the smallest element under the indenter. The mesh corresponds to the one defined in the brick-shaped model shown in figure 16. However, the model consists only of 2378 C3D8R elements which is only an eighth of the elements used in the brick-shaped model. Just like in the brick-shaped model, the side and bottom faces are fixed in all directions and the top face is unrestricted. Additionally, the displacements of nodes on the front and back faces of the specimen are restricted in the z-direction.

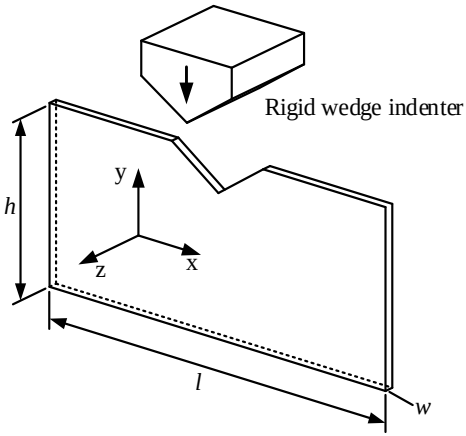

Figure 17: Single-layer model consisting of the deformable specimen and the rigid 90° wedge indenter

5.4 Bridge-shaped model

For a comparison of the simulation carried out in this work and the experimental results of J. Wang, the third model, namely the bridge-shaped model was set up. The mesh in the midsection is similar to the mesh shown in figure 16 in the indented region. Ten elements were defined in over the width of the bridge. The overall length and height and width of the indented bridge is l = 25 µm, h = 10 µm and w = 4.3 µm, respectively. The geometry represents the dimensions of the experimental indented bridge. To match the conditions of the experiments, additional material around the bridge was modeled with the overall size of 33 µm × 12.6 µm × 16 µm (length × width × height). Node displacement on the side, front, back and bottom surfaces are fixed in all directions (see figure 18). The top surface and the front and back face of the indented bridge are unrestricted. Like the brick-shaped and single-layer model, the bridge-shaped model consists of two part, the rigid indenter and the deformable specimen. The specimen is discretized with 25447 C3D8R elements.

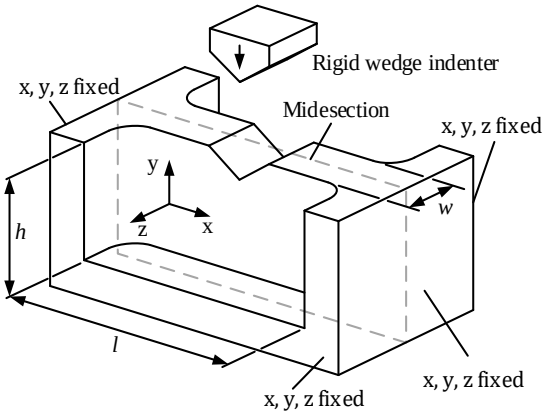

Figure 18: Bridge-shape model consisting of the deformable specimen and the rigid 90° wedge indenter

5.5 Input parameters

The described conventional, non-Schmid and mechanism-based strain gradient crystal plasticity material models are together with their material parameters the basis for the numerical investigations. The material parameters describing elasticity C_{11}, C_{12}, C_{44}, the viscoplastic deformation n, $\dot{\gamma}_0^\alpha$ and the hardening h_0, τ_s, τ_0 and q have to be defined. For the simulations using the non-Schmid crystal plasticity subroutines, additionally, the material parameters a_1, a_2, a_3 and for the MBSGCP simulation, the parameters G, $\boldsymbol{b}$ and α are necessary. For every simulation, a maximum step time of 0.000075 s and an indentation depth of 2 µm were defined.

Elastic constants

The anisotropic elastic deformation behavior of crystalline materials is generally described by the elastic tensor. For cubic crystals, the elastic tensor is completely defined by the three tensor components C_{11}, C_{12} and C_{44}. Tungsten single crystals can be assumed to deform elastically almost isotropic. The experimental isotropic constants that are used in this work were taken from (Liu et al. 2009) and are listed in the following table 4.

Table 4: Elastic constants of tungsten single crystal as input parameters for the user material subroutines (Liu et al. 2009)

Elastic constants	Experimental value in GPa
C_{11}	532.6
C_{12}	204.9
C_{44}	163.1

Viscoplastic parameters

The viscoplastic deformation behavior of the tungsten single crystal is described by the reference shear rate $\dot{\gamma}_0^\alpha$ and strain rate sensitivity exponent n. Both parameters can be found in the literature, e.g. (Liu et al. 2009). Following (Zambaldi and Raabe 2010), $\dot{\gamma}_0^\alpha$ and n are more numerically meaningful and

less related to mechanical properties of the single crystal. High strain rate sensitivity exponents n > 100 can suppress the strain rate sensitivity. The defined parameters are listed in the following table 5 for the {110}⟨111⟩ slip systems.

Table 5: Viscoelastic parameters of tungsten single crystal as input parameters for the user material subroutines

Viscoelastic parameter	Defined value
$\dot{\gamma}_0^{\alpha}$	10^{-4}
n	20

Hardening parameters

Strengthening of the single crystal is described by the evolution equation (2.11) following Peirce, Asaro and Needleman (PAN) (Peirce et al. 1982). The necessary input parameters of the PAN-hardening model are the initial hardening modulus h_0, the stage I stress τ_s, the yield stress τ_0 and the parameter q. The parameters were determined by Yao (Yao 2012) for tungsten single crystal Berkovich nanoindentation simulations and taken for the investigations in this work. Table 6 lists the values of the four parameters for the {110}⟨111⟩ slip systems applied in all simulations.

Table 6: Hardening parameters of tungsten single crystal as input parameters for the user material subroutines

Hardening parameter	Defined value
h_0	1350 MPa
τ_s	530 MPa
τ_0	210 MPa
q	1.4

MBSGCP input parameters

Beside the input parameters in the material card of the conventional crystal plasticity user subroutine (Huang 1991), the magnitude of the Burgersvector b and the parameter α need to be defined for the calculations.

Table 7: Additional input parameters in the mechanism-based strain gradient crystal plasticity simulations

MBSGCP parameter	Defined value
b	0.27 nm
α	0.3

Non-Schmid input parameters

For the non-Schmid simulations, the three constant material parameters a_1, a_2 and a_3 were defined for tungsten following Gröger et al. (Gröger et al. 2008b). As described above, a_1 represents the contribution due to the twinning and anti-twinning asymmetry and is zero. The parameters a_2 and a_3 are given in the following table 8.

Table 8: Additional input parameters in the non-Schmid crystal plasticity simulations

NOS parameter	Defined value
a_1	0.0
a_2	0.56
a_3	0.75

Friction

Coulomb friction was chosen in the contact definition between the diamond indenter and the polished tungsten single crystal. The coefficient of friction (COF) was found to have a significant influence in particular on the material pile-up and load-displacement curves (see appendix A.4), however, the exact value in the experiments is not known. The study of the COF performed in this thesis showed that low values in the rage between μ=0.0 and μ=0.1 result in unrealistic distortion of the elements in contact with the indenter. Higher values in the range of μ=1.0 are also unrealistic for a contact between polished tungsten and the diamond indenter. So a value μ=0.2 is seen as appropriate and was chosen for the simulations in the course of this work. A similar value of μ=0.15 was proposed by Engineering ToolBox (Engineering ToolBox 2004).

6 Results and discussion

6.1 Results of the [0$\bar{1}$0] oriented brick-shaped conventional CP simulation

The brick-shaped model was used together with the conventional crystal plasticity subroutine to simulate 90° wedge nanoindentation into the tungsten single crystal. For the study of strain gradients and non-Schmid effects and their influence on plastic deformation of the single crystal at the microscale in the following chapters, results in the midsection of the brick-shaped conventional crystal plasticity model serves as reference. Plastic deformation behavior i.e. activity of slip systems, the stress state, plastic shear rate, crystal lattice rotation and the GND density under the indent was investigated for both, the [0$\bar{1}$0] and [123] orientation with the conventional crystal plasticity model.

6.1.1 Slip system activity

The FE-model described in chapter 5 was applied to simulate 90° wedge indentation in the tungsten single crystal. The indenter tip was aligned parallel to the global [001] direction and indented the crystal in the [0$\bar{1}$0] direction with a speed of 2 µm/s and a maximum time increment size of $7.5 \cdot 10^{-5}$ s up to the defined indentation depth of 2 µm. Plastic shear is expected to occur on the $\{110\}\langle 111\rangle$ slip family which was defined in the subroutine together with the material parameters described in chapter 5.5. The slip directions and slip plane normals of all slip systems are listed in table 9 in local and global coordinates together with the numbering as defined in the subroutine.
The evaluation of computed plastic shear shows that it is either zero or very small on six of the twelve potentially active slip systems compared to the six slip systems that are active in the midsection. Plastic shear occurs solely on

slip system 2, 5, 8, 9, 10 and 12 (see figure 19), whereas slip systems 1, 3, 4, 6, 7 and 11 are inactive.

Table 9: Slip plane normal and slip directions in the $[0\bar{1}0]$ oriented specimen in local and global coordinates

slip system	**local (crystal)**		**global (specimen)**	
α	$\boldsymbol{m}_{\mathrm{L}}^{\alpha}$	$\boldsymbol{s}_{\mathrm{L}}^{\alpha}$	$\boldsymbol{m}_{\mathrm{G}}^{\alpha}$	$\boldsymbol{s}_{\mathrm{G}}^{\alpha}$
1	$[011]$	$[1\bar{1}1]$	$(1,-\sqrt{2},1)$	$(0,1,\sqrt{2})$
2	$[011]$	$[11\bar{1}]$	$(1,-\sqrt{2},1)$	$(-\sqrt{2},-1,0)$
3	$[101]$	$[\bar{1}11]$	$(0,0,1)$	$(\sqrt{2},-1,0)$
4	$[101]$	$[11\bar{1}]$	$(0,0,1)$	$(-\sqrt{2},-1,0)$
5	$[110]$	$[\bar{1}11]$	$(-1,-\sqrt{2},1)$	$(\sqrt{2},-1,0)$
6	$[110]$	$[1\bar{1}1]$	$(-1,-\sqrt{2},1)$	$(0,1,\sqrt{2})$
7	$[0\bar{1}1]$	$[111]$	$(1,\sqrt{2},1)$	$(0,-1,\sqrt{2})$
8	$[0\bar{1}1]$	$[\bar{1}11]$	$(1,\sqrt{2},1)$	$(\sqrt{2},-1,0)$
9	$[10\bar{1}]$	$[111]$	$(-1,0,0)$	$(0,-1,\sqrt{2})$
10	$[10\bar{1}]$	$[1\bar{1}1]$	$(-1,0,0)$	$(0,1,\sqrt{2})$
11	$[\bar{1}10]$	$[111]$	$(1,-\sqrt{2},-1)$	$(0,-1,\sqrt{2})$
12	$[\bar{1}10]$	$[11\bar{1}]$	$(1,-\sqrt{2},-1)$	$(-\sqrt{2},-1,0)$

In the $[0\bar{1}0]$ orientation, always two of the six active slip systems exhibit the same absolute value for the resolved shear stresses and consequently the same amount of plastic shear, namely slip system 2 and 12, slip system 5 and 8 as well as slip system 9 and 10. Therefore, it is sufficient to show plastic shear solely for slip system 2, 5 and 9 representing all active slip systems. The distribution of plastic shear γ^2, γ^5 and γ^9 in the midsection is given in figure 19 at the indentation depth of 2 µm. The contour plots of slip system 2 and 5 are mirrored with respect to the indentation direction.

The corresponding slip systems either possess the same slip directions or slip planes (see table 9). The Schmid-tensors of the active slip systems are listed in the appendix A.5 showing that for all active slip systems, the components P_{33} are zero. The components P_{31}, P_{13}, P_{23} and P_{32} do not influence the resolved shear stress on the slip systems since the stress components σ_{13} and σ_{23} are zero

in the midsection of the brick-shaped model due to the high symmetry of the chosen [0$\bar{1}$0] orientation.

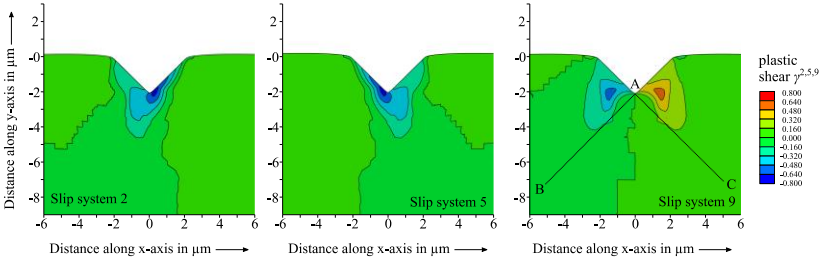

Figure 19: Slip system activity of slip systems 2, 5 and 9 (corresponding to slip system 12, 8 and 10 respectively) in the midsection of the conventional crystal plasticity brick-shaped simulation underneath the indent at the indentation depth of 2 µm.

The Schmid-tensors of the active slip systems reveal, that the components P_{11}, P_{12}, P_{21} and P_{22} of corresponding slip systems are either the same or differ by their sign. Consequently, the coherences $\tau^2 = \tau^{12}$, $\tau^5 = -\tau^8$ and $\tau^9 = -\tau^{10}$ of the resolved shear stresses on corresponding slip systems can be determined. Figure 20 b) illustrating the slip directions and slip planes of the corresponding slip systems in the initial state, shows that slip systems 2 and 12 have the same slip direction lying in the midsection under an angle of 35.3° to the surface of the specimen. Slip systems 5 and 8 have the same slip directions within the midsection under an angle of 35.3° as well but are mirrored to the slip directions of slip system 2 and 12 with respect to the indenter axis. Slip systems 9 and 10 have different slip directions but they lie in the same slip plane, which is normal to the midsection.

Following Rice (Rice 1987), it is useful to define three effective slip systems based on each two corresponding slip systems, consisting of an effective slip direction and slip plane in the midsection resulting in the same Schmid-tensor than the combination of corresponding slip systems. These effective slip systems based on slip system 2 and 12, 5 and 8 as well as 9 and 10 are shown in figure 20 c) in the initial state. The effective slip system based on slip system

2 and 12 is mirrored to the effective slip system based on slip system 5 and 8. The combination of slip system 9 and 10 results in effective plastic shear solely in vertical direction (i.e. in indenter direction) with a slip plane orthogonal to the midsection.

As slip system 2 and 12 possess the same resolved shear stress, their plastic shear rate corresponds as well. This means that $\dot{\gamma}_s^2 = \dot{\gamma}_s^{12}$, where the subscript *s* denotes the results of the conventional crystal plasticity simulation. Consequently, the combined rate of stretching $\boldsymbol{D}_s^{2/12}$ of the two slip systems can be determined by:

$$\boldsymbol{D}_s^{2/12} = \dot{\gamma}_s^2 \boldsymbol{P}_s^2 + \dot{\gamma}_s^{12} \boldsymbol{P}_s^{12}. \tag{6.1}$$

As the slip directions $\boldsymbol{s}^2$ and $\boldsymbol{s}^{12}$ are the same, the expression can be reduced to:

$$\boldsymbol{D}_s^{2,12} = \frac{\dot{\gamma}_s^{2/12}}{2} [\boldsymbol{s}^2 \otimes (\boldsymbol{m}^2 + \boldsymbol{m}^{12}) + (\boldsymbol{m}^2 + \boldsymbol{m}^{12}) \otimes \boldsymbol{s}^2]. \tag{6.2}$$

With the slip directions and slip plane normal vectors for the two slip systems *2* and 12, the rate of plastic stretching can be determined:

$$\boldsymbol{D}_s^{2/12} = \dot{\gamma}^{2/12} \begin{pmatrix} -2\sqrt{2} & 1 & 0 \\ 1 & 2\sqrt{2} & 0 \\ 0 & 0 & 0 \end{pmatrix} = \dot{\gamma}^{2/12} \boldsymbol{P}_s^{2/12,eff}. \tag{6.3}$$

$\boldsymbol{P}_s^{2/12,\,\mathrm{eff}}$ is the effective Schmid-tensor resulting from the combination of slip systems 2 and 12. This effective slip system leads to plastic shear in the midsection under an angle of 35.3° to the horizontal surface of the specimen (figure 20 c). The shear components D_{13}, D_{23}, D_{31} and D_{32} are zero in the resulting rate of stretching.

The similar procedure is performed in the appendix A.67A.6 for slip system 9 and 10 as well as 5 and 8 resulting in the rate of plastic stretching $\boldsymbol{D}_s^{5/8}$ and $\boldsymbol{D}_s^{9/10}$:

$$\boldsymbol{D}_s^{5/8} = \dot{\gamma}_s^{5/8} \begin{pmatrix} -2\sqrt{2} & -1 & 0 \\ -1 & 2\sqrt{2} & 0 \\ 0 & 0 & 0 \end{pmatrix} = \dot{\gamma}^{5/8} \boldsymbol{P}_s^{5/8,eff}, \tag{6.4}$$

$$\boldsymbol{D}_s^{9/10} = \dot{\gamma}_s^{9/10} \begin{pmatrix} 0 & \sqrt{2} & 0 \\ \sqrt{2} & 0 & 0 \\ 0 & 0 & 0 \end{pmatrix} = \dot{\gamma}^{9/10} \boldsymbol{P}_s^{9/10,eff}. \tag{6.5}$$

The effective slip system 5/8 is mirrored to the effective slip system 2/12 causing plastic shear solely in the midsection under an angle of 35.3° to the horizontal surface (figure 20c). By the combination of slip system 9 and 10, the components D_{13}, D_{23}, D_{31} and D_{32} cancel each other out. The resulting effective slip system 9/10 leads to pure shear in the midsection. Here, the components D_{11} and D_{22} of the rate of stretching tensor are zero.

The contour plots of plastic shear in figure 19 show that the maximum value of plastic shear occurring on slip systems 2 and 5 and on 12 and 8 is with an amount of about 0.8 higher than on corresponding slip systems 9 and 10 with a maximum values of about 0.55. Plastic shear on the effective slip system 9/10 occurs in two regions left and right of the indent expanding vertically to about -4.0 µm. The regions exhibit an asymmetry with respect to the indenter axis with negative plastic shear on the left and positive plastic shear on the right. Right underneath the indent, in an area limited by the two lines $\overline{AB}$ and $\overline{AC}$, including an angle of approximately 90°, no plastic shear occurs on slip system 9/10. Its highest amount appears left and right of the indent about 2.5 µm under the indented surface. As shown above, the effective slip system 9/10 causes solely vertical strain ε_{12} in these areas. The mirrored contour plots of effective slip systems 2/12 and 5/8 in figure 19 show that in both, plastic shear occurs

mainly in a region under the indent expanding vertically to about -5 µm. On effective slip system 2/12, the maximum plastic shear occurs underneath the right flank of the indent close to the tip and corresponding on the left of the indent close to the tip on the mirrored effective slip system 5/8.

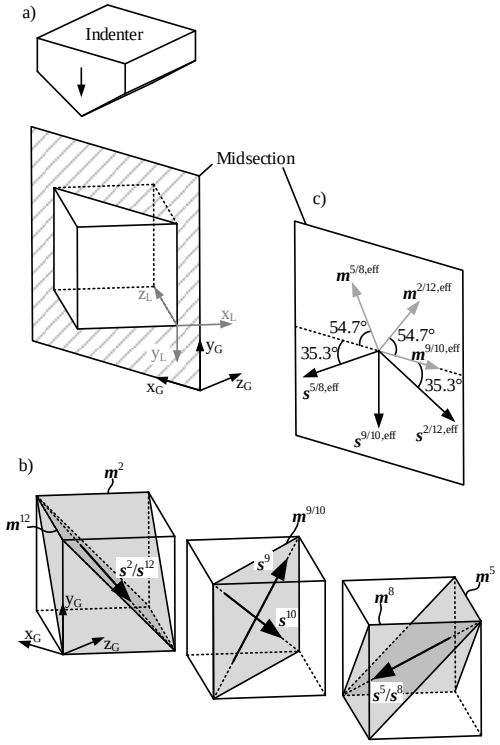

Figure 20: a) crystal orientation (x_L, y_L, z_L) with respect to the midsection of the brick-shaped model (x_G, y_G, z_G) and the indenter; b) corresponding slip systems; c) effective slip systems in the midsection

Regions where slip systems are active under the indent were investigated and combined resulting in a so-called slip system activity map. The determination of the slip system activity map in this work follows Dahlberg et al. (Dahlberg

et al. 2014). Plastic shear at an element node is considered to occur solely on one effective slip system if 90% or more of the total cumulative plastic shear is contributed by this slip system. If the sum of two effective slip systems exceeds 90% of the effective cumulative plastic shear and more than 10% of cumulative plastic shear occurs on each of the two effective slip systems, it is marked that plastic shear occurs on these two slip systems. Consequently, the third effective slip system contributes less than 10% to the cumulative plastic shear in this region and its contribution is negligible. In regions where all effective slip systems contribute more than 10% to the cumulative plastic shear, all slip systems are considered to be active. The regions in which effective slip systems are active following the previously described rules, are superimposed to create the slip system activity map shown in figure 21 for the midsection of the specimen at the indentation depth of 2 µm.

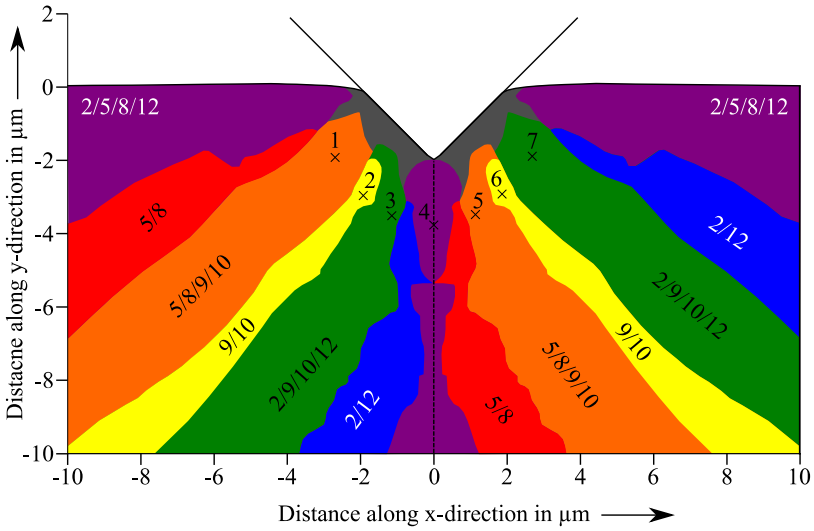

Figure 21: Slip system activity map in the midsection of the brick-shaped model underneath the indenter in the conventional crystal plasticity simulation at the maximum indentation depth of 2 µm

Regions under the indent can be identified following Volz et al. (Volz et al. 2018) where either one or two pairs of corresponding slip systems are active. In the region in contact to the indenter, high plastic deformation occurs and all slip system are active. Figure 21 shows that the particular regions of the activity map in which slip systems are active are symmetric with respect to the indenter axis. However, the slip systems active in these regions are not the same in the mirrored regions in every case. The magenta regions in which both, the effective slip systems 2/12 and 5/8 are active, are symmetric with respect to the indenter axis. So are the green regions in which solely the effective slip system 9/10 is active. The blue and red regions left and right of the indent in which only the effective slip systems 2/12 and 5/8 are active have the same shape but the active slip systems are interchanged. The same is observed for the cyan and yellow regions where the effective slip system 9/10 is active together with the effective slip systems 2/12 and 5/8.
Figure 20 c) shows the slip direction of the effective slip systems in the initial state showing that slip directions of the effective slip systems 2/12 and 5/8 are mirrored with respect to the indenter axis. Since the lattice rotation is antisymmetric with respect to the indenter axis, the slip directions of effective slip systems preserve their symmetry over the whole indentation process. Consequently, dislocation motion left and right of the indent can be seen as mirrored with respect to the indenter axis.

6.1.2 Stress state

The crystal plasticity constitutive law describes the dependency of the plastic shear rates on the stress states. To analyze the stress state underneath the indent calculated in the simulation, it helps to determine the yield surface according to Schmids-law as performed by (Volz et al. 2018) for tungsten following Rice (Rice 1987). Whereas in this rate-independent formulation no plastic yielding occurs within the yield-surface and stress states outside the surface are not possible, the rate-dependent formulation used in the simulations results in yielding for stress states inside the yield surface and stress conditions outside the surface may emerge.

As mentioned above, in the investigated orientation, the shear stresses σ_{13}, σ_{31}, σ_{23} and σ_{32} are zero in the midsection. Therefore, the resolved shear stress τ^{α} simplifies according to equation (2.1) to:

$$\tau^{\alpha} = (\sigma_{11} m_1^{\alpha} s_1^{\alpha} + \sigma_{22} m_2^{\alpha} s_2^{\alpha} + \sigma_{33} s_3^{\alpha} m_3^{\alpha} + \sigma_{12} (s_1^{\alpha} m_2^{\alpha} + m_1^{\alpha} s_2^{\alpha})). \qquad (6.6)$$

Table 9 confirms that for the six active slip systems 2, 5, 8, 9, 10 and 12, the product $s_3 m_3$ is zero. Consequently, the stress components σ_{33} has no influence on plastic shear in the midsection. Another consequence of either s_3 or m_3 being zero in case of the active slip systems is that direction $s_1 m_1$ corresponds to $-s_2 m_2$ as slip plane and slip direction remain orthogonal to each other and the expression can be further simplified to:

$$\tau^{\alpha} = m_1^{\alpha} s_1^{\alpha} (\sigma_{11} - \sigma_{22}) + (s_1^{\alpha} m_2^{\alpha} + m_1^{\alpha} s_2^{\alpha}) \sigma_{12}. \qquad (6.7)$$

Following Schmid's law, plastic shear only occurs when the resolved shear stress τ^{α} on a slip system reaches the critical shear stress of a slip system τ_c. For the case that $\tau^{\alpha} = \pm\tau_c$, the expression (6.7) to determine the yield surface can be rearranged to write σ_{12} as a function of σ_{11} - σ_{22}:

$$\frac{\sigma_{12}}{\tau_c} = \frac{1}{s_1^{\alpha} m_2^{\alpha} + m_1^{\alpha} s_2^{\alpha}} - \frac{2 m_1^{\alpha} s_1^{\alpha}}{s_1^{\alpha} m_2^{\alpha} + m_1^{\alpha} s_2^{\alpha}} \frac{\sigma_{11} - \sigma_{22}}{2\tau_c}. \qquad (6.8)$$

Consequently, for every of the six active slip systems α, a line can be determined in a two-dimensional stress space with $(\sigma_{11} - \sigma_{22})/(2\tau_c)$ on the abscissa and σ_{12}/τ_c on the ordinate as proposed by Rice (Rice 1987) for yielding under plane strain conditions. The resulting inner envelope defines a hexagonal yield surface shown in figure 22.

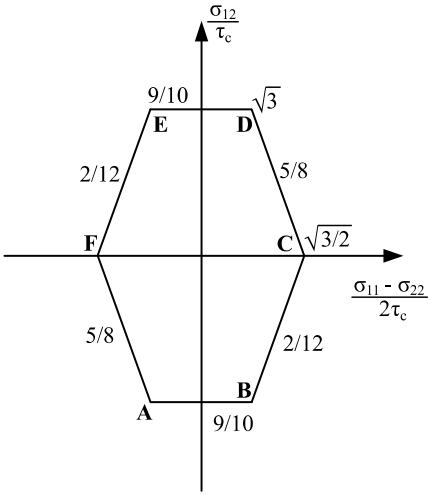

Figure 22: Yield surface based on Schmid´s law under plane strain condition in the midsection of the brick-shaped model

Via the yield surface, the stresses $(\sigma_{11}-\sigma_{22})/2$ and σ_{12} are related to the active slip systems. In case σ_{12} is zero, e.g. at the free surface of the specimen, $(\sigma_{11}-\sigma_{22})/2$ has to reach a value of $\pm\sqrt{3/2}\tau_c$ to cause yielding. The corresponding point in the yield surface is either vertex C or F, dependent on the sign of $(\sigma_{11}-\sigma_{22})/2$. Then, the effective slip systems 2/12 and 5/8 are activated, whose lines intersect at vertex C or F respectively. In case $(\sigma_{11}-\sigma_{22})/2$ is zero or up to $\pm 3/\sqrt{24}\tau_c$, σ_{12} has to reach $\pm\sqrt{3}\tau_c$ to cause slip on a slip system. In that case solely the effective slip system 9/10 is activated. If σ_{12} stays constant at $\pm\sqrt{3}\tau_c$ on one of the horizontal lines $\overline{AB}$ or $\overline{ED}$ and $(\sigma_{11}-\sigma_{22})/2$ is larger than $\pm\sqrt{3/2}\tau_c$, the corresponding point on the yield surface is at one of the vertexes A, B, E or D. So, either slip systems 9/10 and 5/8 (at vertex A and D) of 9/10 and 2/12 (at vertex B and E) are active.

The simulation gives the stress state under the indenter at the indentation depth of 2 µm calculated with the rate dependent formulation of crystal plasticity. The stresses can be related to the activity of effective slip systems with the help

of the yield surface. Figure 23 shows the contour plots of $(\sigma_{11}\text{-}\sigma_{22})/2$ and σ_{12}. Due to the rate-dependent formulation, it is likely that stress states outside the yield surface occur. The plots show an asymmetry and symmetry with respect to the indenter axis for σ_{12} and $(\sigma_{11}\text{-}\sigma_{22})/2$, respectively. The contour plots of the stresses, suggest a division into fan-shaped areas in which either both, σ_{12} and $(\sigma_{11}\text{-}\sigma_{22})/2$ are close to zero or one of them is positive or negative while the other is zero. The regions are limited by the six lines (denoted 1 to 6) in the contour plots (figure 23) for a comparison to the stress states determined in the MBSGCP and non-Schmid simulation performed in the following chapters.

Along the symmetry axis (indenter axis) and as mentioned before, at the free surface of the specimen, the shear stress component σ_{12} has to be zero which is confirmed in the simulation. Left and right of the indent along the surface of the specimen, the absolute value of $(\sigma_{11}\text{-}\sigma_{22})/2$ is approximately 500 MPa, decreasing further away from the indent. The maximum current strength τ_c is about 340 MPa along the surface. Thus, $(\sigma_{11}\text{-}\sigma_{22})/2$ exceeds $\sqrt{3/2}\tau_c$ at the free surface left and right of the indent causing plastic shear here. At the indenter axis, the current strength reaches the saturation value of 530 MPa (see chapter 5.5) leading to $\sqrt{3/2}\tau_c \approx 650$ MPa. The value of $(\sigma_{11}\text{-}\sigma_{22})/2$ along the axis is about 900 MPa, causing plastic shear in this region. Left and right of where the indenter is in contact, under an angle of about 35° to the surface, the shear stress is below 100 MPa and the maximum current strength in this area is about 400 MPa thus $(\sigma_{11}\text{-}\sigma_{22})/2$ has to exceed approximately 490 MPa (compare vertex C or F of the yield surface) to ensure yielding. Up to a distance of 5 µm left and right of the indenter tip, $(\sigma_{11}\text{-}\sigma_{22})/2$ exceeds this value. In the rate-dependent crystal plasticity formulation, two effective slip systems may be active not only at exact one stress state. Figure 23 also shows regions with small absolute values of $(\sigma_{11}\text{-}\sigma_{22})/2$, There the shear stress reaches a maximum value of well over 1000 MPa exceeding the value of $\sqrt{3}\tau_c \approx 920$MPa for the current strength of 530 MPa reached in this regions.

Additionally, the stress states and corresponding active slip systems are analyzed at the seven points marked in the plots shown in figure 23. At point 1, the values of $(\sigma_{11}\text{-}\sigma_{22})/2$ and σ_{12} are negative. This corresponds to vertex A on

the yield surface. Consequently, slip system 5, 8, 9 and 10 should be active which is confirmed by the slip system activity map in figure 21.

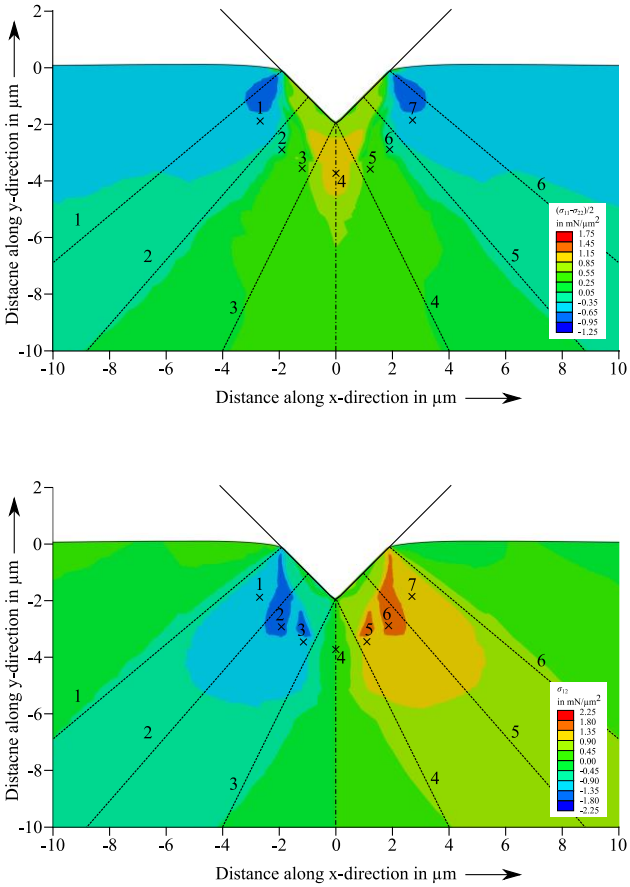

Figure 23: Distribution of $(\sigma_{11}-\sigma_{22})/2$ and σ_{12} in the midsection of the brick-shaped model under the indent at the maximum indentation depth of 2 µm

At point 2, the value of $(\sigma_{11}-\sigma_{22})/2$ is close to zero and σ_{12} is still negative, corresponding to the point between vertexes A and B meaning that solely the effective slip system 9/19 is active in this region which is again confirmed by the slip system activity map. At the third highlighted point, $(\sigma_{11}-\sigma_{22})/2$ is positive and σ_{12} still negative, corresponding to vertex B and as confirmed by the slip system activity map, effective slip system 9/10 and 2/12 are active. At the fourth point on the vertical line under the indent, $(\sigma_{11}-\sigma_{22})/2$ is positive and σ_{12} zero, consequently effective slip systems 5/8 and 2/12 are active at this point. Due to the symmetry of the contour plot of $(\sigma_{11}-\sigma_{22})/2$, the same values at the points 5, 6 and 7 occur than at points 1, 2 and 3. The values of σ_{12} are the same at these points but differ by sign. Thus, point 5 corresponds to vertex D on the yield surface and effective slip systems 5/8 and 9/10 are active. The stress state at point 6 leads to a corresponding point on the yield surface between vertex D and E so that only the effective slip system 9/10 is active at this point. At the last highlighted point, $(\sigma_{11}-\sigma_{22})/2$ is negative and σ_{12} positive. Thus, the stress state changes to vertex E and systems 2/12 and 9/10 are active. Just like on the left of the indent, the investigations based on the yield surface and the stress states are confirmed by the slip system activity map determined in the simulation.

6.1.3 Increments of plastic shear

So far the analysis focused on the cumulative plastic shear at the indentation depth of 2 µm. In the present chapter, the shear rate and its evolution during indentation were investigated following the work of Reuber et al. (Reuber et al. 2014) and Dahlberg et al. (Dahlberg et al. 2014). Figure 24 shows the plastic shear rate $\dot{\gamma}^{\alpha}$ calculated via the increment of the plastic shear divided by the time increment $\Delta\gamma/\Delta t$ of the six active slip systems at the three indentation depths 1 µm, 1.5 µm and 2 µm. Again, solely the results of the three slip systems 2, 5 and 9 are shown representing the corresponding slip systems 12, 8 and 10, respectively. The two plots of plastic shear increments on systems 2/12 and 5/8 are mirrored but asymmetric. For slip systems 9/10 however, the plots are antisymmetric with respect to the indenter axis.

On slip system 2/12, a band of plastic shear occurs on the left side of the indenter. This band emanates from the point where contact between indenter and specimen starts (called contact point in the following) and points down towards the indenter axis.

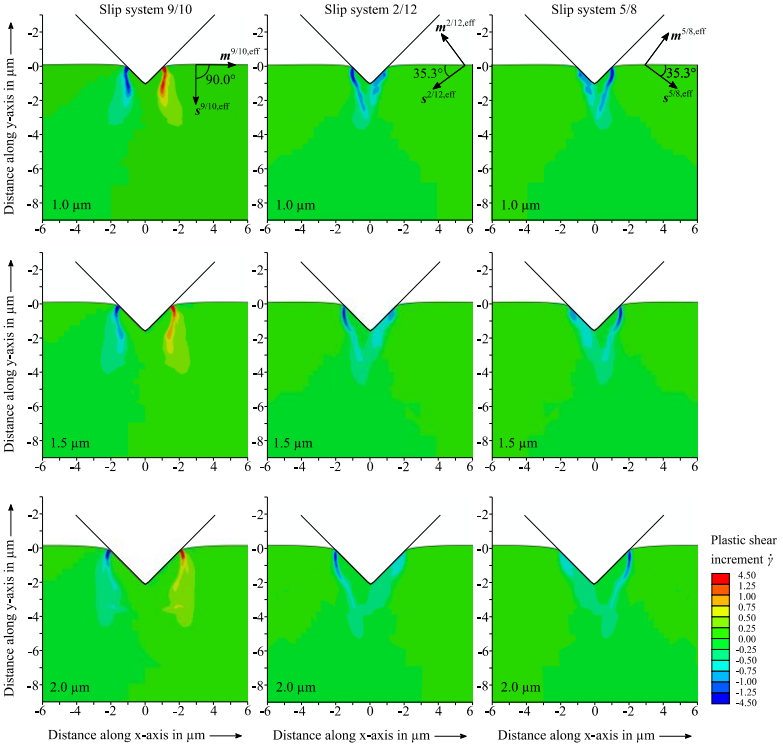

Figure 24: Increments of plastic shear $\dot{\gamma}$ at the three indentation depths 1 µm, 1.5 µm and 2 µm in the conventional single-layer crystal plasticity simulation

With an increase of the indentation depth, the overall shape of the band stays similar but the plastic shear rate within the band decreases. Besides, plastic shear appears under the right indenter flank during the indentation process.

With increasing indentation depth, plastic shear in this region decreases as well. The figure shows that plastic shear evolves alike on slip systems 5/8 but mirrored with respect to the indenter axis like the resolved shear stress. On slip systems 9/10, two symmetric bands of plastic shear occur but with different sign, both starting at the contact points on the left and right of the indent, emanating down with a convex shape. The three plots of different indentation depth show similar shaped of the bands. Like slip systems 2/12 and 5/8, the plastic shear rate within the bands decreases at higher indentation depths. A comparison of the three different indentation depth for all active slip systems shows that the overall shape of regions of the plastic shear rate is similar. The bands in which plastic shear occurs propagate through the crystal starting invariably at the contact point of the of the indenter. These propagating bands can be explained following Kords (Kords 2013) by a deformation induced significant increase of dislocations with increasing indentation depth under the indent leaving a region where the material experienced high strengthening becoming less favorable to plastic deformation. The occurring bands are the hull of this region propagating through the crystal with increasing indentation depth, always starting at the contact point.

In order to gain deeper insight in the plastic deformation fields under the contact points, further investigations regarding plastic shear and rotation increments were performed for the tungsten bcc single crystal. As reported by Hill et al. (Hill et al. 1947), Johnson (Johnson 1985) and Saito (Saito and Kysar 2011; Saito et al. 2012) angular sectors that characterize the plastic zone under the indent can be determined in wedge nanoindentation between the indenter flank and the original surface.

To investigate if sectors can be determined in the numerical investigations in this work, too, a plastic shear increment map shown in figure 25 was determined at the indentation depth of 2 µm. If more than 90% of plastic shear occurred on one effective slip system, solely this system was assumed to be active in the current increment. Two effective slip systems were assumed to be active if 90% or more of plastic shear occurred on these two slip systems just like in the determination of the slip system activity map. The map shows different

regions in which plastic shear occurs in the last increment of the simulation emanating from the contact point in a fan shape. Three regions can be determined where solely plastic shear on effective slip system 5/8, 9/10 and 2/12 occurs (red, yellow and blue). However, the region where solely slip system 5/8 is active is very narrow. Between the regions where solely plastic shear occurs on one effective slip system, plastic shear on two effective slip systems occur (magenta, orange and green).

Along the circular path highlighted in figure 25 with a radius of 4 µm, the plastic shear increments are investigated in detail. Figure 26 a) shows the plastic shear increments of the three effective slip systems 5/8, 9/10 and 2/12 along the circular path. Starting at the indenter axis, in section I, slip systems 5/8 and 2/12 are active, marked as section I. In about 1 µm distance, in section II, solely plastic shear on slip system 5/8 occurs. In the following region III, slip systems 5/8 decrease while 9/10 increases, so both are active simultaneously. In the following region IV, plastic shear occurs mainly on slip system 9/10. In region V, slip systems 2/12 and 9/10 are active. This is confirmed by the plastic shear increment map.

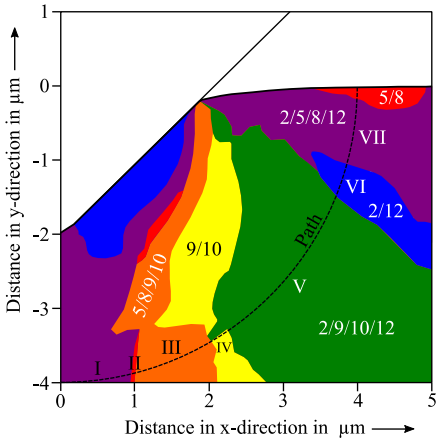

Figure 25: Plastic shear increment map of the right side of the indent in the midsection of the conventional brick-shaped model at the indentation depth of 2 µm

In the second last region VI along the path, slip occurs mainly on slip system 2/12 while in the last section VII, close under the surface, plastic shear increments are rather small. Beside the plastic shear rates, figure 26 b) shows the lattice rotation increment (increment of the first Euler angle) divided by the time increment along the path. It turns out that in the regions II, IV and VI, where plastic shear occurs mainly on one effective slip system, the absolute value of lattice rotation rate is maximal with changing sign. In the regions where two slip systems are active, the absolute value of in-plane rotation rate decreases significantly. This is due to fact that one of the active slip systems leads to positive rotation and the other one to negative. This corresponds well to the investigations of Saito et al. (Saito and Kysar 2011; Saito et al. 2012).

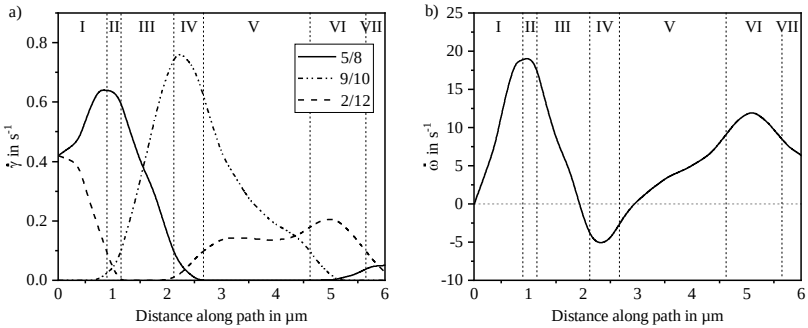

Figure 26: a) $\dot{\gamma}$ on the three effective slip systems; b) $\dot{\omega}$ along the circular path at the indentation depth of 2 µm

6.1.4 Crystal lattice rotation and GND density

The undeformed crystal lattice is characterized by the three Euler angles φ_1, θ and φ_2 following Bunge. For the chosen crystal orientation with its plane strain conditions in the midsection, the two Euler angles θ and φ_2 are constant during the indentation process. Solely the first Euler angle φ_1 changes and characterizes the in-plane lattice rotation. The value of the first Euler angle calculated in the user material subroutine for each integration point were read from the

ABAQUS data file and interpolated on uniformly distributed points using the SciPy griddata interpolation method (The SciPy community 2019). Then the interpolated data were visualized in Matlab (MathWorks). The visualization of the in-plane rotation as contour plot directly with the post processing tool of ABAQUS is also possible. For a visualization corresponding to the experiments and a comparison of experimental and numerical results, the interpolated Euler angles are used as input for the software package MTEX (Hielscher et al.) that was modified by J. Wang in the course of her dissertation to use the kernel average misorientation method (KAM) to determine the GND density. Figure 27 shows the in-plane crystal lattice rotation under the indent in the midsection at the indentation depth of 2 µm. A vertical line running down from the indenter tip divides the rotation map in figure 27 into two antisymmetric regions. Significant lattice rotation occurs close to the flanks and under the indenter. The maximum values of lattice rotation in this region ranges from approximately -20° to 20°. Outside this region, the lattice rotation maps exhibit a fan-shape with alternating regions of positive and negative rotation and significantly less rotation than in the region close to the indenter.

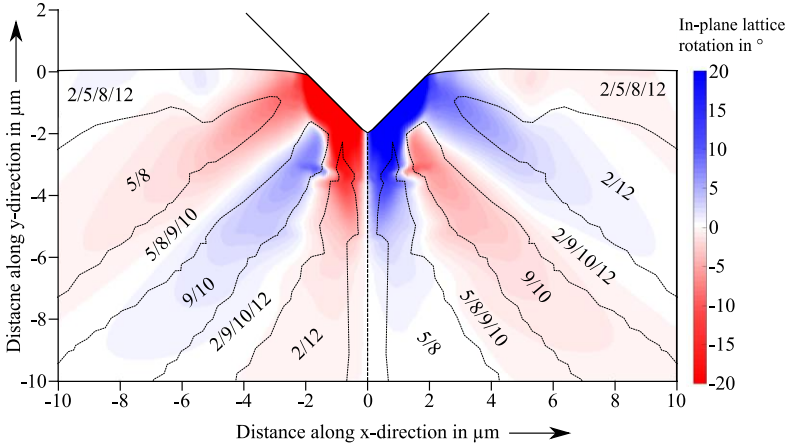

Figure 27: First Euler angle φ_1 in the midsection of the model, representing the in-plane lattice rotation

Beside the in-plane rotation, the regions where effective slip systems are active are plotted in figure 27. A correlation between these regions and the rotation map is visible. In regions where two effective slip systems are active, a sign change of the rotation patterns occurs and rotation is either positive or negative in regions where solely two corresponding slip systems are active. This corresponds to the former investigations of the increments of plastic shear showing that in regions where solely one effective slip system is active, the lattice rotation increment reaches a peak and decrease to low values in regions where two of the effective slip systems are active.

Based on the crystal lattice rotation calculated in the brick-shaped conventional crystal plasticity simulation, the density of geometrically necessary dislocations in the midsection at the indentation depth of 2 µm determined via the kernel average misorientation method in MTEX (Hielscher et al.). The result is shown in the following figure 28.

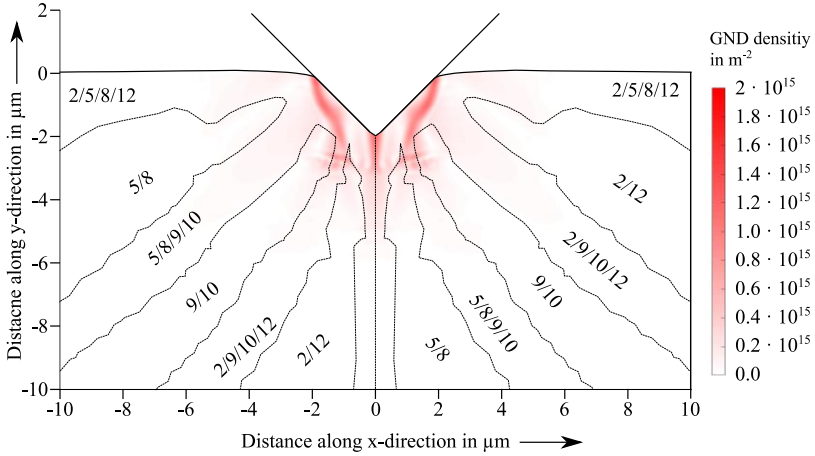

Figure 28: Density of geometrically necessary dislocations in the midsection of the brick-shaped conventional crystal plasticity simulation at the indentation depth of 2 µm, determined with the kernel average misorientation method

The plot of shows three bands of high GND density, two emanating from the contact points downwards and the one starting under the indenter tip along the indenter axis. A comparison with the in-plane lattice rotation shows that the bands with high GND-densities occur at the sharp boundaries of the regions under the indenter flanks where high lattice rotation occurs and along the indenter axis where a sudden sign change occurs. Further away from the indent, fan-shaped regions with higher GND-densities occur, corresponding to the regions in which two effective slip systems are active. Regions where two effective slip systems are active can be seen as transit regions, in which one of the effective slip system increases and the other one decreases causing a higher GND density.

6.2 Results of the [123] oriented brick-shaped conventional CP simulation

Beside the $[0\bar{1}0]$ orientation of the single crystal, the lattice rotation in the midsection, material pile-up at the indented surface and the load-displacement curve were investigated for the [123] orientation. Beside the crystal orientation, all other input parameters and boundary conditions were the same in both, the [123] and $[0\bar{1}0]$ brick-shaped conventional crystal plasticity simulation. The aim of the study is the investigation of the influence of the single crystal's orientation on the plastic deformation behavior in the wedge indentation simulations. All investigations were again performed in the midsection of the brick-shaped specimen.

6.2.1 Slip system activity and lattice rotation

Plastic shear on six slip systems were identified to be rather small in the midsection of the [123] oriented brick-shaped simulation. However, in opposite to the $[0\bar{1}0]$ simulation, none of the Schmid-tensors of the twelve slip systems correspond in any way to each other and the distributions of plastic shear for all active slip systems in the midsection exhibit different shapes. Further, the

investigation of the stress state in the midsection showed that no stress components are zero, which was beside the corresponding Schmid-tensors the second condition for plane strain conditions in the $[0\bar{1}0]$ simulation. So it is confirmed by the simulation, that general strain conditions are present in the midsection. With that, no in-plane lattice rotation occurs and the first Euler angle φ_1 is not sufficient to describe the lattice rotation. The distributions of the three Euler angles are shown in the following figure 29 at the indentation depth of 2 µm in the specimen's midsection. All three Euler angles exhibit a fan shape with areas in which the sign of the Euler angles changes from positive to negative comparable to the result of the $[0\bar{1}0]$ simulation. However, in opposite to the first Euler angle, describing the lattice rotation in the $[0\bar{1}0]$ simulation, no symmetry occurs for any of the three Euler angles. With maximum values of approx. –35° to +40° right under the indenter flanks, the first Euler angle determined in the [123] simulation is much higher than the second and third Euler angles. These are both between -5° and +5°. However, in comparison to the $[0\bar{1}0]$ simulation, they are not zero.

A further investigation of the material pile-up of the surface of the specimen in the [123] simulation and a comparison to the $[0\bar{1}0]$ results was performed. Figure 30 shows in a) and b) the piled-up material at the indented surface in the [123] and $[0\bar{1}0]$ simulation, respectively. Only in the $[0\bar{1}0]$ simulation, a symmetry of the piled up material with respect to the indenter tip occurs. In the [123] simulation, the amount of piled-up material is significantly higher at the right of the residual imprint. Further, a symmetry with respect to the midsection highlighted in a) and b) occurs in the $[0\bar{1}0]$ simulation but not in the [123] simulation. Here, slightly more material piles up below the midsection. In the same figure in c) and d), the vertical displacement is shown in the midsection. Again, the distribution is symmetric with respect to the indenter axis in the $[0\bar{1}0]$ simulation but not in the [123] simulation. Here vertical displacement is more prominent on the right side.

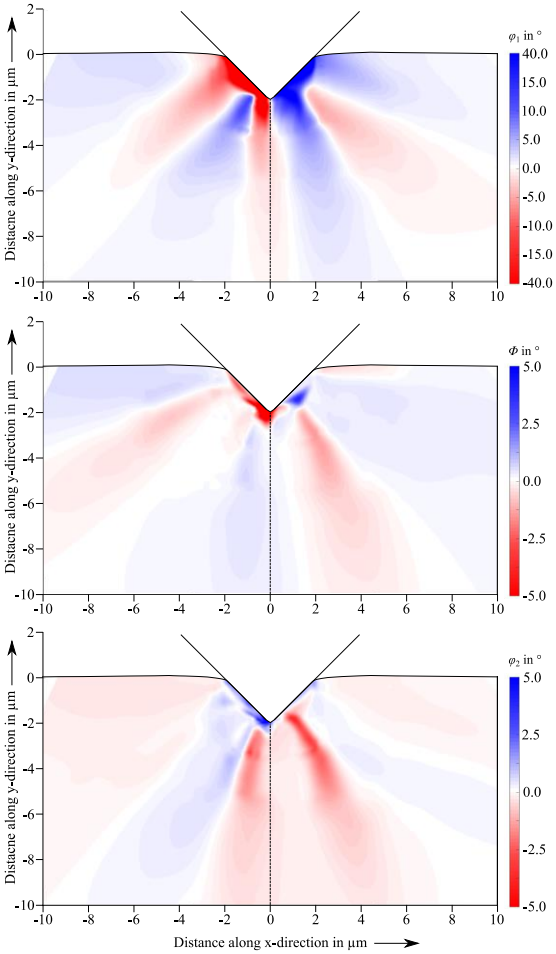

Figure 29: Three Euler angles in the midsection of the [123] brick-shaped conventional crystal plasticity simulation at the indentation depth of 2 µm

Stated by Wang at al. (Wang et al. 2004), the elevated material at the indented surface (pile-up) can be understood by the translation of material along the intersection of the primary slip systems and the indented surface. It was shown

above (figure 20) that for the $[0\bar{1}0]$ oriented single crystal three effective slip systems can be determined in the midsection. These have the effective slip plane normals $(1\sqrt{2}0)$, $(\bar{1}\sqrt{2}0)$ and $(\bar{1}00)$.

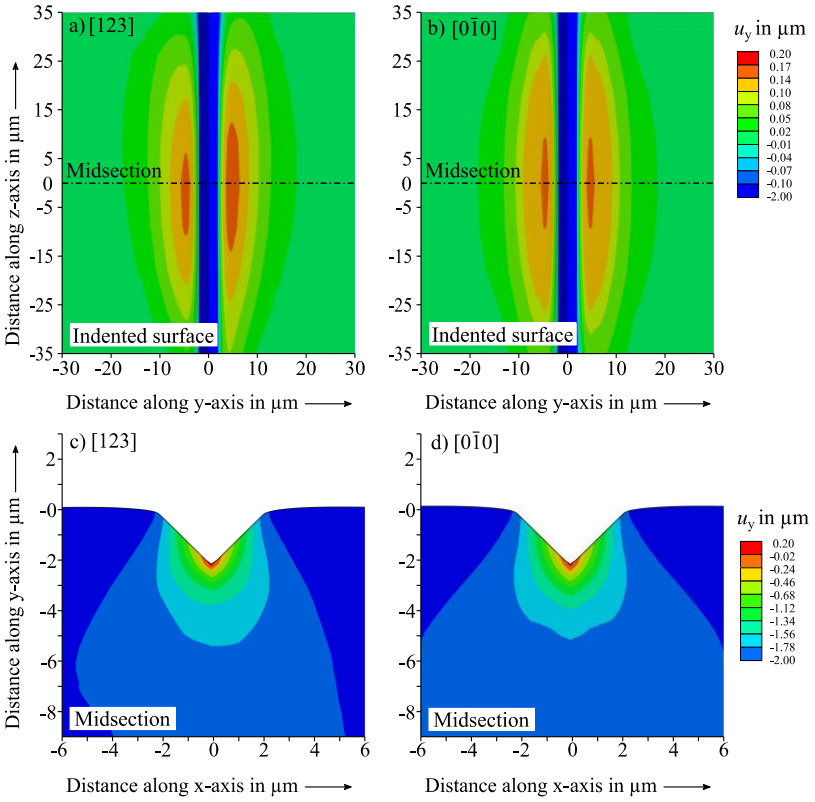

Figure 30: Material pile-up (u_y) at the surface of the specimen in the [123] simulation in a) and the $[0\bar{1}0]$ simulation in b), respectively; u_y in the midsection of the [123] simulation in c) and the $[0\bar{1}0]$ simulation in d), respectively

All effective slip plane normals intersect the indented (010) surface in an [001] direction (see figure 30 b)) in the midsection. The effective slip systems 2/12

and 5/8 have mirrored plastic shear, slip directions and slip planes, so a symmetry of the piled up material in the midsection occurs. For the [123] oriented single crystal, neither a symmetry of slip directions or slip planes nor corresponding plastic shear occurs. Thus, an unsymmetric pile-up pattern at the indented surface for the [123] simulation in the midsection must occur (see figure 30 a)).

The determination and comparison of the load-displacement curves for both, the [123] and [$0\bar{1}0$] crystal orientation shows that a significantly lower load on the indenter is necessary for the same penetration depth of 2 µm in the [123] simulation. The maximum load on the indenter at 2 µm indentation depth is with 1400 mN in the [$0\bar{1}0$] simulation, approx. 100 mN higher than in the [123] simulation. This indicates that in the [123] orientation, the orientation of the slip systems enables the crystal to deform easier under the penetrating indenter in comparison to the [$0\bar{1}0$] orientation. So, the orientation of the crystal has a significant influence of the plastic deformation response in the wedge indentation simulation.

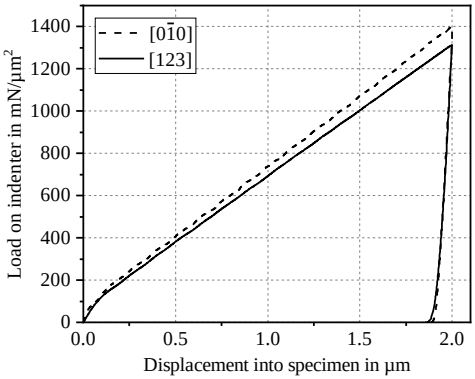

Figure 31: Load-displacement curves determined in the conventional [123] and [$0\bar{1}0$] simulation

6.3 Results of the [0$\bar{1}$0] oriented single-layer MBSGCP simulation

The aim of the mechanism-based strain gradient crystal plasticity simulations is a study of the influence of gradients of plastic shear and the associated additional hardening due to GNDs on the plastic deformation behavior of the single crystal on the microscale. Therefore, the single-layer model was used together with the MBSGCP subroutine for the FE-simulation of wedge nanoindentation into the single crystal in the [0$\bar{1}$0] orientation. The activity of slip systems, deformed geometry, stress state, resolved and critical shear stress on slip systems and the crystal lattice rotation and GND density was determined and compared to the results of the conventional CP simulation in the midsection of the brick-shaped model for an evaluation of the influence of gradients of plastic shear. Additionally, a study of the indentation size effect was performed based on the MBSGCP simulation.

6.3.1 Influence of GNDs on strain conditions

As shown in chapter 6.1.1, plane strain conditions occur in the midsection of the brick-shaped model for the [0$\bar{1}$0] oriented single crystal using the conventional CP subroutine and only six slip systems which can be reduced to three effective slip systems are active under the indent. Since gradients of plastic shear, i.e. geometrically necessary dislocations solely increase the current strength of a slip system, it is most likely that, like in the conventional CP simulation, solely slip systems 2, 5, 8, 9 and 10 are active in the MBSGCP simulation (the numbering in both, the MBSGCP and conventional CP subroutine corresponds). Furthermore, plane strain conditions in the single-layer model using the MBSGCP subroutine solely occur if the stress components σ_{13} and σ_{23} are zero, which they are, and the densities of geometrically necessary dislocations on corresponding slip systems following the equation:

$$n_{\mathrm{G}}^{\alpha} = |m^{\alpha} \times [s^{\alpha,2}\nabla\gamma^{2} \times m^{2} + s^{\alpha,12}\nabla\gamma^{12} \times m^{12} + s^{\alpha,5}\nabla\gamma^{5} \times m^{5} + s^{\alpha,8}\nabla\gamma^{8} \times m^{8} + s^{\alpha,9}\nabla\gamma^{9} \times m^{9} + s^{\alpha,10}\nabla\gamma^{10} \times m^{10}]| \quad (6.9)$$

are equal. Corresponding plastic shear $\gamma^2 = \gamma^{12}$, $\gamma^5 = -\gamma^8$ and $\gamma^9 = -\gamma^{10}$ were identified at the first increments of the simulation, so the gradients of strains correspond as well in the same manner: $\nabla\gamma^2 = \nabla\gamma^{12}$, $\nabla\gamma^5 = -\nabla\gamma^8$ and $\nabla\gamma^9 = -\nabla\gamma^{10}$. Furthermore, the following connections were found for the inner product $s^{\alpha\beta}$: $s^{\alpha,2} = s^{\alpha,12}$, $s^{\alpha,5} = s^{\alpha,8}$, $s^{2,9} = -s^{2,10}$, $s^{5,9} = -s^{5,10}$, $s^{8,9} = -s^{8,10}$, $s^{12,9} = -s^{12,10}$ but $s^{9,9} = s^{10,10}$ and $s^{10,9} = s^{9,10}$. In case of slip systems 9 and 10, the slip plane normal $\boldsymbol{m}^9$ and $\boldsymbol{m}^{10}$ are the same. For slip system 2 and 12 as well as 5 and 8, the normal to slip planes differs. With these findings, together with the equation for the calculation of the densities of geometrically necessary dislocations on slip systems, it was found that in the $[0\bar{1}0]$ orientation, $n_{\mathrm{G}}^{2} = n_{\mathrm{G}}^{12}$, $n_{\mathrm{G}}^{5} = n_{\mathrm{G}}^{8}$ and $n_{\mathrm{G}}^{9} = n_{\mathrm{G}}^{10}$ and thus, strain gradients and associated geometrically necessary dislocations do not violate the plane strain conditions in the single-layer MBSGCP simulation.

6.3.2 Slip system activity

Simulations performed with the single-layer model using the MBSGCP subroutine confirm that gradients of plastic shear and the associated geometrically necessary dislocation density on slip systems correspond on slip system 2 with slip system 12, 5 with 8 and 9 with 10. The plastic shear on slip systems 2, 5 and 9 are shown in figure 32 (representing slip system 12, 8 and 10, respectively). Like in the conventional crystal plasticity simulation, the distribution of plastic shear on slip system 2 and 5 (and so on 8 and 12) are mirrored with respect to the indenter axis. The distribution of plastic shear of slip system 9 and 10 is antisymmetric with respect to the indenter axis. Comparing the plastic shear on active slip systems of the MBSGCP (figure 32) with the conventional CP simulation results (figure 19) reveals that for all active slip systems, both, the absolute values and the distributions of the plastic shear are similar. On slip

system 2, 5, 8 and 12, slip occurs mainly under the indent limited by vertical lines that emanate from points where contact between indenter and specimen starts (called contact point in the following). In contrast, no slip in a region limited by the two lines $\overline{AB}$ and $\overline{AC}$ right under the indent occurs on slip systems 9 and 10.

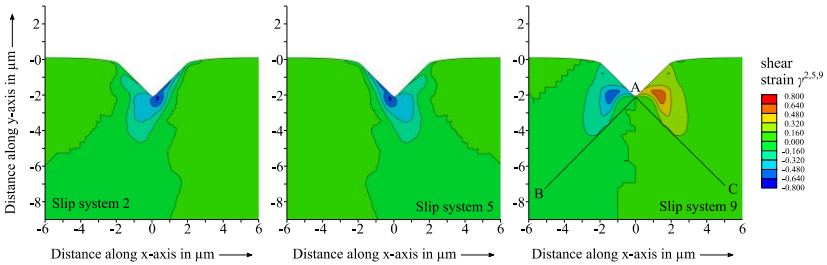

Figure 32: Plastic shear on slip system 2, 5 and 9 under the indent at the indentation depth of 2 µm

Figure 33 shows the slip system activity map under the residual imprint after unloading. The activity map for the MBSGCP simulation was determined in the same manner as for the conventional CP simulation. The slip system activity maps determined in the conventional and mechanism-based strain gradient crystal plasticity simulation shown in figure 21 and figure 33, respectively, exhibit a high similarity like the individual slip systems. In both, at the flanks of the indenter, all six slip systems are active. The shape and size of this region (grey) is similar. Like in the conventional simulation, fan-shaped regions where either one or two effective slip systems are active occur and regions with one or two effective slip systems alternate. The angles of the individual regions with respect to the surface of the specimen are similar in the conventional and mechanism-based strain gradient crystal plasticity simulation. Right under the indent, slip systems 2, 5, 8 and 12 are active. However, this region ends at about 6 µm under the original surface in the MBSGCP while it expands to the bottom of the shown figure in the conventional CP simulation.

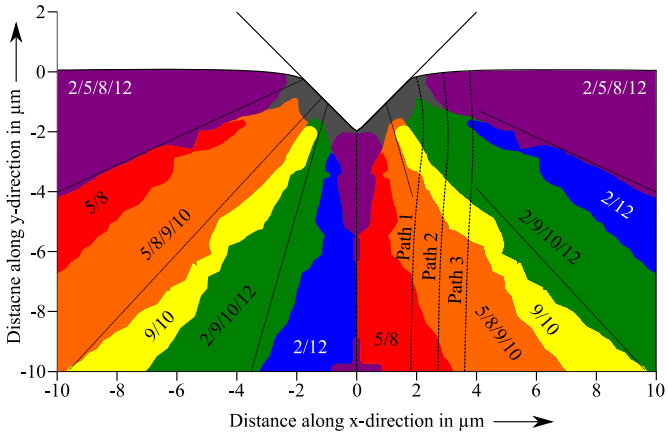

Figure 33: Slip system activity map underneath the indenter in the mechanism-based strain gradient crystal plasticity simulation

Figure 34 a) shows the indentation profile of the surface determined in the conventional and mechanism-based strain gradient crystal plasticity simulation after unloading. Due to symmetry it is sufficient to show only the right half. The indentation profiles differ slightly with a higher pile-up in the CP simulation. To figure out the reason, the computed plastic shear on active slip systems was analyzed in detail along three paths to the right of the residual imprint. Their location is marked in figure 33 and figure 34 a). Figure 34 b), c) and d) show the total cumulative plastic shear as well as plastic shear on slip system 9 and 10 along these three paths 1, 2 and 3, respectively. The total cumulative plastic shear along the paths is a measure for the overall plastic deformation. Slip on slip system 9 and 10 together is responsible for material transport in vertical (i.e. indentation) direction and is seen to be decisive for the occurrence of material piling-up or sinking-in. The slip system activity map in figure 33 shows that along path 1, initially all slip systems are active till about 1 µm under the surface before slip systems 9 and 10 become dominating. This is also

visible in figure 34 b). At about 3 µm under the surface, almost the whole cumulative plastic shear is made up of plastic shear on slip system 9 and 10. The figure also shows that in the MBSGCP simulation, the cumulative plastic shear and plastic shear on slip system 9 and 10 are always higher up to 3 µm than in the conventional CP simulation. In a higher depth they are the same. Along path 2, till about 1 µm under the surface, mainly slip systems 2, 5, 8, and 12 are active (purple region in the slip system activity map). In this area, the cumulative plastic shear is higher in the conventional CP simulation.

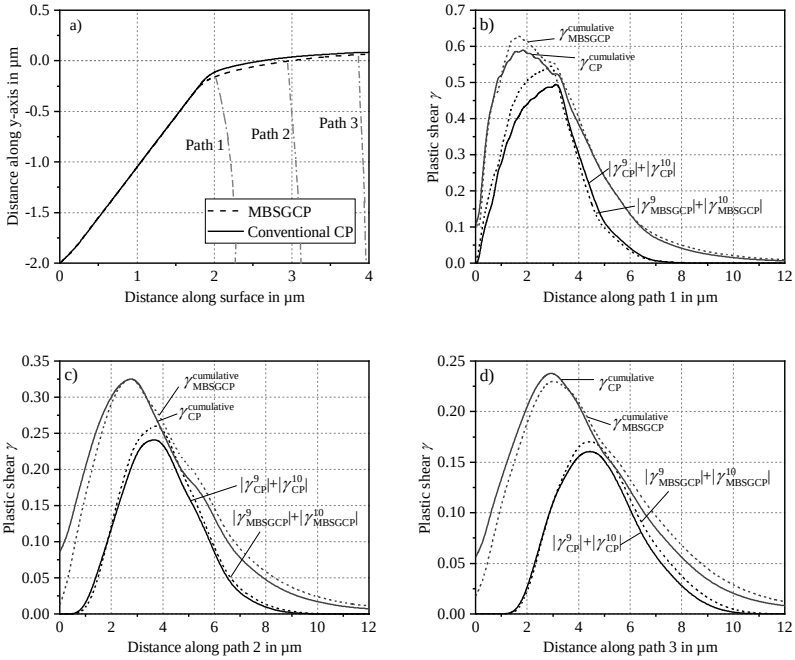

Figure 34: a) conventional and MBSGCP indentation profiles; b) plastic shear on slip systems 9 and 10 together with the cumulative plastic shear along path 1, 2 and 3 in b), c) and d)

However, between 3 µm and 6 µm along the path 2 under the indent (yellow area in the slip system activity map), plastic shear mainly occurs on slip system

9 and 10 again and is higher in the MBSGCP simulation. On the third path, again mainly slip on slip systems 2, 5, 8, and 12 occurs directly below the surface and the cumulative plastic shear is higher in the conventional CP simulation like along path 2. Between 4 µm and 6 µm, however, slip occurs again mainly on slip system 9 and 10 again (yellow area) and plastic shear on these slip systems is again higher in the MBSGCP simulation. So along all paths, slip on slip systems 9 and 10 is higher in the MBSGCP simulation explaining the less present pile-up (the higher cumulative plastic shear along path 2 and 3 under the surface, where mainly slip systems 2, 5, 8 and 12 are active is assumed to have an insignificant influence of the pile-up behavior).

6.3.3 Stress state

The plane strain conditions are not violated due to the occurrence of GNDs in the mechanism-based strain gradient crystal plasticity simulations. Consequently, the resolved shear stress τ^{α} on active slip systems in the investigated highly symmetric orientation depends solely on the stress components σ_{11}- σ_{22} and σ_{12}. The distribution of $(\sigma_{11}$-$\sigma_{22})/2$ and σ_{12} are shown in figure 35 a) and b). Like in the stress state of the conventional CP simulation, $(\sigma_{11}$-$\sigma_{22})/2$ exhibits two areas left and right of the indenter between the surface of the specimen and the lines 2 and 5 with a positive value. Right under the indent, a region with a positive value occurs with line 3 and 4 as borders. Between line 2 and 3 as well as 4 and 5, the value of $(\sigma_{11}$-$\sigma_{22})/2$ decreases to zero. While the maximum negative value of $(\sigma_{11}$-$\sigma_{22})/2$ at the contact points and the maximum positive value under the indenter tip are about -1.2 GPa and 1.8 GPa, they are about 0.95 GPa and 1.2 GPa in the conventional CP simulation. Thus, the occurring maximum value of $(\sigma_{11}$-$\sigma_{22})/2$ is much higher in the MBSGCP simulation. However, the distribution of $(\sigma_{11}$-$\sigma_{22})/2$ can be, just like in the conventional CP simulation, divided into fan-shaped regions with either positive or negative values.

The same holds for the distribution of σ_{12} under the indent shown in figure 35. Again, two regions occur left and right of the indent limited by the two lines 1 and 6. Within these regions, the value of σ_{12} is close to zero. In the region

between the lines 1 and 3 as well as 4 and 6, σ_{12} becomes negative and positive, respectively, whereby the absolute value is much higher closer to the indent and decreases further away. However, right at the indenter flanks, σ_{12} decreases to a small value. In the region between line 3 and 4, the value of σ_{12} is again close to zero.

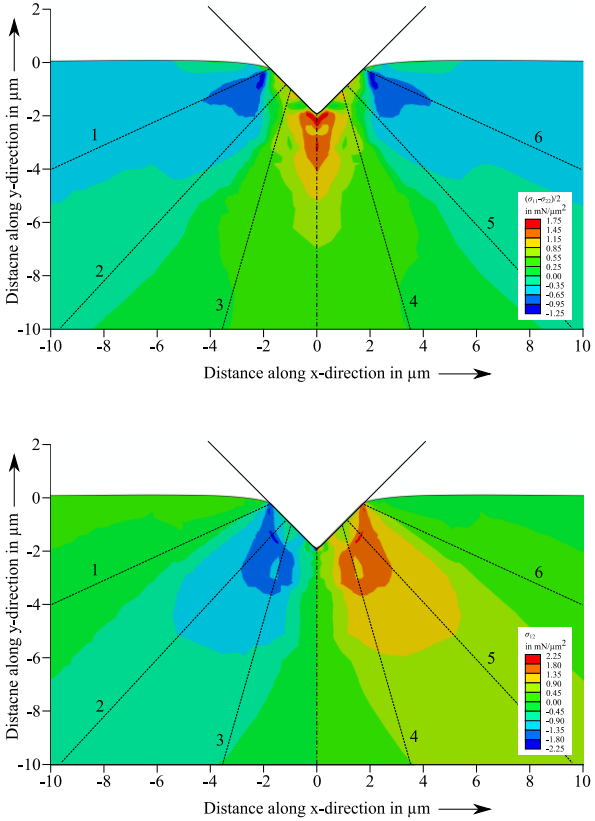

Figure 35: Distribution of (σ_{11}-σ_{22})/2 and σ_{12} in the midsection of the single-layer model under the indent at the maximum indentation depth of 2 µm

So, just like the distribution of $(\sigma_{11}-\sigma_{22})/2$, areas with positive, negative and with small values close to zero can be identified exhibiting a fan-shape starting at the indent. The occurring maximum absolute values of σ_{12} at the contact points left and right of the indenter are with about 2.2 GPa and about 1.6 GPa in the MBSGCP and the conventional crystal plasticity simulation and so again much higher in the MBSGCP simulation.
Concluding, the overall shape of the contour plots of $(\sigma_{11}-\sigma_{22})/2$ and σ_{12} are similar in the conventional and mechanism-based strain gradient crystal plasticity simulation. However, the stress state in the midsection is much higher in the MBSGCP simulation.

The determination of the stress state in the single layer MBSGCP model and its comparison to the stress state calculated in the conventional CP simulation showed significantly higher stresses under the indent in the MBSGCP simulation. This indicates that a much higher resolved shear stress as driving force on the active slip systems is necessary in the MBSGCP simulation to achieve the same enforced plastic shear on the active slip systems. This is confirmed by the distributions of resolved shear stresses on the three slip systems 2, 5 and 9 (representing 12, 8 and 10) of the MBSGCP and conventional CP simulation shown in figure 36. The overall shape of the results is similar for the compared slip systems. However, much higher resolved shear stresses occur in the regions under the indent in the MBSGCP simulation as already indicated by evaluation of stresses. Like the plastic shear, the contour plots of the resolved shear stress on slip system 2 and 5 are mirrored with respect to the indenter axis. The resolved shear stress on slip system 9 is antisymmetric with respect to the indenter axis. The highest value of τ_{res} in the conventional CP simulation is about 0,85 mN/µm^2 but about 1.7 mN/µm^2 in the mechanism-based strain gradient simulation on slip systems 2, 5, 8 and 12. On slip system 9 and 10, the resolved shear stress in the MBSGCP simulation is only slightly larger in small regions right underneath the indenter. Thus, a much higher resistance against slip, mainly on slip system 2, 5, 8 and 12 must be present due to the occurrence of geometrically necessary. The distribution of the resolved shear stress on slip systems 2 and 5 show that further away from the indent, the values of τ_{res} are

similar, but in the region close around the indent, significantly higher shear stresses occur. Areas with high resolved shear stress occur on slip system 2 and 12 at the right flank of the indenter and right under the indenter tip. Left of the indenter a small area with high resolved shear stress starts at the contact point emanating downwards. At the left flank of the indenter however, smaller values of resolved shear stress occur. On slip system 5 and 8, areas with high τ_{res} occur mirrored to those on slip systems 2 and 12. The higher resolved shear stresses in the described areas corresponds to regions with high values of $(\sigma_{11}-\sigma_{22})/2$ and σ_{12} at the contact points and right under the indenter tip.

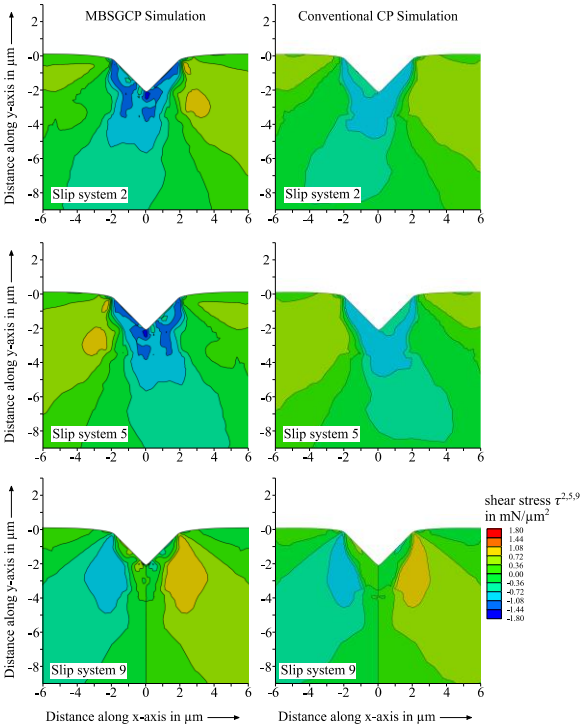

Figure 36: Resolved shear stress τ_{res} on slip system 2, 5 and 9 under the indent at the indentation depth of 2 µm calculated

6.3.4 Critical shear stress

The contribution to strain hardening due to geometrically necessary dislocations is investigated in this chapter in detail. As described in chapter 2.5, the overall critical shear stress g_t is the sum of g_{SSD} and g_{GND} describing the hardening due to statistically stored dislocation and geometrically necessary dislocations, respectively. The much higher resolved shear stress that was found in regions under the indent on slip systems 2, 5, 8 and 12 indicates much higher strengthening in the MBSGCP simulation. This is confirmed by the results of the distributions of g_{GND} plotted in figure 37 a) to c) for the six active slip systems. As shown in chapter 6.3.1, the effective density of geometrically necessary dislocations and with that the contribution to the overall strengthening g_{GND}, is the same on corresponding slip systems, so $g^2_{GND} = g^{12}_{GND}$, $g^5_{GND} = g^8_{GND}$ and $g^9_{GND} = g^{10}_{GND}$. Again, solely the results for slip system 2, 5 and 9 are shown in the figure 37 as they also represent the slip systems 12, 8 and 10. Figure 37 d) shows the distribution of the resolved shear stress g_{SSD}, which is the same for every active slip system. The results of g_{GND} determined in the MBSGCP simulation have mirrored contour plots with respect to the indenter axis for slip system 2 and 12 as well as 5 and 8, like the plastic shear and resolved shear stress shown above. The distribution of g_{GND} on slip systems 9 and 10 is mirrored with respect to the indenter axis. The saturation value of g_{SSD} is an input material parameter which is set to 0.53 GPa. This maximum value is reached in a spherical-shaped region under the indent as shown in figure 37 d). Outside this area, the value decreases steadily. In contrast, the distribution of g_{GND} determined in the mechanism-based strain gradient crystal plasticity simulation exhibits small areas in which high values of g_{GND} occur defined by the gradients of plastic shear. The highest value of g_{GND} is about 1.04 GPa in the MBSGCP simulation and occurs on slip system 2, 12, 5 and 8 right under the indenter tip and thus exceeds the maximum value in the conventional simulation by far. Further away from the indent however, the value of g_{GND} on all slip systems decreases faster than g_{SSD}. It can be concluded, that in the regions close to the indent from about two microns left to two microns

right of the indenter axis and down to about 5 microns under the surface, geometrically necessary dislocations influence the strengthening of the material significantly. Outside this region, the influence decreases and strengthening is mainly caused by g_{SSD}.

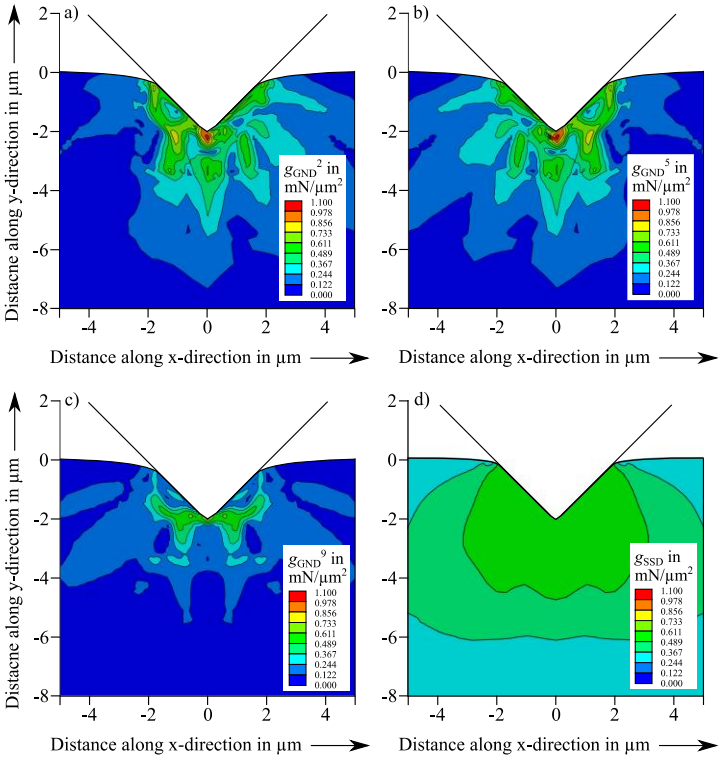

Figure 37: Distributions of the critical resolved shear stress g for slip system 2 and 12, 5 and 8 as well as 9 and 10 in the mechanism-based strain gadient crystal plasticity simulation in a), b), c) and in the conventional CP simulation in d)

The contribution to strain hardening due to GNDs generally differs on every slip system since it is calculated based on the density of geometrically necessary dislocations (see equation (2.22)). Thus, it is useful to determine the sum of g_{GND} for the investigation of the evolution of the contribution to strain hardening due to GNDs dependent on the indentation depth. The following figure 38 shows the sum of g_{GND} over all active slip systems for the two indentation depth 2 µm and 4 µm on the left and right side of the figure, respectively. One has to note, that the dimensions of the right plot are twice the dimensions of the left plot. For a detailed investigation of the overall contribution of GNDs to the hardening, the plots are evaluated along the three semicircular paths shown in figure 38. Since the indentation depth is 2 µm and 4 µm in the two compared deformation states, the distances between the paths is double, too.

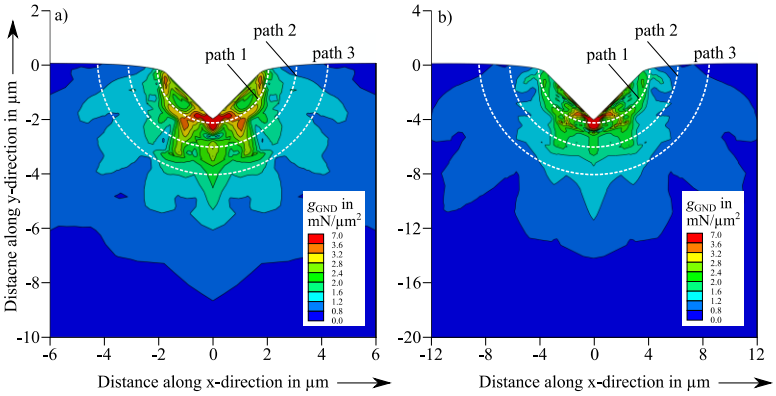

Figure 38: g_{GND} under the indent at a) 2 µm and b) 4 µm indentation depth, determined in the single-layer MBSGCP simulation

The overall contribution to the hardening due to GNDs along the three paths is plotted in figure 39. For a comparison, the distance along the path is normalized for both indentation depths. Along all path, g_{GND} is significantly higher for the smaller indentation depth of 2 µm. Solely along path 1, a higher value occurs right under the indenter tip for the indentation depth of 4 µm. This is

most likely because the elements under the indenter tip are highly distorted with increasing indentation depth and the results right under the tip are not trustworthy. However, on path 2 and 3, further away from the indenter tip, the values at the indenter axis are always smaller for the indentation depth of 4 µm.

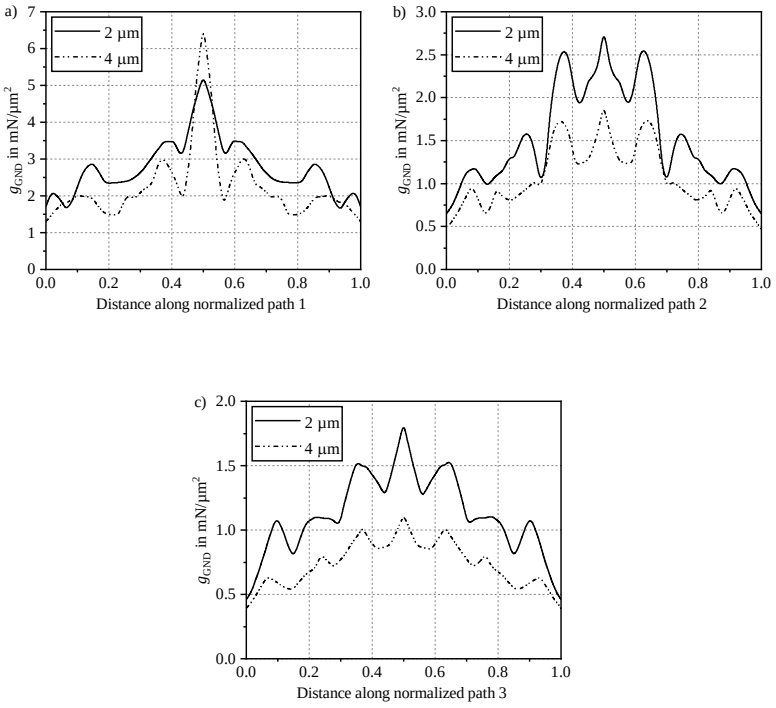

Figure 39: g_{GND} along the paths 1, 2 and 3 under the indenter at 2 µm and 4 µm indentation depth in a), b) and c)

The investigation of g_{GND} along the paths for the two different indentation depths show that the contribution to the overall hardening decreases with increasing indentation depth.

According to equation (2.22) this also means that the GND density decreases with increasing indentation depth. Additionally, it confirms that the implemented mechanism-based strain gradient crystal plasticity subroutine is capable of describing the experimentally observed size dependency in nanoindentation.

6.3.5 Size effect

It was shown in the former chapter that the contribution to hardening due to GNDs, g_{GND} decreases with increasing indentation depth and thus, the single crystal deforms easier at higher indentation depths. This size dependency was investigated in detail by the comparison of the load-displacement curves and the hardness between the conventional and mechanism-based strain gradient crystal plasticity simulation.

The load-displacement curves, the fingerprints of a nanoindentation simulation, are showed in figure 40. The comparison reveals a significantly higher load that is necessary to achieve the defined indentation depth of 2 µm in the MBSGCP simulation.

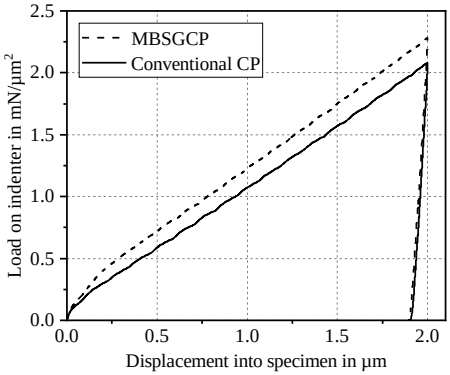

Figure 40: Load-displacement curves determined in the conventional and mechanism-based strain gradient crystal plasticity

This result agrees well with the much higher stresses and resolved shear stresses that were determined in the mechanism-based strain gradient crystal plasticity simulation in comparison to the conventional simulation. Thus, for an indentation depth of 2 µm, a significant size effect occurs and the material at this length scale has a much higher resistance against plastic deformation.

Beside the analysis of the simulation of the single-layer model up to an indentation depth of 2 µm, the simulation was extended to an indentation depth of 5 µm to investigate how the deformation response, represented by load-displacement curves, changes at higher indentation depths. Consequently, simulations up to three indentation depths, 1.5 µm, 2 µm and 5 µm, were performed and the normalized load-displacement curves were determined following Lewandowski et al. (Lewandowski and Stupkiewiez 2018a, 2018b). Both, the load and the indentation depth were normalized with the particular maximum indentation depth h_{max}. Figure 41 shows the results for the MBSGCP and the conventional CP simulation with the normalized load F/h_{max} and normalized displacement h/h_{max} at the ordinate and abscissa, respectively.

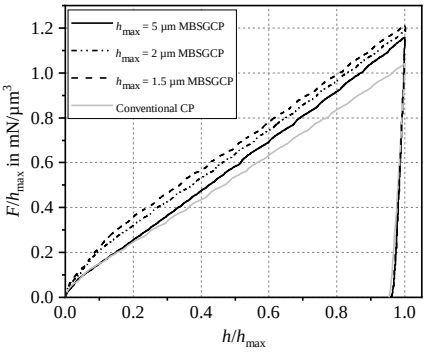

Figure 41: Normalized load-displacement curves determined in the conventional and mechanism-based strain gradient crystal plasticity simulation for the three indentation depth of 1.5µm, 2 µm and 5 µm

For all indentation depths, the normalized curves are the same in the conventional CP simulation since no size effect can be described with this theory. The normalized curve up to the indentation depth of 1.5 µm in the MBSGCP simulation is higher, than normalizing the load-displacement curve up to an indentation depth 2 µm or 5 µm simulations. The difference between the curves determined in the 1.5 µm and 5 µm indentation depth simulation is about 6%. The curve determined in the conventional CP simulation is even lower, indicating that at 5 µm indentation depth, still an influence of the size effect is present.

In addition to the load displacement curves, the hardness H of the single crystal was investigated in detail. The definition of the hardness used in the following is F/A, where F is the load on the indenter in global y-direction and A is the true area between the indenter and the specimen that is determined in ABAQUS directly. The results of the hardness show a strong scattering due to the stair cased evolution of the contact area (caused by the surface elements coming in contact with the indenter after each other). Thus, the curves were smoothed and are shown as moving average in figure 42. The investigation of the hardness shows a significant increase for indentation depths under 1 µm in the conventional crystal plasticity simulation with a sharp tip. A similar effect was observed by Qu et al. (Qu et al. 2004). However, this effect is not a size effect but a dependency of the hardness on the indenter tip radius. To investigate this in more detail, the conventional single-layer simulation was performed with three different wedge indenter tips with a radius of 0.0 µm, 0.2 µm and 0.5 µm. The result of the hardness for the three simulations show that with increasing radius, the hardness decreases at smaller indentation depths. For a small tip radius, it is supposed that the FE-mesh is too coarse to describe the exact contact area for small indentation depths and underestimates the area for small indentation depth. In case of the large tip radius of 0.5 µm, the contact at small indentation depths corresponds to a spherical indentation and the contact area is larger for small indentation depth, leading to an underestimation of the hardness.

However, figure 42 a) shows that for an indentation depth larger than 1 µm, the hardness determined in the conventional CP simulation is constant. The curve determined in the mechanism-based strain gradient crystal plasticity simulation with a perfectly sharp indenter tip however, shows a decrease between 1.0 µm and 5.0 µm and approaches the conventional crystal plasticity curves. The plot of $1/h$ and $(H/H_0)^2$ (where H_0 is the hardness value at the infinite indentation depth with a value of 6.6 mN/µm^2) in figure 42 b), shows the approach of the two curves for the indentation depth between 1.0 µm and 5.0 µm even clearer. The increase of hardness under $1/h = 0.4$ µm^{-1} occurs due to larger elements making contact with the indenter as the indentation depth exceeds 2.5 µm, leading to an underestimation of the contact area.

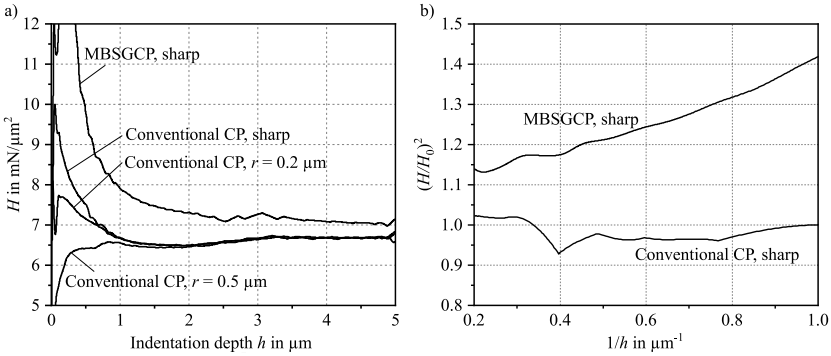

Figure 42: a) hardness detemined in the conventional crystal plasticity single-layer model for a sharp tip and the radius of 0.2 µm and 0.5 µm together with the MBSGCP single layer simulation result determined with the sharp indenter; b) depth dependence determined with the sharp indenter and the conventional and MBSG crystal plasticity model following Nix and Gao (Nix and Gao 1998)

6.3.6 Crystal lattice rotation and GND density

The Euler angles following Bunge were determined in the MBSGCP single-layer simulation corresponding to the conventional CP simulation. The first Euler angle describes the in-plane lattice rotation and is shown in figure 43.

Due to plane strain conditions, the second and third Euler angles are constant over the whole indentation process. Like in the conventional CP simulation, the maximum in-plane lattice rotation is about ±20° around the indenter. The lattice rotation pattern exhibits an antisymmetry with respect to the indenter axis. The highest rotation occurs at the flanks of the indenter and right under the indent. Along the indenter axis, a change of sign occurs and the rotation decreases to zero.

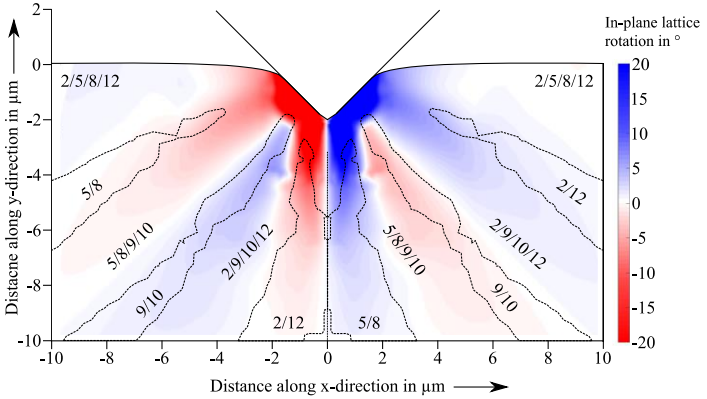

Figure 43: First Euler angle φ_1 in the MBSGCP single-layer simulation, representing the in-plane lattice rotation

Further away from the indent, fan-shaped regions can be identified with alternating positive and negative rotation. The regions correspond to the slip system activity map shown in figure 33. The boarders of regions where solely one effective slip system is active are marked in the figure. In these regions either positive or negative lattice rotation occurs. In between these regions, where two effective slip systems are active, a sign change of the crystal lattice rotation and thus, a decrease of the lattice rotation to zero occurs. Consequently, always two of the effective slip systems must cancel the lattice rotation out if they are equally active, leading to the fan-shaped lattice rotation pattern. In the region

close under the indent where all slip systems are active, the largest lattice rotation occurs. Overall, the pattern of crystal lattice rotation determined in the MBSGCP and the conventional CP are similar.

Figure 44 shows the density of geometrically necessary dislocations as sum of the GND density on the individual six active slip systems determined in the mechanism-based strain gradient crystal plasticity simulation following equation (2.21) instead of a GND density determined with the KAM method, based on the crystal lattice rotation. However, the result is visualized in the same manner as the GND density determined by KAM in the conventional CP simulation. Following Han et al. (Han et al. 2005), the unit of the effective density of GNDs is 1/µm instead of 1/m^2. The distribution of GNDs is symmetric with respect to the indenter axis. The highest density occurs under the indenter tip and in regions starting the left and right contact points and emanating downwards. Under the indenter flanks, solely a small GND density is present. The comparison with the resolved shear stress shows an expected correlation between regions on slip system 2, 5, 8, and 12 with high resolved shear stress and the regions of high GND density.

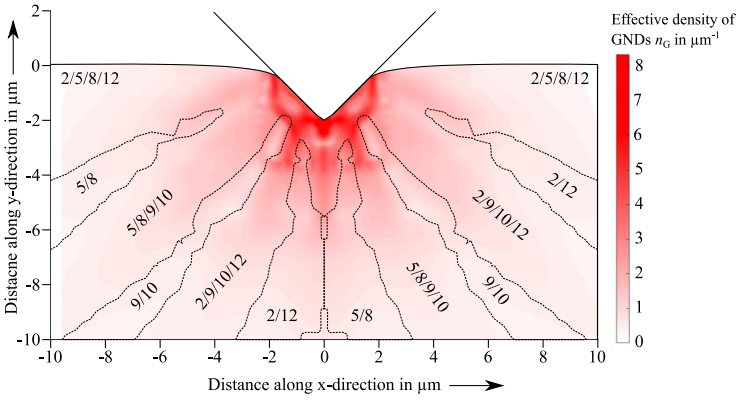

Figure 44: Effective density of geometrically necessary dislocations n_G in the midsection of the brick-shaped conventional crystal plasticity simulation at the indentation depth of 2 µm, determined in the MBSGCP subroutine following Han et al. (Han et al. 2005)

While the highest density occurs under the indent, fan-shaped regions further away can be identified with low and higher GND densities. Like in the plot of the crystal lattice rotation, the boarders between regions where one or two effective slip system are active are shown in the plot of the GND density. Here, a region where mainly one effective slip system is active, correspond to a region with low and a region where two effective slip systems are active with high GND density. The reason for this are small gradients in regions where solely one effective slip system is active. In the border areas between two regions with only one effective slip system, the two adjoining effective slip systems decrease or increase, respectively, causing higher strain gradients and thus, a higher density of geometrically necessary dislocations, explaining the shape of the GND density distribution.

6.4 Results of the [0$\bar{1}$0] oriented brick-shaped non-Schmid crystal plasticity simulation

The brick-shaped model as described in chapter 5.2 together with the non-Schmid version of CP as material law was used for an FE-simulation of the 90° wedge nanoindentation into the [0$\bar{1}$0] oriented tungsten single crystal. The same definitions regarding crystal orientation, indentation speed, increment size, active slip family and material parameters were defined as in the conventional crystal plasticity simulations. The aim of the investigations is to study the influences of non-Schmid effects on the plastic deformation behavior. For this purpose, the activities of slip systems, the stress state, slip increments, crystal lattice rotation, GND density, material pile-up and load-displacement curve were analyzed in the midsection and compared to the conventional CP results.

6.4.1 Influence of non-Schmid effects on strain conditions

Internally in the subroutine, the 24 non-Schmid slip systems are ordered according to table 1 in chapter 2.4. For the comparison with conventional CP

results, not only the plastic shear γ^{α} of the two collinear slip systems are merged but also renumbered and assigned to the conventional CP slip systems as shown in appendix A.7. In the following, only the added plastic shear values are given and the numbering of slip systems α corresponds to the one of the conventional CP subroutine.

The non-Schmid simulations shows, that just like in the conventional CP simulations, slip systems 1, 3, 4, 6, 7 and 11 are inactive over the whole indentation process. The simulation shows in addition, that the three pairs of active slip systems 2 and 12, 5 and 8 as well as 9 and 10 (shown in figure 45) exhibit the same resolved shear stress and plastic shear, like in the conventional CP simulation. The comparison of the non-Schmid tensors of active slip shows that the components P_{11}^{NoS}, P_{12}^{NoS}, P_{21}^{NoS}, P_{22}^{NoS} and P_{33}^{NoS} are the same for each of the mentioned pairs of slip systems. Other components of the non-Schmid tensor are negligible since the simulation shows that the stress components σ_{13}, σ_{31}, σ_{23} and σ_{32} are zero in the investigated midsection. These findings confirm corresponding plastic shear and shear stress on slip systems 2 and 12, 5 and 8 and 9 and 10 found in the simulation. These findings show, that non-Schmid effects do not violate the plane strain conditions in the midsection of the brick-shaped model. However, deviations of plastic shear on active slip systems between the non-Schmid and conventional CP results are likely and investigated in detail in the following chapter.

6.4.2 Slip system activity

As mentioned above, solely six slip systems are active and always two of these correspond regarding shear stress and plastic shear. Thus, only the plastic shear on one of the corresponding slip systems is shown in figure 45 in the midsection. Plastic shear on slip system 9 (and 10) is like in the conventional CP simulation antisymmetric with respect to the indenter axis and mirrored in case of slip systems 2 and 5 (12 and 8). The contour plots of plastic shear on slip system 2 and 5 determined in the non-Schmid and conventional crystal plasticity simulation are similar.

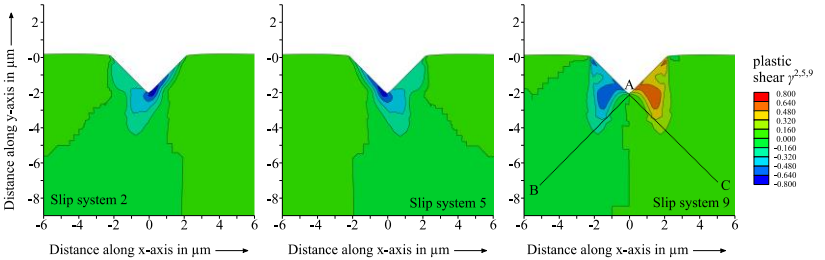

Figure 45: Slip system activity of slip systems 2, 5 and 9 (corresponding to slip system 12, 8 and 10 respectively) in the midsection of the non-Schmid crystal plasticity brick-shaped simulation underneath the indent at the indentation depth of 2 µm.

The maximal absolute value however, occurring near under the indenter tip in both simulations, is with 0.766 higher than in the non-Schmid than in the conventional simulation where a maximal value of 0.724 was determined. Slip system 9 (and the corresponding slip system 10) behave significantly different in the two simulations. The regions where plastic shear occurs under the indent is larger in the non-Schmid simulation and occurs mainly in the region underneath the indent but hardly left and right of it. The maximal value determined on slip system 9 and 10 is with ±0.644 in the non-Schmid simulation much higher than in the conventional CP simulation where the maximum value is solely ±0.558. Therefore, the non-Schmid effects promote dislocation mobility mainly on slip system 9 and 10 but do not have a significant influence on slip system 2, 5, 8 and 12.

Figure 46 shows the indentation profiles determined in the midsection with the non-Schmid and conventional CP model. The profiles exhibit a symmetry with respect to the indenter axis and thus only the right side is shown in the figure. Significantly more material pile-up at the indenter flanks occurs in the non-Schmid crystal plasticity simulation. For a deeper understanding of this result, again the plastic shear along four paths shown in figure 46 were investigated.

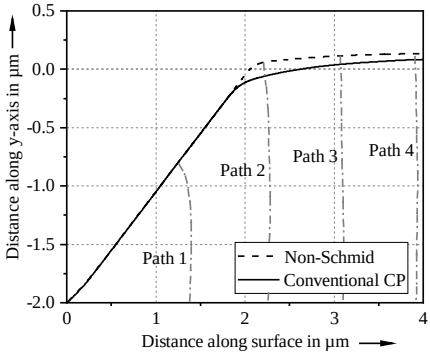

Figure 46: Indentation profiles determined in the conventional and non-Schmid brick-shaped wedge indentation simulations at the indentation depth of 2 µm

Along these four paths, the cumulative plastic shear and plastic shear on slip system 9 and 10 are shown in figure 47 a), b), c) and d). Along path 1, 2, 3 and 4, both, the cumulative plastic shear and individual shear on slip system 9 and 10 are much lower in the non-Schmid than in the conventional simulation. In the MBSGCP simulation however, higher cumulative plastic shear and shear on slip system 9 and 10 occurred. So with the assumption that slip on slip system 9 and 10 mainly influences material pile-up at the surface, less plastic shear on these two slip systems as it occurs in the non-Schmid simulation leads to more material pile-up while more plastic shear as observed in the MBSGCP simulation, results in much less material-pile-up than in the conventional crystal plasticity simulation. Along path 1, higher plastic shear on slip system 9 and 10 and cumulative shear occurs which however, does not influence the material deformation behavior right of the indenter.

The slip system activity map determined in the non-Schmid simulation in figure 48 shows the same overall fan-shape like in the conventional and MBSG crystal plasticity simulations.

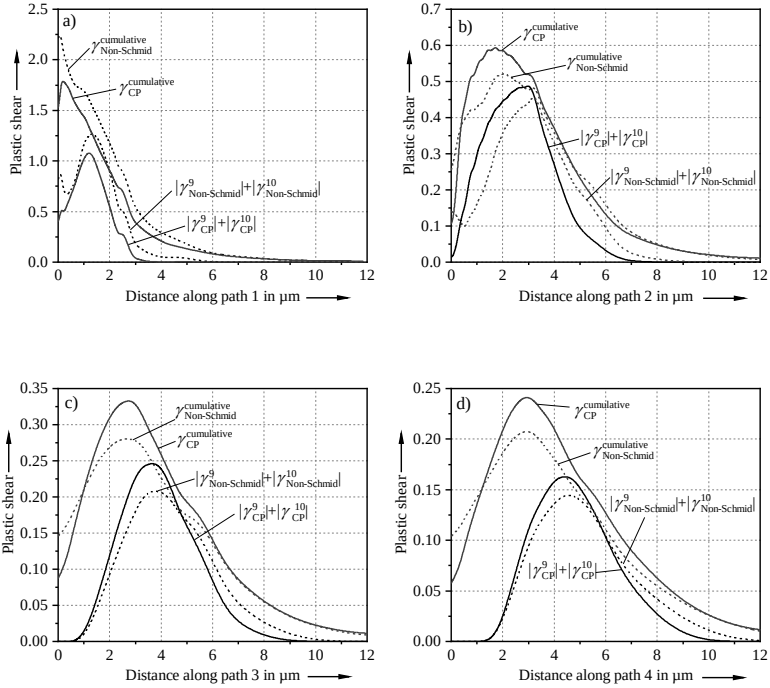

Figure 47: Plastic shear on slip systems 9 and 10 together with the cumulative plastic shear along path the four paths 1, 2, 3 and 4 in a), b), c) and d)

All six slip systems are active under the indenter. Emanating from the indent, three regions where the three effective slip systems 5/8, 9/10 and 2/12 are active, left and right of the indenter axis occur. In between, transition regions occur in which always the two adjoining slip systems are active. Although it was shown in the investigation of individual slip systems that more plastic shear occurs in the non-Schmid simulation, the overall shape of the slip system activity map is not significantly influenced by non-Schmid effects.

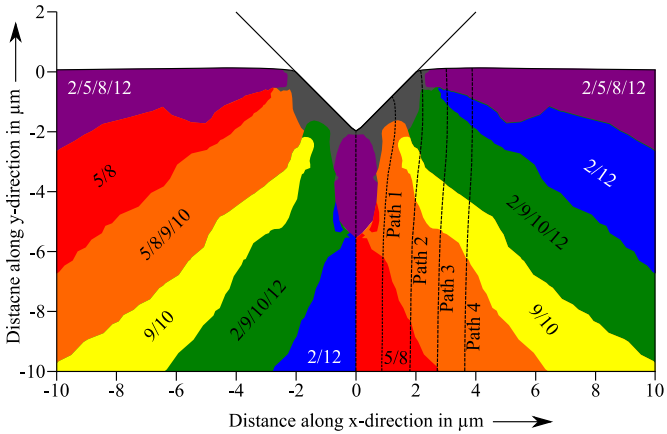

Figure 48: Slip system activity map underneath the indenter in the non-Schmid crystal plasticity simulation

6.4.3 Stress state

Just like in the conventional and mechanism-based strain gradient crystal plasticity simulation, the driving force causing plastic shear is solely the three stress components σ_{11}, σ_{22} and σ_{12} in the midsection of the non-Schmid brick-shaped simulation. The distribution of σ_{12} and $(\sigma_{11}\text{-}\sigma_{22})/2$ are shown in figure 49. The overall shapes of the contour plots are similar to the ones in the mechanism-based and conventional crystal plasticity. In the distribution of $(\sigma_{11}\text{-}\sigma_{22})/2$, there is a region with positive values at the flanks and underneath the indent. Even more pronounced than in the conventional crystal plasticity simulation, a band in the distribution of $(\sigma_{11}\text{-}\sigma_{22})/2$ emanates from the contact point almost vertically downwards in which the value of $(\sigma_{11}\text{-}\sigma_{22})/2$ decreases to zero. Left and right of these bands, two regions with negative values of $(\sigma_{11}\text{-}\sigma_{22})/2$ adjoin. About 3 µm under the surface of the specimen, the bands in which $(\sigma_{11}\text{-}\sigma_{22})/2$ is zero bend outwards under an angle of approx. 45° with respect to the surface. Within these bands, solely shear stress σ_{12} occurs, and thus only the effective slip system 9/10 is active following the yield surface

determined in chapter 6.1.2. At the indenter flanks and under the indenter tip, a large region with a positive value of $(\sigma_{11}\text{-}\sigma_{22})/2$ occurs.

The distribution of σ_{12} in the midsection has two areas limited by the line 1 and 6 and the surface of the specimen in which σ_{12} is zero. Between line 3 and 4 under the indent and at the indenter flanks, σ_{12} is zero as well. However, there are two regions in which shear stress occurs, one left of the indent with negative shear stress between line 1 and 3 and on the right side of the indenter between line 4 and 6 with positive value of σ_{12}.

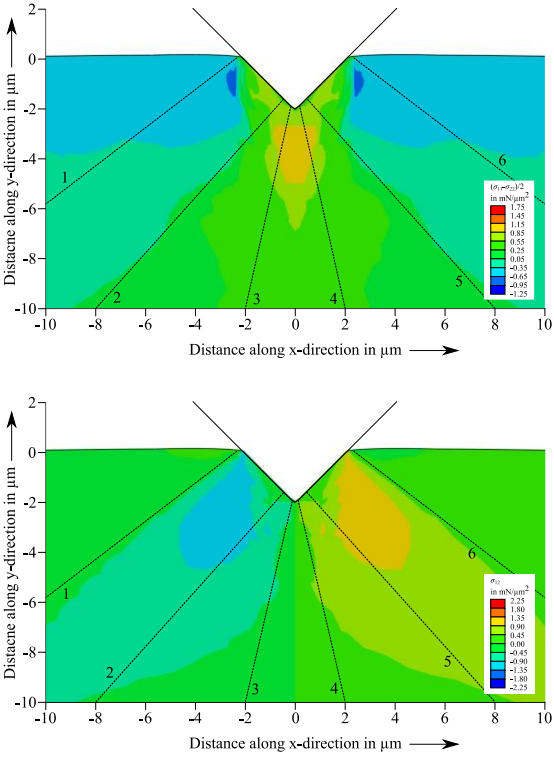

Figure 49: Distribution of $(\sigma_{11}\text{-}\sigma_{22})/2$ and σ_{12} in the Non-Schmid brick-shaped model under the indent at the maximum indentation depth of 2 µm

6.4.4 Increments of plastic shear

Following the investigation of the plastic shear increments in the conventional crystal plasticity simulation, $\dot{\gamma}^{\alpha}$ is evaluated for the non-Schmid simulation for the three indentation depths of 1.0 µm, 1.5 µm and 2.0 µm. The results are shown for slip system 2, 5 and 9 in figure 50. For a comparison, the same increment size of $7.5 \cdot 10^{-5}$ s was chosen in the non-Schmid as in the conventional simulation. Like in the conventional CP simulation, the plots of plastic shear increments of slip system 9/10 are antisymmetric with respect to the indenter axis. The plots of slip system 2/12 and 5/8 are mirrored. On slip system 2 and 12, respectively, a band with high $\dot{\gamma}$ emanates from the left contact point downwards in all indentation depths. Under the right indenter flank, there is a region where the slip systems are active in the current increment. Like in the conventional simulation, the activity under the flank decreases with higher indentation depths. The values $\dot{\gamma}$ and the distribution are similar in the non-Schmid and conventional crystal plasticity simulation. This was indicated by the comparison of the individual slip system activities showing a similar result for slip systems 2, 5, 8 and 12. Again, the same values but mirrored distributions of plastic shear increment were determined for slip systems 5 and 8 for the three different indentation depths. A significant difference however, appears between the slip systems 9 and 10 in the non-Schmid and conventional simulation. Although all the contour plots of slip system 9 and 10 show the two antisymmetric bands emanating downwards from the two contact points, two significant differences occur. First, the absolute values of $\dot{\gamma}$ are higher in the non-Schmid simulation. Secondly, the bands emanate downwards vertically in the non-Schmid whereas they bend outwards in the conventional simulation. Both was already indicated by the comparison of the plastic shear on slip system 9 and 10 showing higher absolute values and plastic shear only in the vertical region under the indent in the non-Schmid simulation but also left and right of the indent in the conventional CP simulation. However, like in the conventional simulation, the bands in which high plastic shear increments occur, emanating from the contact point on all slip systems, propagate outwards with the contact point with increasing indentation depth.

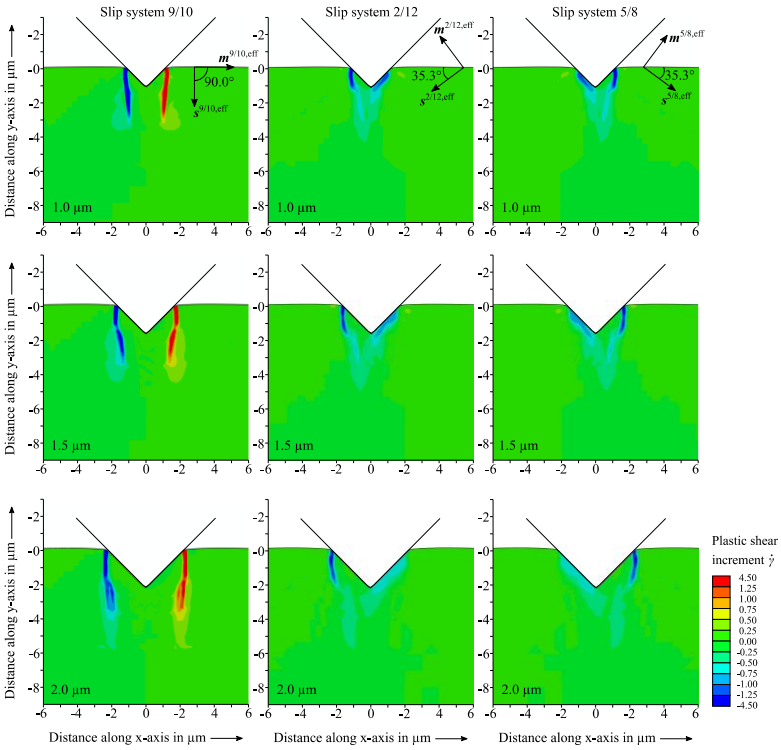

Figure 50: Increments of plastic shear $\dot{\gamma}$ at the three indentation depths 1 µm, 1.5 µm and 2 µm in the midsection of brick-shaped non-Schmid simulation

Figure 51 shows the plastic shear increment map of the right side of the indent, determined in the non-Schmid simulation in the same manner than in the conventional CP simulation. In addition, the shear increments along the circular path are plotted in figure 52. At the start of the path at the indenter axis, in region I, slip systems 2, 5, 8 and 12 are active followed by a small region where solely the effective slip system 5/8 is active. Between approximately 2 and 3 µm, plastic shear occurs on slip systems 5/8 and 9/10.

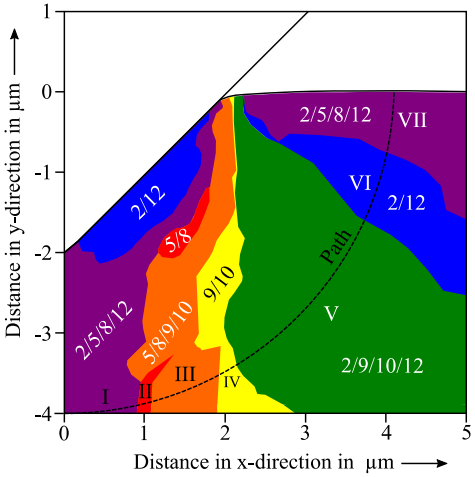

Figure 51: Plastic shear increment map of the right side of the indent in the non-Schmid brick-shaped simulation at the indentation depth of 2 µm

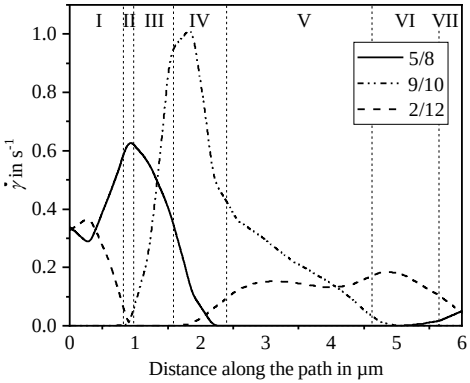

Figure 52: Plastic shear increment along the circular path highlighted in figure 51

At about 2 µm on the path, plastic shear occurs almost solely on the effective slip system 9/10 followed by a large region where the effective slip systems 2/12 and 9/10 are active. At the end of the path, the overall value of the plastic shear increment decreases significantly and at approximately 5 µm, only slip system 5/8 is active. Close under the surface, the plastic shear increments decrease to a very small value. Overall, the plastic shear increment map determined in the non-Schmid simulation is similar to the conventional crystal plasticity result. The peaks of effective slip systems along the circular paths are slightly shifted but overall, the distribution along the path is quiet similar.

6.4.5 Crystal lattice rotation and GND density

For the determination of the crystal lattice rotation in the non-Schmid brick-shaped simulation, the same SciPy griddata interpolation method (The SciPy community 2019) was used than in the conventional and mechanism-based strain gradient crystal plasticity simulation and was plotted in Matlab (MathWorks). Since plane strain conditions occur in the midsection of the brick-shaped model, the first Euler angle φ_1 following Bunge represents the in-plane lattice rotation and is plotted in figure 53.

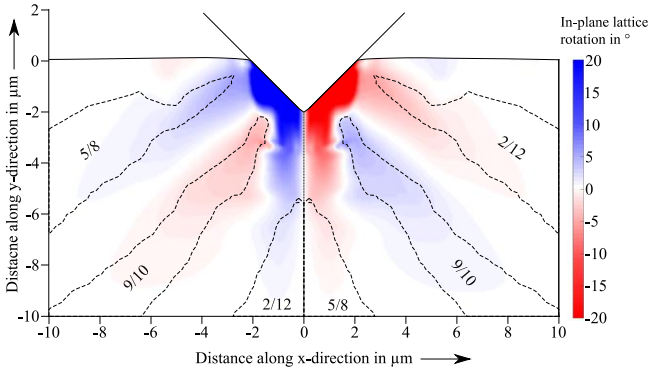

Figure 53: First Euler angle φ_1 in the midsection of the non-Schmid brick-shaped model, representing the in-plane lattice rotation

The overall shape of the lattice rotation corresponds well to the results of the conventional and mechanism-based strain gradient crystal plasticity simulation. The plot exhibits a antisymmetry with respect to the indenter axis. Left and right under the indenter, regions with high lattice rotation occurs, corresponding to the regions under the indenter where high plastic shear on all active slip systems occurs. Further away, fan-shaped regions occur with alternating regions with positive and negative rotation. Just like in the conventional and mechanism-based strain gradient crystal plasticity simulations, a link between the slip system activity map and the lattice rotation exists. In regions where two effective slip systems are active, the lattice rotation decreases to zero but is rather positive or negative in regions where solely one effective slip system is active.

Overall, the distribution of the density of geometrically necessary dislocations determined by the kernel average misorientation method under the indent in the midsection of the brick-shaped model in the non-Schmid simulation agrees with the results from the conventional crystal plasticity simulation. There are two bands emanating from the contact points and another one starting at the indenter tip along the indenter axis.

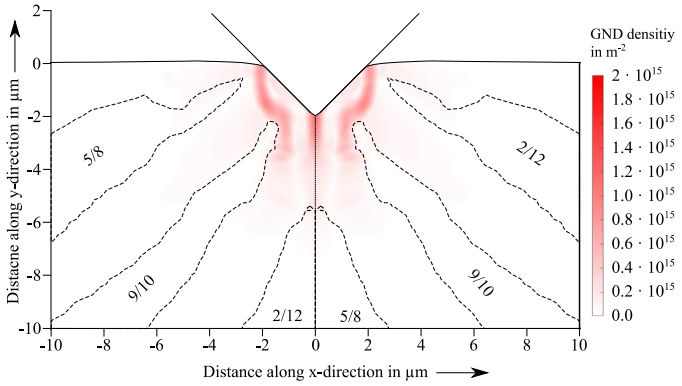

Figure 54: Density of geometrically necessary dislocations in the midsection of the brick-shaped non-Schmid crystal plasticity simulation at the indentation depth of 2 µm, determined with the kernel average misorientation method

There are almost no GNDs occurring right under the indenter flanks. Corresponding to the conventional CP results, a fan-shaped distribution of the GND density further away from the indent occurs with higher GND densities in the regions where two effective slip system are active.

6.4.6 Load-displacement curves

Last, the load-displacement curves of the brick-shaped non-Schmid and conventional crystal plasticity simulations are compared. Figure 55 shows the two load-displacement curves determined in the two simulations. The necessary load in the non-Schmid simulation is significantly lower than in the conventional simulation. This confirms the result of the stress state investigated in chapter 6.4.3 where significantly lower stresses were found to occur in the non-Schmid than in the conventional CP simulation. Both, the lower occurring stresses and load-displacement curves in the non-Schmid simulation can be explained by the non-Schmid effect.

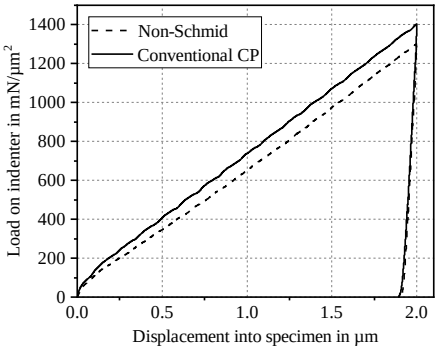

Figure 55: Comparison of the load-displacement curves determined in the conventional and non-Schmid crystal plasticity brick-shaped simulations

As shown above, the Non-Schmid effect does not influence the effective slip system 2/12 and 5/8 but leads to more plastic shear on slip system 9/19 despite the lower occurring stress in the midsection. Thus, the non-Schmid effect on slip system 9/10 promotes the plastic deformation behavior, i.e. the single crystal deforms easier in the non-Schmid simulation.

6.5 Results of the [0$\bar{1}$0] oriented bridge-shaped crystal plasticity simulation

After the principle investigations using the brick-shaped and single-layer model together with the conventional, non-Schmid and mechanism-based strain gradient crystal plasticity, the brick-shaped model was set up for a comparison of the numerical and experimental results. The model was defined to meet the boundary conditions and geometry of the experimentally indented bridge described in detail in chapter 4. Together with the conventional and non-Schmid crystal plasticity subroutines, it was used to simulate the wedge nanoindentation into the [0$\bar{1}$0] oriented tungsten single crystal. The aim of both simulations is a comparison of the numerically determined deformed geometry after indentation, the crystal lattice rotation and the density of geometrically necessary dislocations to the experimental results, determined by Wang.

6.5.1 Strain conditions in the [0$\bar{1}$0] oriented bridge-shaped model

Due to its small thickness of 4.3 µm, plane strain conditions no longer occur in the midsection of the bridge-shaped model. Now slip systems 1, 6, 7 and 11 are active in addition to the six active slip systems (2, 5, 8, 9, 10 and 12) in the thick brick-shaped model (see table 9). Because of the symmetry, the stress components σ_{23} and σ_{31} are still zero in the midsection. Therefore, slip systems 3 and 4 with all Schmid-tensor components except P_{13}, P_{23}, P_{31} and P_{32} being zero are inactive over the whole indentation process. For the slip systems 1, 6, 7, and 11, the product $s_3 m_3$ is no longer zero (see table table 9 listing the slip

plane normals and slip directions in the initial state in the midsection of the brick-shaped and bridge-shaped model) and therefore, the driving force on these slip systems depends on σ_{33}.

A detailed analysis of the computed slip system activity reveals that the newly active slip systems 6 and 7 as well as 1 and 11 correspond in their amount just like slip systems 2 and 12, 5 and 8, and 9 and 10 in the chosen $[0\bar{1}0]$ orientation do: $\gamma^1 = -\gamma^{11}$, $\gamma^6 = \gamma^7$, $\dot{\gamma}^1 = -\dot{\gamma}^{11}$ and $\dot{\gamma}^6 = \dot{\gamma}^7$. The contour plots of plastic shear of the five slip systems are shown in figure 56 and figure 57. Again solely five slip systems are shown, representing the corresponding slip systems. The maximum plastic shear on slip systems 1, 6, 7 and 11 is about the same value as on the slip systems 2, 5, 8, and 12. On the slip systems 9 and 10, the absolute values of maximum plastic shear is slightly smaller. So, in the bridge-shaped model, the plastic deformation in the midsection is significantly driven by the slip systems 1, 6, 7 and 11 which were not active in the brick-shaped model. The regions where slip occurs on slip systems 2, 5, 8 and 12 in the bridge-shaped simulation are still similar to the brick-shaped simulation. Slip systems 2 and 5 (and so 8 and 12) are mirrored again. The same holds for slip systems 1 and 6 (and so 7 and 11). Slip systems 9 and 10 are still antisymmetric with respect to the indenter axis. So the difference between the brick-shaped and bridge-shaped model is mainly the activity of the four slip systems 1, 6, 7 and 11. Based on these findings, two additional effective slip systems can be defined by the combination of slip system 1 and 11 as well as 6 and 7. For the six slip system 2, 5, 8, 9, 10 and 12, the determination of the effective slip systems performed in chapter 6.1.1 and appendix A.6, is still valid.

Consequently, the rate of stretching $\boldsymbol{D}_s^{1/11}$ of the effective slip system 1/11 can be determined following the equation:

$$\boldsymbol{D}_s^{1/11} = \dot{\gamma}_s^1 \boldsymbol{P}_s^1 + \dot{\gamma}_s^{11} \boldsymbol{P}_s^{11} = \dot{\gamma}^{1/11} \begin{pmatrix} 0 & 1 & 0 \\ 1 & -2\sqrt{2} & 0 \\ 0 & 0 & 2\sqrt{2} \end{pmatrix}. \tag{6.10}$$

In the same manner, the rate of stretching $\boldsymbol{D}_s^{6/7}$ can be determined for slip system 6 and 7:

$$\boldsymbol{D}_s^{6/7} = \dot{\gamma}_s^6 \boldsymbol{P}_s^6 + \dot{\gamma}_s^7 \boldsymbol{P}_s^7 = \dot{\gamma}^{\frac{6}{7}} \begin{pmatrix} 0 & -1 & 0 \\ -1 & -2\sqrt{2} & 0 \\ 0 & 0 & 2\sqrt{2} \end{pmatrix} = \dot{\gamma}^{6/7} \boldsymbol{P}_s^{6/7,eff}. \qquad (6.11)$$

Thus, slip systems 1, 6, 7 and 11 cause strain in the global z-direction and out of plane rotation is likely to occur also in the midsection. However, the investigation of the Euler angles show that the lattice rotation occurs mainly in the midsection and solely the first Euler angle changes significantly while the second and third Euler angles exhibit only a change between approx. ±1.0° under the residual imprint. Based on this investigation, the comparison of the lattice rotation between the experimental results and the conventional and non-Schmid simulation was performed solely for the first Euler angle while θ and φ_2 where neglected in the following comparison in the next chapter.

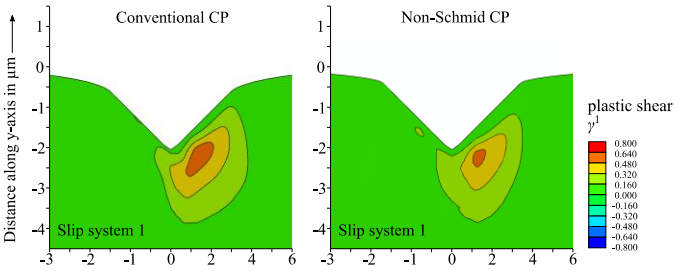

Figure 56: Plastic shear on slip system 1 (corresponding to 7) in the midsection of the bridge-shaped model at the indentation depth of 2 µm determined in the conventional and non-Schmid crystal plasticity simulation

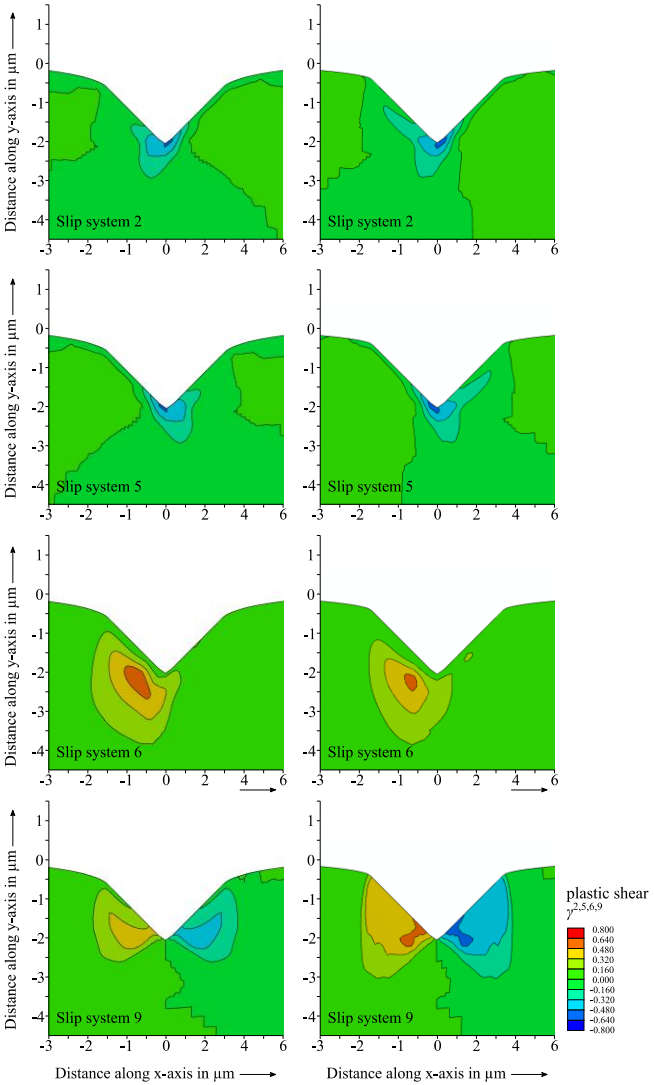

Figure 57: Plastic shear on slip systems 2, 5, 6 and 9 (corresponding to 8, 10, 11 and 12) in the midsection of the bridge-shaped model at the indentation depth of 2 µm determined in the conventional and non-Schmid crystal plasticity simulation

6.6 Comparison of numerical and experimental results

6.6.1 Residual imprint geometry

The profiles of the imprints in the midsection after unloading determined in the experiment, the conventional and the non-Schmid crystal plasticity simulation are shown in figure 58. The surface profile of the imprint is symmetric with respect to the indenter axis and thus, solely the profile of the right part of the imprint is shown in the figure.

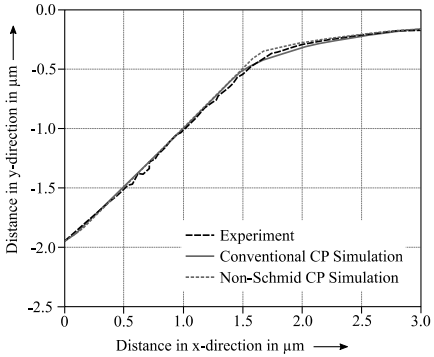

Figure 58: Indentation profiles in the midsection of the experiment, conventional and non-Schmid simulation after unloading

A comparison of the three shown profiles reveals a good agreement of profiles determined in the experiments and calculated in the conventional CP simulation. The profile in the non-Schmid result is slightly higher than in the conventional CP simulation. The reason was discussed in chapter 6.4.2. The input parameters used for the simulation determined by Yao (Yao 2012) were fitted to spherical and Berkovich indentation into tungsten single crystals in conventional crystal plasticity simulations and not non-Schmid simulations. The investigations of Yao (Yao 2012) also showed that the indentation profiles are

significantly influenced by the material parameters h_0, τ_s, τ_0 and the hardening exponent n. As shown in appendix A.4, an increase of the coefficient of friction leads to more pronounced material pile-up. Summarized the profiles of the residual imprint agree quantitatively very well between simulation and experiment.

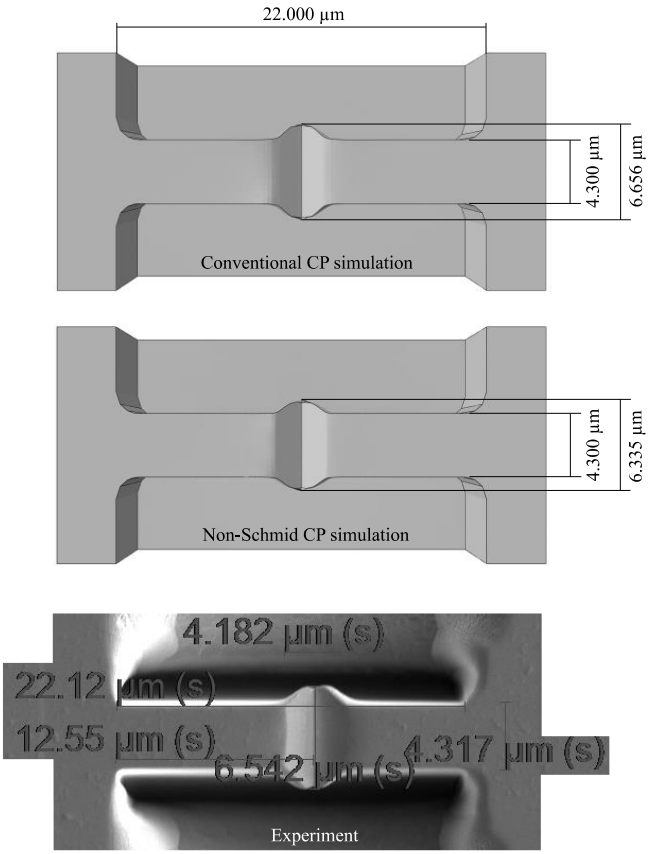

Figure 59: Material pushed out of the side faces of the bridge in the conventional and non-Schmid simulations and in the experiment

Additionally, the shape of the residual imprint was compared regarding the material pushed out of the side faces of the bridge. Figure 59 shows the deformed geometry of the bridge after unloading determined in the experiment (bottom) and the conventional and non-Schmid simulation (top and middle, respectively). The overall deformed shape of the indented bridge of the experiments and the two simulations agrees well.
The material laterally pushed out at the side faces is larger in the conventional than in the non-Schmid simulation. The plastic shear on slip system 1/11 and 6/7 which are responsible for strain in the global z-direction in the midsection shows a higher value in the conventional than in the non-Schmid simulation (see figure 56 and figure 57). This agrees well with the higher peak of pushed out material at the side faces of the bridge. So, the non-Schmid effects on slip system 1/11 and 6/7 lead to less plastic shear on these slip systems, i.e. aggravate plastic shearing.

6.6.2 Comparison of the crystal lattice rotation and GND density

The crystal lattice rotation was determined in the bridge shaped experiment by Wang as described in chapter 4. Based on the EBSD data, the crystal lattice rotation was investigated. As already indicated, the out-of-plane rotation is negligible during wedge indentation into the bridge and thus, solely the first Euler angle is taken to characterize the lattice rotation. Figure 60 shows the first Euler angle as determined in the conventional and non-Schmid simulation and the experimental result. All plots exhibit an antisymmetry with respect to the indenter axis and two regions with high positive and negative rotation under the left and right flanks of the indent, respectively. The overall shape of these regions agrees very well. Under the indenter flanks in the experiment however, the maximum rotation angle is significantly larger. Further away from the indent, the values agree well. Along a virtual arch starting at the free surface of the specimen down to the indenter axis, a positive rotation occurs at the start of the arc in all plots. Further along the arch, the rotation decreases to zero and then enters a region with negative rotation in all plots. Towards the

end of the arch, approaching the indenter axis, the rotation decreases to zero in a region under the indent limited by the two lines $\overline{AB}$ and $\overline{CD}$ in the plot determined in the experiment. However, in both, the conventional and the non-Schmid simulation, again a positive first Euler angle occurs. So, beside the good agreement of the rotation field, there is a significant disagreement in the area between the lines $\overline{AB}$ and $\overline{CD}$ in the experiment and simulation.

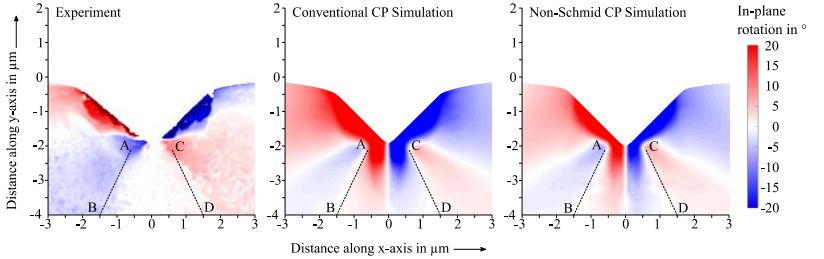

Figure 60: Crystal lattice rotation in the midsection of the bridge in the experiment, the conventional and the non-Schmid crystal plasticity simulation

As Figure 60 shows, gradients of plastic shear and non-Schmid effects hardly change the distribution of the Euler angle. It seems that a phenomenon only appearing in the experiment is seen to be responsible for the disagreement, for example recrystallization i.e. the formation of subgrains under the indenter flanks is not handled in the model. However, this cannot be finally proved in this thesis.

Beside the first Euler angle, representing the lattice rotation, the kernel average misorientation method in the software package MTEX was used to determine the density of geometrically necessary dislocations in the midsection in the simulations and experiment, always based on the three Euler angles. The results are shown in figure 61. The overall GND density is higher in the experiment. High values occur right under the indenter flanks. This may be due to

friction and recrystallization in a small layer under the flanks. In both simulations, no GNDs occur under the flanks. As already described in detail above, in both simulations, bands starting at the contact point emanating downwards to the indenter axis occur with a length of about 3 µm. In the experiment, also two band starting at the contact point can be identified, however, they are connected to the indenter tip and do not point downwards as in the simulation results. This is because no lattice rotation occurs under the indenter tip in the experiments, in contrast to the experiments. Furthermore, another ray starting at the indenter tip along the indenter axis occurs in the simulations but not in the experimental result.

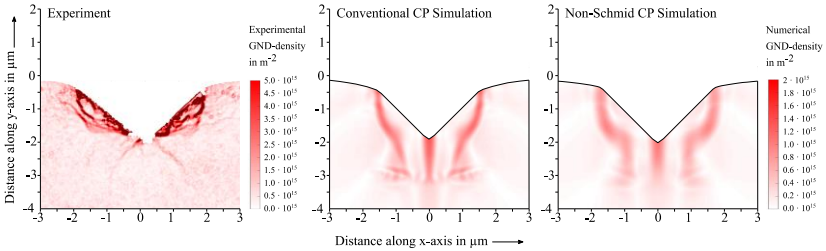

Figure 61: Density of geometrically necessary dislocations in the midsection in the experiment, conventional and non-Schmid simulation determined with the kernel average misorientation method (KAM) based on the crystal lattice rotation

7 Summary and conclusion

In the present work, the plastic deformation behavior of tungsten single crystals on the microscale was investigated using finite-element wedge nanoindentation simulations.

The focus of the first part of this work was thereby to determine constitutive models that area able to describe the indentation size effect and non-Schmid effects. The chosen models, namely the mechanism-based strain gradient and non-Schmid crystal plasticity model were implemented in the conventional CP constitutive model. For a use in the framework of the finite-element method, both models were implemented as extensions for the crystal plasticity subroutine by Huang (Huang 1991) and used together with the commercial FE-software package ABAQUS.

In the second part of the thesis an investigation of the deformation behavior in wedge nanoindentation with the conventional, mechanism-based strain gradient and non-Schmid crystal plasticity model was performed. Therefore, the slip system activities, stress states, increments of plastic shear, deformed geometries, load-displacement curves as well as crystal lattice rotation and density of geometrically necessary dislocations were determined. For the MBSGCP simulation, an additional investigation of the critical shear stress and the indentation size effect was performed. All studies were carried out for the $[0\bar{1}0](101)$ oriented single crystal. To study the orientation influence, the crystal lattice rotation, deformed geometry and load-displacement curves were determined for the $[123](11\bar{1})$ oriented crystal in addition and compared to the results from the $[0\bar{1}0](101)$ simulation. Different FE-models, namely the conventional and non-Schmid simulation with the brick-shaped and the computationally significantly more expensive MBSGCP simulation with the single-layer model were used. The use of the single-layer model was possible since plastic deformation can be described by the sum of dislocation on solely three effective slip systems in the $[0\bar{1}0](101)$ simulation causing plane strain conditions in the midsection of the brick-shaped model.

The third part of this work contains a comparison of the deformed geometry of the indented bridge-shaped specimen, the crystal lattice rotation and the density of geometrically necessary dislocations determined in the numerical study and the experiment conducted by J. Wang at the Karlsruhe Institute of Technology.
The key results and findings are summarized in the following paragraphs.

Conventional crystal plasticity studies

- Based on the activity of individual slip systems, a slip system activity map was determined in the midsection of the model showing fan-shaped regions in which either one or two effective slip systems are active. On these active slip systems, a dependency of plastic shear solely on the stress components σ_{11}, σ_{22} and σ_{12} was found for the $[0\bar{1}0](101)$ oriented crystal. A connection between the activity of slip systems and the stress state was observed. For a better understanding, a yield surface was determined in a two-dimensional stress space with $(\sigma_{11}\text{-}\sigma_{22})/2\tau_c$ on the abscissa and σ_{12}/τ_c on the ordinate. With the yield surface and the distribution of $(\sigma_{11}\text{-}\sigma_{22})/2$ and σ_{12}, the activity of slip systems at points under the indent were determined. The results correspond to the slip system activity map.

- Further, the increments of plastic shear were investigated at different indentation depths. It was found that plastic shear occurs in bands, propagating through the crystal always starting at the contact point of the indenter. These propagating bands are explained by an increase of dislocations under the indent with increasing indentation depth. So a region with high strengthening under the indent becomes less favorable to plastic deformation and the material around this zone deforms preferable, resulting in the observed plastic shear bands.

- An investigation of the increments of plastic shear at an indentation depth of 2 µm revealed a fan shaped distribution of areas in which either one or two effective slip systems are active. This result of the numerical investigation in this work agrees well with the analytic results determined e.g. in

the work of Hill et al. (Hill et al. 1947), Johnson (Johnson 1985) and Saito (Saito and Kysar 2011; Saito et al. 2012).

Influence of the crystal orientation

- In opposite to the plane strain conditions in the midsection of the brick-shaped $[0\bar{1}0](101)$, out of plane strain was found in the $[123](11\bar{1})$ simulation.
- A comparison of the load-displacement curves, showed that the crystal indented in the [123] direction has a smaller resistance against the penetrating indenter than it has in the $[0\bar{1}0](101)$ orientation. This indicates, that the orientation of the slip systems in the $[123](11\bar{1})$ orientation enable an easier displacement of material under the indenter. This was confirmed by the comparison of the pile-up profiles of the indented surface which showed that overall more material piles-up at the surface as the crystal is indented in the [123] direction.

Influence of gradients of plastic shear

- More material piled-up at the surface of the specimen in the conventional CP simulation compared to the MBSGCP simulation. A comparison of the plastic shear on the resulting slip system 9/10 (causing mainly vertical shear and seen to be responsible for pile-up) along vertical paths under the piled-up material showed higher values in the MBSGCP simulation. This difference is seen to be the reason for the different pile-up profiles. A qualitative comparison of the distributions of plastic shear on the three effective slip systems and the slip system activity maps did not show a significant difference between the conventional and MBSG crystal plasticity simulations.
- The introduction of gradients of plastic shear does not violate the plane strain conditions in the single-layer model and a dependency of the shear stress solely on σ_{11}, σ_{22} and σ_{12} was found. A comparison between $(\sigma_{11}-\sigma_{22})/2$ and σ_{12} determined in the conventional and mechanism-based strain gradient crystal plasticity revealed much higher values in the MBSGCP

simulation. This can be explained by the occurrence of GNDs in the MBSGCP simulation that aggravate plastic deformation. In the displacement controlled simulation, this additional strengthening is compensated by an increase of the resolved shear stress, i.e. the driving force, which in turn makes higher stresses necessary.

- A study on g_{GND}, the contribution to hardening by GNDs, under the indent revealed a decrease of g_{GND} for increasing indentation depths, corresponding to decreasing gradients of plastic shear with increasing indentation depth. Thereby, the increase of the hardness with smaller indentation depths and a higher resistance against the penetration of the indenter can be explained.

- The influence of strain gradients on the lattice rotation and GND density turned out to be rather small. Only a small difference in a comparison between the conventional and MBSGCP simulation occurred. Since gradients of plastic shear do influence the occurring stresses severely but not the distribution and absolute values of plastic shear, it is only reasonable that the lattice rotation agrees well in the two simulations. Since gradients of plastic shear, i.e. additional hardening do not change the lattice rotation and GND density, a change of the hardening model in the conventional CP simulations can be assumed to cause no significant change, too.

Influence of non-Schmid effects

- Compared to the conventional and MBSGCP simulation, significantly more material pile-up at the surface of the specimen occurred in the non-Schmid simulation. The comparison of plastic shear on effective slip system 9/10, again along vertical paths under the piled-up material, revealed lower values in the non-Schmid than in the conventional simulation. In opposite to the higher values of plastic shear in the MBSGCP simulation that corresponded with less material pile-up, the non-Schmid effects lead to lower values of plastic shear along the paths and thus, more material pile-up occurs. The qualitative comparison of the distributions of plastic shear on the three effective slip systems between the conventional and

non-Schmid simulation showed significantly more plastic shear on slip system 9/10 in the vertical region under the indenter, while on slip system 2/12 and 5/8, no significant difference occurred. Consequently, non-Schmid effects must promote plastic shear mainly on the effective slip system 9/10 but not on slip system 2/12 and 5/8. The determined slip system activity map shows again a good qualitative agreement with the ones determined in the conventional and MBSG crystal plasticity simulation.

- Like in the first two simulations, non-Schmid effects did not influence the plane strain conditions in the midsection of the brick-shaped model. Thus, the stress state was studied in the same manner than in the conventional and MBSG crystal plasticity simulations. The result shows significantly lower occurring stresses under the indent. So, the non-Schmid effects lead to a facilitation of the deformability of the crystal. The same indicates the much lower load-displacement curve determined in the non-Schmid simulation in comparison to the conventional CP simulation.
- Regarding the study of the increments of plastic shear, it was found that the absolute values are higher in the non-Schmid simulation than in the conventional CP simulation. Propagating bands were found like in the conventional CP simulation. However, while they are slightly bend outward in the conventional CP simulation, they point downwards almost vertically in the non-Schmid simulation. Thus, the zone under the indent where severe strengthening occurs, changes its shape due to the non-Schmid effects. This is mainly because of the effective slip system 9/10 that is more active in the non-Schmid simulation under but not left and right of the indent. The plastic shear increment map determined in the non-Schmid simulation agrees well with the one determined in the conventional crystal plasticity simulation.
- The qualitative comparison of the overall distributions and values of in-plane rotation and density of geometrically necessary dislocation agrees well between the non-Schmid and conventional CP simulation. The small difference can be explained by the more active slip system 9/10.

Comparison of the numerical and experimental studies

- The comparison of experimental and numerical results regarding the deformed geometry of the indented bridge after the indentation agrees well. The comparison of the pile-up in the midsection of the bridge shows a good agreement between the conventional CP simulation and the experiment. Like in the simulations of the brick-shaped model, more material pile-up occurs in the non-Schmid simulation.

While crystal lattice rotation occurs right under the indenter tip in all simulations, no rotation was determined in the experiment. This disagreement may be caused by recrystallization i.e. the formation of subgrains under the indenter flanks which was not handled in the numerical simulations.

A Appendix

A.1 Shape functions and their derivatives

For both, the calculation of the plastic shear gradients and the determination of the Jacobian matrix for every element, the partially derivatives of the shape functions with respect to the local coordinates are needed. These derivatives are defined in the subroutine and listed in the following table 10 for the used C3D8 and C3D8R elements.

Table 10: Partially derived shape functions with respect to the local coordinates

i	$N_{i,\xi}$	$N_{i,\eta}$	$N_{i,\rho}$
1	$-\frac{1}{8}(1-\eta)(1-\rho)$	$-\frac{1}{8}(1-\xi)(1-\rho)$	$-\frac{1}{8}(1-\xi)(1-\eta)$
2	$\frac{1}{8}(1-\eta)(1-\rho)$	$-\frac{1}{8}(1+\xi)(1-\rho)$	$-\frac{1}{8}(1+\xi)(1-\eta)$
3	$\frac{1}{8}(1+\eta)(1-\rho)$	$\frac{1}{8}(1+\xi)(1-\rho)$	$-\frac{1}{8}(1+\xi)(1+\eta)$
4	$-\frac{1}{8}(1+\eta)(1-\rho)$	$\frac{1}{8}(1-\xi)(1-\rho)$	$-\frac{1}{8}(1-\xi)(1+\eta)$
5	$-\frac{1}{8}(1-\eta)(1+\rho)$	$-\frac{1}{8}(1-\xi)(1+\rho)$	$\frac{1}{8}(1-\xi)(1-\eta)$
6	$\frac{1}{8}(1-\eta)(1+\rho)$	$-\frac{1}{8}(1+\xi)(1+\rho)$	$\frac{1}{8}(1+\xi)(1-\eta)$
7	$\frac{1}{8}(1+\eta)(1+\rho)$	$\frac{1}{8}(1+\xi)(1+\rho)$	$\frac{1}{8}(1+\xi)(1+\eta)$
8	$-\frac{1}{8}(1+\eta)(1+\rho)$	$\frac{1}{8}(1-\xi)(1+\rho)$	$\frac{1}{8}(1-\xi)(1+\eta)$

Further the values of the shape functions and their derivatives at the integration points are necessary for the calculations. The local coordinates of integration points are listed in table 11 together with the local coordinates of the elements

nodes for C3D8 elements and exemplarily the values of the first, second and eights shape function at integration points. In the C3D8R element, solely one integration point exists at the local coordinates $\zeta = \eta = \rho = 0$.

Table 11: local coordinates of nodes and integration points within the C3D8 element together with the values of shape function 1, 2 and 8 at the eight integration points

IPT	ζ	η	ρ	N^1	N^2	...	N^8	*Node*	ζ	η	ρ
1	-0.577	-0.577	-0.577	0.490	0.131	…	0.035	1	-1.0	-1.0	-1.0
2	0.577	-0.577	-0.577	0.131	0.490	…	0.009	2	1.0	-1.0	-1.0
3	-0.577	0.577	-0.577	0.131	0.035	…	0.131	3	1.0	1.0	-1.0
4	0.577	0.577	-0.577	0.035	0.131	…	0.035	4	-1.0	1.0	-1.0
5	-0.577	-0.577	0.577	0.131	0.035	…	0.131	5	-1.0	-1.0	1.0
6	0.577	-0.577	0.577	0.035	0.131	…	0.035	6	1.0	-1.0	1.0
7	-0.577	0.577	0.577	0.035	0.009	…	0.490	7	1.0	1.0	1.0
8	0.577	0.577	0.577	0.009	0.035	…	0.131	8	-1.0	1.0	1.0

The values of derivatives of the eight shape functions are listed in the following table 12, exemplarily for the shape functions one and eight.

Table 12: Values of derivatives of shape functions 1 and 8 at the eight integration points

IPT	$N^1{}_{,\xi}$	$N^1{}_{,\eta}$	$N^1{}_{,\rho}$	...	$N^8{}_{,\xi}$	$N^8{}_{,\eta}$	$N^8{}_{,\rho}$
1	-0.311	-0.311	-0.311	…	-0.022	0.083	0.083
2	-0.311	-0.083	-0.083	…	-0.022	0.022	0.022
3	-0.083	-0.311	-0.083	…	-0.083	0.083	0.311
4	-0.083	-0.083	-0.022	…	-0.083	0.022	0.083
5	-0.083	-0.083	-0.311	…	-0.083	0.311	0.083
6	-0.083	-0.022	-0.083	…	-0.083	0.083	0.022
7	-0.022	-0.083	-0.083	…	-0.311	0.311	0.311
8	-0.022	-0.022	-0.022	…	-0.311	0.083	0.083

A.2 Common blocks and additional STATEV

Additional STATEVs were defined for the studies performed in this work. These contain the contribution to the current strength of a slip system caused by GNDs and the gradients of plastic shear in the x- y- and z-direction. The numbering of the additional STATEVs is listed in the following table 13.

Table 13: Additional STATEVs in the MBSGCP subroutine

STATEV(10*NSLPTL+2)- STATEV(11*NSLPTL+1)	Contribution to the current strength due to the geometrically necessary dislocations
STATEV(11*NSLPTL+2)- STATEV(12*NSLPTL+1)	Gradient of plastic shear in global x-direction
STATEV(12*NSLPTL+2)- STATEV(13*NSLPTL+1)	Gradient of plastic shear in global y-direction
STATEV(13*NSLPTL+2)- STATEV(14*NSLPTL+1)	Gradient of plastic shear in global z-direction

Furthermore, an overview of the needed user-defined common blocks necessary in the MBSGCP subroutine is shown in the following table 14 containing the common block names and a brief description of the contents:

Table 14: User-defined common blocks in the MBSGCP subroutine

GAMMAINT1	(global element number, number of slip system)	Contains all plastic shear values with the global element number at the unique integration point of an C3D8R element
NODELEM	(global element number, local node number)	Contains the elements in global numbering and the eight attached nodes in local numbering
NODEADJEL	(global node number)	Contains how often a unique node is shared by different elements
ALLGAMMA1	(global node number, number of slip system)	Contains the averaged value of plastic shear at all nodes in global numbering

COORDSK	(global node number, global coordinates)	Contains the three components of the global coordinates of nodes in global numbering

A.3 Characterization of crystal lattice rotation

For the characterization of the crystal lattice rotation, the initial values of the slip directions $\boldsymbol{s}^{\mathrm{i}}$ and slip plane normal $\boldsymbol{m}^{\mathrm{i}}$ are saved as additional solution-dependent state variables (SDV) and remain unchanged till the simulation end. The determination can be performed based on each of the twelve slip systems since all vectors undergo the same rotation at a material point. In this work, the first system was used for the calculations. A third vector $\boldsymbol{t}$ in the initial and current state defined by $\boldsymbol{t}^{\mathrm{i/c}} = |\boldsymbol{m}^{\mathrm{i/c}} \times \boldsymbol{s}^{\mathrm{i/c}}|$ is calculated in the subroutine and saved in the initial increment as SDV as well. All vectors are normalized for the calculation of the rotation matrix in every increment. The rotation matrix $\boldsymbol{R}$ can be determined by setting up the three equations (sum over *j* and *k*):

$$m_{\mathrm{j}}^{\mathrm{c}} = R_{\mathrm{jk}} m_{\mathrm{k}}^{\mathrm{i}} \tag{A.1}$$

$$s_{\mathrm{j}}^{\mathrm{c}} = R_{\mathrm{jk}} s_{\mathrm{k}}^{\mathrm{i}} \tag{A.2}$$

$$t_{\mathrm{j}}^{\mathrm{c}} = R_{\mathrm{jk}} t_{\mathrm{k}}^{\mathrm{i}}. \tag{A.3}$$

With these nine equations, the nine components R_{ij} of the rotation matrix can be calculated. Therefore, the matrix $\boldsymbol{A}$ is set up in the subroutine in the following form:

$$\boldsymbol{A} = \begin{pmatrix} m_1^{\mathrm{i}} & m_2^{\mathrm{i}} & m_3^{\mathrm{i}} \\ s_1^{\mathrm{i}} & s_2^{\mathrm{i}} & s_3^{\mathrm{i}} \\ t_1^{\mathrm{i}} & t_2^{\mathrm{i}} & t_3^{\mathrm{i}} \end{pmatrix}. \tag{A.4}$$

With the matrix $\boldsymbol{A}$, the following three expressions can be formulated:

$$\begin{pmatrix} m_1^{\mathrm{c}} \\ s_1^{\mathrm{c}} \\ t_1^{\mathrm{c}} \end{pmatrix} = \boldsymbol{A} \begin{pmatrix} R_{11} \\ R_{12} \\ R_{13} \end{pmatrix}, \begin{pmatrix} m_2^{\mathrm{c}} \\ s_2^{\mathrm{c}} \\ t_2^{\mathrm{c}} \end{pmatrix} = \boldsymbol{A} \begin{pmatrix} R_{21} \\ R_{22} \\ R_{23} \end{pmatrix}, \begin{pmatrix} m_3^{\mathrm{c}} \\ s_3^{\mathrm{c}} \\ t_3^{\mathrm{c}} \end{pmatrix} = \boldsymbol{A} \begin{pmatrix} R_{31} \\ R_{32} \\ R_{33} \end{pmatrix}. \tag{A.5}$$

By inverting the matrix $\boldsymbol{A}$, the components of the rotation matrix $\boldsymbol{R}$ can be determined.

A.4 Influence of the coefficient of friction

It is assumed that in all models used in this work the influence of friction is comparable and hence, the investigations on friction were performed on the basis of the single-layer model with mesh 2 and the $[0\bar{1}0]$ orientation. It was observed that the distortion of the elements in contact with the indenter and several layers of elements beneath are significantly influenced by the coefficient of friction. For a high coefficient, the lateral deformation of elements in contact with the indenter is restricted. For small values, massive lateral distortion was observed. The comparison of the first Euler angle, the indentation profiles and the load-displacement curves determined with different coefficients of friction show that the described effect influences the results significantly. The higher the coefficient of friction is chosen, the higher the load on the indenter is and the more material pile-up occurs. Furthermore, a significant increase of the first Euler angle appears as the coefficient of friction increases. The exact coefficient of friction is not known, however, a too low value leads to unrealistic distortion of elements under the indenter.

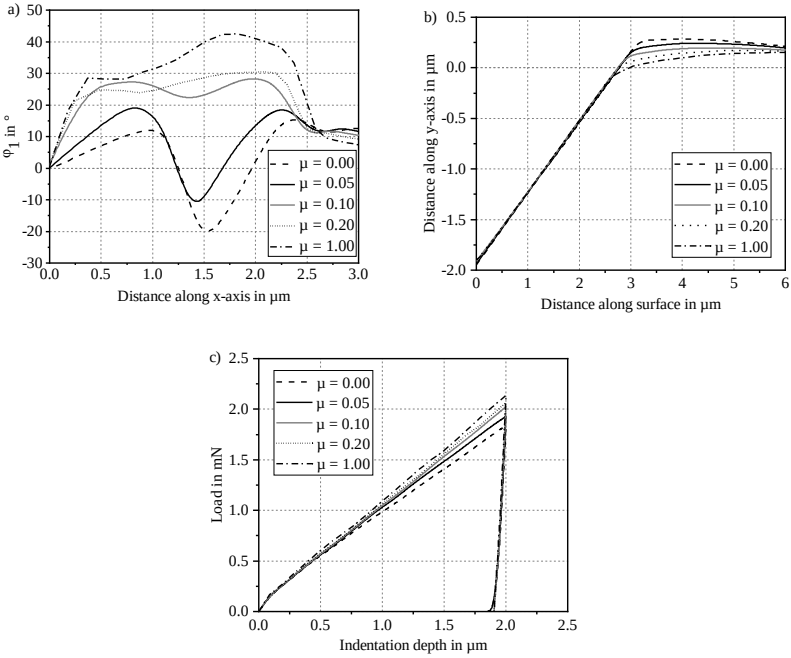

Figure 62: Influence of the coefficient of friction on in-plane lattice rotation, material pile-up and load-displcament curves in a), b) and c), repectively

A.5 Schmid-tensors of active slip systems

The Schmid-tensors of the six active slip systems in the midsection of the conventional CP simulation using the brick-shaped model are listed in the following:

$$\boldsymbol{P}^2 = \begin{pmatrix} -0.408 & 0.144 & -0.204 \\ 0.144 & 0.408 & -0.144 \\ -0.204 & -0.144 & 0.000 \end{pmatrix} \tag{A.6}$$

$$\boldsymbol{P}^{12}=\begin{pmatrix}-0.408 & 0.144 & 0.204\\ 0.144 & 0.408 & 0.144\\ 0.204 & 0.144 & 0.000\end{pmatrix} \tag{A.7}$$

$$\boldsymbol{P}^{5}=\begin{pmatrix}-0.408 & -0.144 & 0.204\\ -0.144 & 0.408 & -0.144\\ 0.204 & -0.144 & 0.000\end{pmatrix} \tag{A.8}$$

$$\boldsymbol{P}^{8}=\begin{pmatrix}0.408 & 0.144 & 0.204\\ 0.144 & -0.408 & -0.144\\ 0.204 & -0.144 & 0.000\end{pmatrix} \tag{A.9}$$

$$\boldsymbol{P}^{9}=\begin{pmatrix}0.000 & 0.289 & -0.408\\ 0.289 & 0.000 & 0.000\\ -0.408 & -0.000 & 0.000\end{pmatrix} \tag{A.10}$$

$$\boldsymbol{P}^{10}=\begin{pmatrix}0.000 & -0.289 & -0.408\\ -0.289 & 0.000 & 0.000\\ -0.408 & -0.000 & 0.000\end{pmatrix}. \tag{A.11}$$

A.6 Determination of effective slip systems

Slip systems 9 and 10 have the same slip plane but different slip directions. Simultaneous slip occurs along these slip directions ($\dot{\gamma}_s^9 = -\dot{\gamma}_s^{10}$). With these findings, slip systems 9 and 10 can be combined following the expression:

$$\boldsymbol{D}_s^{9/10} = \dot{\gamma}_s^9 \boldsymbol{P}_s^9 - \dot{\gamma}_s^{10} \boldsymbol{P}_s^{10}. \tag{A.12}$$

Again, the Schmid-tensor can be written in terms of $\boldsymbol{s}$ and $\boldsymbol{m}$:

$$\boldsymbol{D}_s^{9/10} = \frac{\dot{\gamma}_s^{9/10}}{2}[(\boldsymbol{s}^9 \otimes \boldsymbol{m}^9 + \boldsymbol{s}^9 \otimes \boldsymbol{m}^9) - (\boldsymbol{m}^{10} \otimes \boldsymbol{s}^{10} + \boldsymbol{m}^{10} \otimes \boldsymbol{s}^{10})]. \tag{A.13}$$

With the corresponding slip plane normals but the different slip directions of slip system 9 and 10 the equation can be simplified to determine the

resulting rate of stretching caused by the combination of corresponding slip systems 2 and 10:

$$\boldsymbol{D}_{\mathrm{s}}^{9/10} = \frac{\dot{\gamma}_{\mathrm{s}}^{9/10}}{2}[\boldsymbol{m}^{9} \otimes (\boldsymbol{s}^{9} - \boldsymbol{s}^{10}) + (\boldsymbol{s}^{9} - \boldsymbol{s}^{10}) \otimes \boldsymbol{m}^{9}]. \tag{A.14}$$

The slip systems 5 and 8 have the same slip direction but different slip planes and again simultaneous slip occurs on the two slip systems ($\dot{\gamma}_s^5 = -\dot{\gamma}_s^8$):

$$\boldsymbol{D}_{\mathrm{s}}^{5/8} = \dot{\gamma}_{\mathrm{s}}^{5}\boldsymbol{P}_{\mathrm{s}}^{5} - \dot{\gamma}_{\mathrm{s}}^{8}\boldsymbol{P}_{\mathrm{s}}^{8}. \tag{A.15}$$

With the expression for the Schmid-tensor, the equation for the calculation of the rate of stretching can be determined:

$$\boldsymbol{D}_{\mathrm{s}}^{5/8} = \frac{\dot{\gamma}_{\mathrm{s}}^{5/8}}{2}[(\boldsymbol{s}^{5} \otimes \boldsymbol{m}^{5} + \boldsymbol{s}^{5} \otimes \boldsymbol{m}^{5}) - (\boldsymbol{m}^{8} \otimes \boldsymbol{s}^{8} + \boldsymbol{m}^{8} \otimes \boldsymbol{s}^{8})]. \tag{A.16}$$

Consequently, the expression to calculate the rate of stretching $\boldsymbol{D}$ gives:

$$\boldsymbol{D}_{\mathrm{s}}^{5/8} = \frac{\dot{\gamma}_{\mathrm{s}}^{5/8}}{2}[\boldsymbol{s}^{5} \otimes (\boldsymbol{m}^{5} - \boldsymbol{m}^{8}) + (\boldsymbol{m}^{5} - \boldsymbol{m}^{8}) \otimes \boldsymbol{s}^{5}]. \tag{A.17}$$

A.7 Numbering of slip systems in CP and NOSCP subroutine

Per definition, there are 24 slip systems in the non-Schmid model implemented. Always two of the 24 slip systems are corresponding slip system with the same slip plane and slip direction that point however, in the opposite direction. This means that each two corresponding slip systems have the same

Schmid-tensor but with different sign. For a comparison of the 24 slip systems in the non-Schmid model and the twelve slip systems in the conventional CP model, each two slip systems with collinear slip directions in the non-Schmid simulation were combined for the investigation of the slip system activities. For every slip system in the conventional crystal plasticity, two corresponding slip systems can be found in the non-Schmid subroutine. For some slip systems, the defined slip plane normal in the non-Schmid simulation is defined in the opposite direction than in the conventional simulation. This leads to different signs in the Schmid-tensors. However, the definition of the slip plane normal does not influence the simulation results. For the comparison of the results, the internal numbering of slip systems as defined in the conventional crystal plasticity simulation is used and the corresponding slip systems in the non-Schmid simulation are renumbered to match the conventional CP numbering. In the following, e.g. slip system 2 from the conventional CP is compared to renumbered slip system 2^{NoS+}+2^{NoS-}. The + defines the non-Schmid slip system with the same slip direction than the slip system from the conventional simulation and – the corresponding slip system with opposite slip direction. A summary of the corresponding slip systems is given in the following table 15. For both, the non-Schmid and conventional crystal plasticity simulation, plastic shear on six of the twelve slip systems is either zero or very small in comparison to the slip systems that are considered active. These slip systems are not shown in the table.

Table 15: Numbering of active slip systems in the conventional and non-Schmid crystal plasticity simulation

conventional CP numbering	non-Schmid numbering	non-Schmid renumbered
2^{S}	7^{NoS}	2^{NoS+}
	19^{NoS}	2^{NoS-}
5^{S}	6^{NoS}	5^{NoS+}
	18^{NoS}	5^{NoS-}
8	5^{NoS}	8^{NoS+}
	17^{NoS}	8^{NoS-}
9	2^{NoS}	9^{NoS-}
	14^{NoS}	9^{NoS+}

10	10^{NoS}	10^{NoS+}
	22^{NoS}	10^{NoS-}
12	9^{NoS}	12^{NoS-}
	21^{NoS}	12^{NoS+}

A.8 Element size study

To ensure that the results of the simulations are independent on the element size, the single-layer model was discretized with three different meshes. The results regarding the pile-up, load-displacement and crystal lattice rotation were compared. Three meshes, namely mesh 1, mesh 2 and mesh 3, consisting of 1330, 2378 and 10698 linear hexahedral elements of type C3D8R. The smallest element sizes under the indent in the contact region were 300 nm × 300 nm, 100 nm × 100 nm and 33 nm × 33 nm, for the three meshes respectively.

Figure 63 shows the results for the calculated first Euler angel φ_1 representing in-plane lattice rotation in the single-layer model, along a path emanating from the indenter axis to the right about 0.6 µm underneath the surface of the specimen in a) and the indented surface profile after unloading in b), both for the three different meshes. The maximum value along the path is larger in the region between 0 µm and 0.5 µm in the simulation with mesh 1. The overall shapes of regions where lattice rotation occurs and the maximum values are similar for all three meshes. Both, mesh 2 and mesh 3, lead to a similar surface profile. However, the profile in the simulation using mesh 1 is slightly lower. The reason is that the larger elements in the region where contact stops cannot resolve the exact profile as determined with mesh 2 and mesh 3. Figure 63 c) shows the load-displacement curves determined with the three different meshes. Again, just like in the comparison of the indentation profiles, mesh 2 and mesh 3 lead to similar results. The curve determined with mesh 1 exhibits a yattering shape. This is caused by the large elements and their nodes respectively, increasing the reaction force on the indenter suddenly as they make contact with the surface of the indenter.

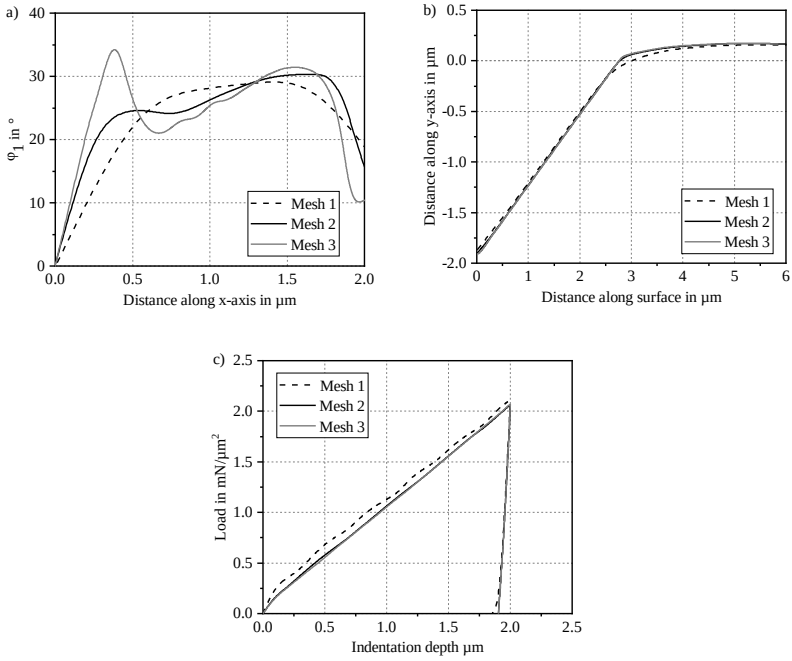

Figure 63: First Euler angel φ_1 along the path 600 nm underneath the surface of the specimen, material pile-up profiles of the indented surface after fully unloading and load-displacement curves in a), b) and c). All figures show the comparison of the three different meshes

The comparison induces that the coarsest mesh tends to be not suitable for the investigations. The simulations with mesh 2 and mesh 3 determine similar results. However, due to the significantly lower computational effort, mesh 2 is used for the investigations using the single-layer model in this work.

A.9 Influence of the number of layers in the brick-shaped model

Beside the element size in the midsection, the number of elements in the global z-direction may influence the simulation results in the brick-shaped model and was therefore investigated. Three models with the same mesh (corresponding to mesh 2 used in the single-layer model) in the global x-y-plane but with a different amount of elements in the z-direction, namely eight, twelve and 16 elements were used for the simulations and the three Euler angles, the material pile-up and the load-displacement curves were compared. For the $[0\bar{1}0]$ orientation, the number of elements in the z-direction can be assumed negligible due to the plane strain conditions and so the investigations were carried out for the brick-shaped model and the [123] orientation. Since no plane strain conditions occur in the midsection of the simulations of the [123] indented crystal, all three angles were evaluated and compared along the path 600 nm under the specimen's surface. It was found that neither the Euler angles nor the indentation profiles or load-displacement curves are influenced by the number of elements and therefore, the results are not shown here. To keep computational time as low as possible, eight elements were defined in the global z-direction in all simulations of the brick-shaped model.

A.10 Influence of wideness of the brick-shaped model

It was found, that a minimum thickness of the brick-shaped model is necessary for plane strain conditions, i.e. in-plane lattice rotation in the midsection. The evaluation of the three Euler angles for the [123] orientation, again along the path 600 nm under the surface, shown in figure 64, reveals a derivation of the angles for a wideness *w* of the specimen smaller than 50 µm. The comparison of the indentation profiles in figure 65 shows a decrease of material pile-up with decreasing wideness of the specimen. A lower profile was determined for the 50 µm wide specimen. For a wideness of 30 µm, an even more significant lower profile was determined. Consequently, the brick-shaped model for the studies in this work has to have a wideness of 70 µm.

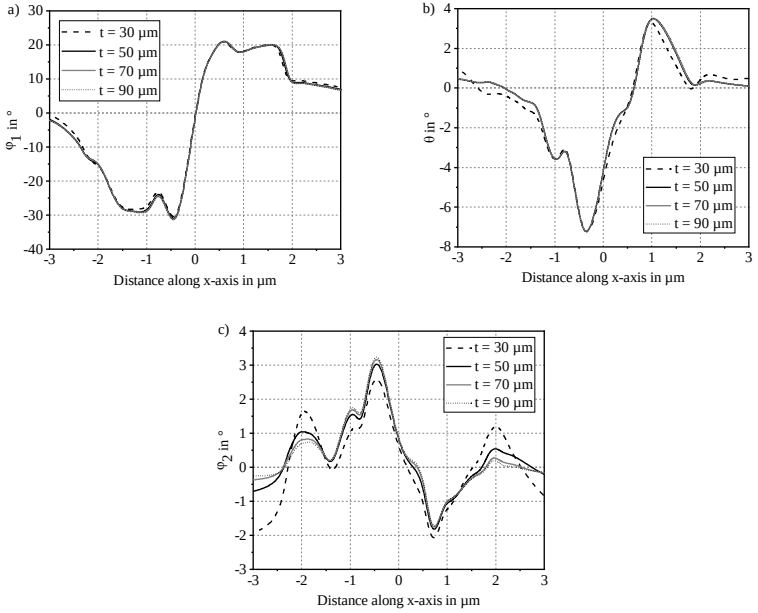

Figure 64: Comparison of the three Euler angles φ_1, Φ and φ_2 along the path about 600 nm under the indented surface after unloading in the brick-shaped model in a), b) and c)

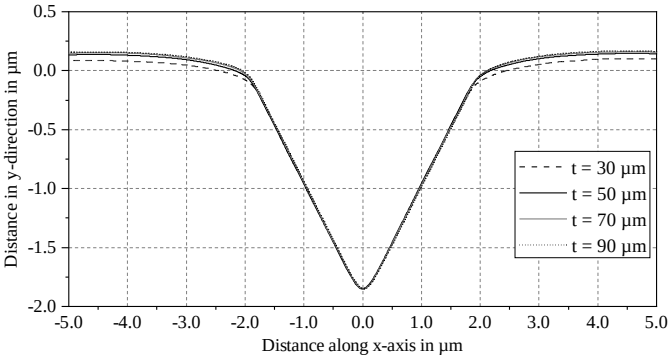

Figure 65: Comparison of the surface profiles of the indented specimens with the 30 µm, 50 µm, 70 µm and 90 µm wideness of the brick-shaped model after unloading

Publication bibliography

Alder, B. J.; Wainwright, T. E. (1959): Studies in molecular dynamics. I. general method. In *The Journal of Chemical Physics* 31 (2), pp. 459–466. DOI: 10.1063/1.1730376.

Arsenlis, A.; Cai, W.; Tang, M.; Rhee, M.; Oppelstrup, T.; Hommes, G. et al. (2007): Enabling strain hardening simulations with dislocation dynamics. In *Modelling and Simulation in Materials Science and Engineering* 15 (6), pp. 553–595.

Arsenlis, A.; Parks, D. M. (1999): Crystallographic aspects of geometrically-necessary and statistically-stored dislocation density. In *Acta Materialia* 47 (5), pp. 1597–1611.

Asaro, J.; Needleman, A. (1989): Texture development and strain hardening in rate-depednent face-centered cubic polycrystalls: correlation of micro- and macromechanics. In *Philosophical Transactions of the Royal Society of London. Series A, Mathematical and Physical Sciences* 328 (1600), pp. 443–500.

Asaro, R. J.; Rice, J. R. (1977): Strain localization in ductile single crystals. In *J. Mech. Phys. Solids* 25, pp. 309–338.

Ashby, M. F. (1970): The deformation of plastically non-homogeneous materials. In *The Philosophical Magazine: A Journal of Theoretical Experimental and Applied Physics* 21 (170), pp. 399–424. DOI: 10.1080/14786437008238426.

Atkinson, M. (1995): Further analysis of the size effect in indentation hardness tests of some metals. In *Journal of Materials Research* 10 (11), pp. 2908–2915.

Bassani, J. L. (2001): Incompatibility and a simple gradient theory of plasticity. In *J. Mech. Phys. Solids* 49 (9), pp. 1983–1996.

Bathe, K.-J. (1996): Finite Element Procedures. Englewood Cliffs, NJ: Prentice Hall.

Berkovich, E. S. (1951): Three-faceted diamond pyramid for micro-hardness testing. In *Ind. Diamond Rev.* 11 (127), pp. 129–133.

Borst, R.; Mühlhaus, H. (1992): Gradient-dependent plasticity: Formulation and algorithmic aspects. In *International Journal for numerical methods in engineering* 35, pp. 521–539.

Busso, E. P.; Meissonnier, F. T.; O'Dowd, N. P. (2000): Gradient-dependent deformation of two-phase single crystals. In *Journal of the Mechnics and Physics of Solids* 48 (11), pp. 2333–2361.

Christian, J. W. (1983): Some surprising features of the plastic deformation of body-centered cubic metals and alloys. In *Metallurgical Transactions A* 14 (7), pp. 1237–1256.

Dahlberg, C. F. O.; Saito, Y.; öztop; M. S.; Kysar, J. W. (2014): Geometrically necessary dislocation density measurements associated with different angles of indentations. In *International Journal of Plasticity* 54, pp. 81–95.

Dassault Systèmes: Abaqus. Available online at https://www.3ds.com/de/produkte-und-services/simulia/produkte/abaqus/, checked on 5/5/2020.

Demiral, M. (2012): Enhanced gradient crystal-plasticity study of size effects in B.C.C. metal. Dissertation. Loughborough University, Loughborough. Available online at https://repository.lboro.ac.uk/articles/Enhanced_gradient_crystal-plasticity_study_of_size_effects_in_B_C_C_metal/9541319.

Demiral, M.; Roy, A.; El Sayed, T.; Silberschmidt, V. V. (2014): Influence of strain gradients on lattice rotation in nanoindentation experiments: A numerical study. In *Materials Science and Engineering A* 608, pp. 73–81.

Demiral, M.; Roy, A.; Silberschmidt, V. V. (2013): Indentation studies in b.c.c. crystals with enhanced model of strain-gradient crystal plasticity. In *Computational Materials Science* 79, pp. 896–902.

Duesbery, M. S. (1984): On non-glide stresses and their influence on the screw dislocation core in body-centred cubic metals I. The Peierls stress. In *Proceedings of the Royal Society of London. Series A, Mathematical and Physical Sciences* 392 (1802), pp. 175–187.

Duesbery, M. S.; Vitek, V. (1998): Plastic anisotropy in b.c.c. transition metals. In *Acta Materialia* 46 (5), pp. 1481–1492.

Engineering ToolBox (2004): Friction and Friction Coefficients for various Materials. Available online at https://www.engineeringtoolbox.com/friction-coefficients-d_778.html, checked on 3/20/2020.

Fischer-Cripps, A. (2011): Nanoindentation. New York, Dordrecht, Heidelberg, London: Springer.

Fleck, N. A.; Hutchinson, J. W. (1993): A phenomenological theory for strain gradient effects in plasticity. In *J. Mech. Phys. Solids* 41 (12), pp. 1825–1857.

Fleck, N. A.; Hutchinson, J. W. (1997): Strain gradient plasticity. In *Advances in Applied Mechanics* 33, pp. 295–361.

Fleck, N. A.; Hutchinson, J. W. (2001): A reformulation of strain gradient plasticity. In *Journal of the Mechnics and Physics of Solids* 49 (10), pp. 2245–2271.

Fleck, N. A.; Muller, G. M.; Ashby, M. F.; Hutchinson, J. W. (1994): Strain gradient plasticity: theory and experiments. In *Acta Metallurgica et Materialia* 42 (2), pp. 475–487.

Gao, H.; Huang, Y.; Nix, W. D.; Hutchinson, J. W. (1999): Mechanism-based strain gradient plasticity - I. Theory. In *Journal of the Mechnics and Physics of Solids* 47 (6), pp. 1239–1263.

Gerday, A. F.; Bettaieb, M. B.; Duchene, L.; Clement, N.; Diarra, H.; Habraken, A. M. (2009): Interests and limitations of nanoindentation for bulk multiphase material identification: Application to the b phase of Ti-5553. In *Acta mater.* 57 (17), pp. 5186–5195.

Ghoniem, N. M.; Tong, S. H.; Sun, L. Z. (2000): Parametric dislocation dynamics: A thermodynamics-based approach to investigations of mesoscopic plastic deformation. In *Phys Ref B* 61 (2), pp. 913–927.

Gottstein, G. (2014): Materialwissenschaften und Werkstofftechnik. Physikalische Grundlagen. Berlin, Heidelberg: Springer.

Gröger, R.; Bailey, A. G.; Vitek, V. (2008a): Multiscale modeling of plastic deformation of molybdenumand tungsten: I. Atomistic studies of the core structureand glide of 1/2h111iscrew dislocations at 0 K. In *Acta Materialia* (56), pp. 5401–5411.

Gröger, R.; Racherla, V.; Bassani, J. L.; Vitek, V. (2008b): Multiscale modeling of plastic deformation of molybdenum and tungsten: II. Yield criterion for single crystals based on atomistic studies of glide of 1/2<111> screw dislocations. In *Acta Materialia* (56), pp. 5412–5425.

Gröger, R.; Vitek, V. (2008): Multiscale modeling of plastic deformation of molybdenumand tungsten. III. Effects of temperature and plastic strain rate. In *Acta Materialia* (56), pp. 5426–5439.

Guzman, M.; Neubauer, G.; Flinn, P.; Nix, W. D. (1993): The role of indentation depth on the measured hardness of materials. In *MRS Proceedings* 308, pp. 613–618. DOI: 10.1557/PROC-308-613.

Han, C.; Gao, H.; Huang, Y.; Nix, W. (2005): Mechanism-based strain gradient crystal plasticity - I. Theory. In *Journal of the Mechnics and Physics of Solids* 53 (5), pp. 1188–1203.

Hielscher, R.; Mainprice, D.; Bachmann, F.; Kilian, R.; Bartel, F.; Johneson, O.; Sorensen, B. E.: MTEX toolbox. Available online at https://mtex-toolbox.github.io/download, checked on 3/20/2020.

Hill, R. A.; Lee, E. H.; Tupper, S. J. (1947): The theory of wedge indentation of ductile materials. In *Proc. R. Soc. Lond. A* 188 (1013), pp. 273–289. DOI: 10.1098/rspa.1947.0009.

Hill, R. A.; Rice, J. R. (1972): Constitutive analysis of elastic-plastic crystals at arbitrary strains. In *J. Mech. Phys. Solids* 20 (6), pp. 401–413.

Huang, Y. (1991): A user-material subroutine incorporating single crystal plasticity in the ABAQUS finite element program. In *Report Mech 178, Div. Applied Science, Harvard, Cambridge (MA)*. Available online at http://www.columbia.edu/~jk2079/Kysar_Research_Laboratory/Single_Crystal_UMAT.html, checked on 5/5/2020.

Huang, Y.; Gao, H.; Nix, W. D.; Hutchinson, J. W. (2000a): Mechanism-based strain gradient plasticity—II. Analysis. In *Journal of the Mechanics and Physics of Solids* 53 (5), pp. 99–128.

Huang, Y.; Qu, S.; Hwang, K. C.; Li, M.; Gao, H. (2004): A conventional theory of mechanism-based strain gradient plasticity. In *International Journal of Plasticity* 20 (4-5), pp. 753–782.

Huang, Y.; Xue, Z.; Gao, H.; Nix, W. D.; Xia, Z. C. (2000b): A study of microindentation hardness tests by mechanism-based strain gradient plasticity. In *Journal of Materials Research* 15 (8), pp. 1786–1796.

Johnson, K. L. (1985): Contact Mechanics. Cambridge: Cambridge University Press.

Knoop, F.; Peters, C. G.; Emerson, W. B. (1939): A sensitive pyramidal-diamond tool for indentation measurements. In *Research Paper 1220, Journal of Research, National Bureau of Standards* 23.

Kords, C. (2013): On the role of dislocation transport in the constitutive description of crystal plasticity. Dissertation. RWTH, Aachen. Fakultät für Georessourcen und Materialtechnik.

Kubin, L. P.; Canova, G.; Condat, M.; Devincre, B.; Pontikis, V.; Bréchet, Y. (1992): Dislocation microstructures and plastic flow: A 3D simulation. In *Solid State Phenomena* 23, pp. 455–472.

Kysar, J. W. (1997): Addendum to "A user-material subroutine incorporating single crystal plasticity in the ABAQUS finite element program". Available online at http://www.columbia.edu/~jk2079/Kysar_Research_Laboratory/Single_Crystal_UMAT.html, checked on 3/20/2020.

Lee, E. H. (1969): Elastic-plastic deformation at finite strains. In *Journal of Applied Mechanics* 36 (1), pp. 1–6.

Lee, W. B.; Chen, Y. P. (2010): Simulation of micro-indentation hardness of FCC single crystals by mechanism-based strain gradient crystal plasticity. In *International Journal of Plasticity* 26 (10), pp. 1527–1540.

Lewandowski, M. J.; Stupkiewiez, S. (Eds.) (2018a): Modelling of wedge indentation using gradient-enhanced crystal-plasticity model. 41st Solid Mechanics Conference. Warschau, Poland, August 27-31. Available online at http://solmech2018.ippt.pan.pl/downloads.html, checked on 5/5/2020.

Lewandowski, M. J.; Stupkiewiez, S. (2018b): Size effects in wedge indentation predicted by a gradient-enhanced crystal-plasticity model. In *International Journal of Plasticity* 109, pp. 54–78.

Li, H.; Ghosh, A.; Han, Y. H.; Bradt, R. C. (1993): The frictional component of the indentation size effect in low load microhardness testing. In *Journal of Materials Research* 8 (5), pp. 1028–1032. DOI: 10.1557/JMR.1993.1028.

Liang, H.; Dunne, F.P.E. (2009): GND accumulation in bi-crystal deformation: Crystal plasticity analysis and comparison with experiments. In *International Journal of Material Sciences* 51 (4), pp. 326–333.

Linsmeier, Ch.; Rieth, M.; Aktaa, J.; Chikada, T.; Hoffmann, A.; Hoffmann, J. et al. (2017): Development of advanced high heat flux and plasma-facing materials. In *Nuclear Fusion* 57 (9), pp. 2–60.

Liu, M.; Lu, C.; Tieu, K. A.; Peng, C.; Kong, C. (2015): A combined experimental numerical approach for determining mechnical properties of aluminium subjects to nanoindentation. In *Scientific Reports* 5 (15072).

Liu, Y.; Zhou, H.; Zhang, Y.; Jin, S.; Lu, G. (2009): The ideal tensile strength and deformation behavior of a tungsten single crystal. In *Nuclear Instruments and Materials in Physics Research Section B: Beam Interactions with Materials and Atoms* 267 (18), pp. 3282–3285.

Ma, Q.; Clarke, D. R. (1995): Size dependent hardness of silver single crystals. In *Journal of Materials Research* 10 (4), pp. 853–863.

Marx, D.; Hutter, J. (2000): Ab initio molecular dynamics: Theory and Implementation. In *Publication Series of the John von Neumann Institute for Computing* 3 (1), 329-477.

MathWorks: Matlab. Version R2016a. Natic, Massachusetts, United States. Available online at https://www.mathworks.com/products.html?s_tid=gn_ps, checked on 5/5/2020.

McElhaney, K. W.; Vlassak, J. J.; Nix, W. D. (1998): Determination of indenter tip geometry and indentation contact area for depth-sensing indentation experiments. In *Journal of Materials Research* 13 (5), pp. 1300–1306. DOI: 10.1557/JMR.1998.0185.

Meissonnier, F. T.; Busso, E. P.; O'Dowd, N. P. (2001): Finite element implementation of a generalised non-local rate-dependent crystallographic formulation for finite strains. In *International Journal of Plasticity* 17 (4), pp. 601–640.

Niordson, C. F.; Hutchinson, J. W. (2003): On lower order strain gradient plasticity theories. In *European Journal of Mechanics A/Solids* 22 (6), pp. 771–778.

Nix, W. D. (1989): Mechanical properties of thin films. In *Materials Transactions* 20, pp. 2217–2245.

Nix, W. D. (1997): Elastic and plastic properties of thin films on substrates: nanoindentation techniques. In *Materials Science and Engineering A* 234-236, pp. 37–44.

Nix, W. D.; Gao, H. (1998): Indentation size effect in crystalline materials: a law for strain gradient plasticity. In *J. Mech. Phys. Solids* 46 (3), pp. 411–425.

Nye, J. F. (1953): Some geometrical relations in dislocated crystals. In *Acta Metallurgica* 1 (2), pp. 153–162.

Oliver, W.; Pharr, G. M. (1992): An improved technique for determining hardness and elastic modulus using load and displacment sensing indentation experiments. In *J. Mater. Res.* 7 (6), pp. 1564–1583.

Oliver, W.; Pharr, G. M. (2004): Measurement of hardness and elastic modulus by instrumented indentation: Advances in understanding and refinements to methodology. In *J. Mater. Res.* 19 (1), 3-20.

Peirce, D.; Asaro, J.; Needleman, A. (1983): Material rate dependency and localized deformation in crystalline solids. In *Acta Metallurgica* 31 (12), pp. 1951–1976.

Peirce, D.; Asaro, R. J.; Needleman, A. (1982): An analysis of non-uniform and localized deformation in ductile single crystals. In *Acta Metallurgica* 30 (6), pp. 1087–1119.

Pethica, J.; Oliver, W. (1988): Mechanical properties of nanometre volumes of material: use of the elastic response of small area indentations. In *MRS Proceedings* 130 (13), pp. 16–23.

Pharr, G. M. (1998): Measurement of mechanical properties by ultra-low load indentation. In *Materials Science and Engineering: A* 253 (1-2), pp. 151–159.

Pharr, G. M.; Bolshakov, A. (2002): Understanding nanoindentation unloading curves. In *J. Mater. Res.* 17 (10), pp. 2660–2671.

Pharr, G. M.; Oliver, W. (1991): On the generality of the relationship among contact stiffness, contact area, and elastic modulus during indentation. In *J. Mater. Res.* 7 (3), pp. 613–617.

Poole, W. J.; Ashby, M. F.; Fleck, N. A. (1996): Micro-hardness of annealed and work-hardened copper polycrystals. In *Scripta Materialia* 34 (4), pp. 559–564.

Qu, S.; Nix, W. D.; Jiang, H. (2004): Indenter tip radius effect on the Nix–Gao relation in micro- and nanoindentation hardness experiments. In *J. Mater. Res.* 19 (11), pp. 3423–3434.

Reuber, C.; Eisenlohr, P.; Roters, F.; Raabe, D. (2014): Dislocation density distribution around an indent in single-crystalline nickel: Comparing nonlocal crystal plasticity finite-element predictions with experiments. In *Acta Materialia* 71, pp. 333–348.

Rice, J. R. (1971): Inelastic constitutive relations for solids: an internal-variable theory and its application to metal plasticity. In *J. Mech. Phys. Solids* 19 (6), pp. 433–455.

Rice, J. R. (1987): Tensile Crack Tip Fields in Elastic-Ideally Plastic Crystals. In *Mechanics of Materials* 6, pp. 317–335.

Roters, F.; Eisenlohr, P.; Hantcherli, L.; Tiahjanto, D. D.; Bieler, T. R.; Raabe, D. (2010): Overview of constitutive laws, kinematics, homogenization andmultiscale methods in crystal plasticity finite-element modeling:Theory, experiments, applications. In *Acta Materialia* 58 (4), pp. 1152–1211.

Saito, Y.; Kysar, J. W. (2011): Wedge indentation into elastic–plastic single crystals, 1: Asymptotic fields for nearly-flat wedge. In *International Journal of Plasticity* 27 (10), pp. 1640–1657.

Saito, Y.; Öztop, M. S.; Kysar, J. W. (2012): Wedge indentation into elastic–plastic single crystals. 2: Simulations for face-centered cubic crystals. In *International Journal of Plasticity* 28 (1), pp. 70–87.

Schmid, E. (1924): Zn-normal stress law. In *Proceedings International Congress of Applied Mechanics. Delft*, p. 342.

Schwarz, K. W. (1999): Simulation of dislocations on the mesoscopic scale. I. Methods and examples. In *Journal of Applied Physics* 85 (108), pp. 108–119.

Siddiq, A.; Schmauder, S.; Huang, Y. (2007): Fracture of bicrystal metal/ceramic interfaces: A study via the mechanism-based strain gradient crystal plasticity theory. In *International Journal of Plasticity* 23 (4), pp. 665–689.

Sills, R. B.; Kuykendall, W. P.; Aghaei, A.; Cai, W. (2016): Fundamentals of dislocation dynamics simulations. In *Multiscale materials modeling for nanomechanics* 245, pp. 53–87.

Stanford University (1995): Fortran 77 Tutorial. Available online at https://web.stanford.edu/class/me200c/tutorial_77/13_common.html, checked on 3/20/2020.

Stelmashenko, N. A.; Walls, M. G.; Brown, L. M.; Milman, YU.V. (1993): Microindentations on W and Mo oriented single crystals: an ATM study. In *Acta Metallurgica et Materialia* 41 (10), pp. 2855–2865.

Swadener, J. G.; George, E. P.; Pharr, G. M. (2002): The correlation of the indentation size effect measured with indenters of various shapes. In *Journal of the Mechanics and Physics of Solids* 50 (4), pp. 681–694.

Taylor, G. (1938): Plastic strain in metals. In *J. Inst. Met.* 62, pp. 307–324.

The SciPy community (2019): scipy.interpolate.griddata. Available online at https://docs.scipy.org/doc/scipy/reference/generated/scipy.interpolate.griddata.html, checked on 3/20/2020.

Vitek, V. (2004): Core structure of screw dislocations in body-centred cubic metals: relation to symmetry and interatomic bonding. In *Philosophical Magazine A* 84 (3-5), pp. 415–428.

Volz, T.; Schwaiger, R.; Wang, J.; Weygand, S. M. (2017): Comparison of three approaches to determine the projected area in contact from finite element Berkovich nanoindentation simulations in tungsten. In *IOP Conf. Ser.: Mater. Sci. Eng.* 257, p. 12013.

Volz, T.; Schwaiger, R.; Wang, J.; Weygand, S. M. (2018): Numerical study of slip system activity and crystal lattice rotation under wedge nanoindents in tungsten single crystals. In *AIP Conference Proceedings* 1960, p. 170017. DOI: 10.1063/1.5035074.

Wang, Y.; Raabe, D.; Klüber, C.; Roters, F. (2004): Orientation dependence of nanoindentation pile-up patterns and of nanoindentation microtextures in

copper single crystals. In *Acta Materialia* 52 (8), pp. 2229–2238. DOI: 10.1016/j.actamat.2004.01.016.

Weinberger, C. R.; Battaile, C. C.; Buchheit, T. E.; Holm, E. A. (2012): Incorporating atomistic data of lattice friction into BCC crystal plasticity models. In *International Journal of Plasticity* 37, pp. 16–30.

Weygand, D.; Friedman, L. H.; van der Giessen, E.; Needleman, A. (2002): Aspects of boundary-value problem solutions with three-dimensional dislocation dynamics. In *Modell Simul Mater Sci Eng* 10 (4), pp. 437–468.

Yao, W. (2012): Crystal plasticity study of single crystal tungsten by indentation tests. Dissertation. University of Ulm.

Yefimov, S.; van der Giessen, E. (2005): Size effects in single crystal thin films:nonlocal crystal plasticity simulations. In *European Journal of Mechanics A/Solids* 24 (2), pp. 183–193.

Zahedi, A.; Demiral, M.; Roy, A.; Babitsky, V.; Silberschmid, V. (2012): Indentation in f.c.c. single crystals. In *Solid State Phenomena* 188, pp. 219–225.

Zambaldi, C.; Raabe, D. (2010): Plastic anisotropy of γ-TiAl revealed by axisymmetric indentation. In *Acta Materialia* 58 (9), pp. 3516–3530.

Zbib, H. M.; Rhee, M.; Hirth, J. P. (1998): On plastic deformation and the dynamics of 3D dislocations. In *Int. J. Mech. Sci.* 40 (2-3), pp. 113–127.

Danksagung

An dieser Stelle möchte ich mich bei allen Personen und Institutionen bedanken, die mir das Erstellen dieser Arbeit ermöglicht haben.

Mein besonderer Dank gilt Frau Prof. Dr. Sabine Weygand, Frau Prof. Dr. Ruth Schwaiger, Herr Prof. Dr. Marc Kamlah und nicht zuletzt Herr Prof. Dr. Oliver Kraft für die ausgezeichnete Betreuung und Unterstützung bei der Durchführung der gesamten Arbeit.

Für die vielen, nicht immer nur fachlichen und organisatorischen Diskussionen, bedanke ich mich bei meinen Kollegen Simon Müller, Kai Stadtmüller (nicht nur für die IT Unterstützung), Mona Gierl und vor allem bei meiner Projektpartnerin Jin Wang.

Außerdem möchte ich mich bei der Hochschule Karlsruhe, dem Institut für Angewandte Materialwissenschaften am KIT und dem Ministerium für Wissenschaft, Forschung und Kunst Baden-Württemberg für die Finanzierung meiner Arbeit und dem Ermöglichen meiner Konferenzteilnahmen vielmals bedanken.

Nicht zuletzt gilt mein Dank der Unterstützung durch meine Frau Kerstin Volz, meiner Familie und all meinen Freunden.

List of publications

Volz, T.; Schwaiger, R.; Wang, J.; Weygand, S. M. (2017): Comparison of three approaches to determine the projected area in contact from finite element Berkovich nanoindentation simulations in tungsten. In *IOP Conf. Ser.: Mater. Sci. Eng.* 257, p. 12013.

Volz, T.; Schwaiger, R.; Wang, J.; Weygand, S. M. (2018): Numerical study of slip system activity and crystal lattice rotation under wedge nanoindents in tungsten single crystals. In *AIP Conference Proceedings* 1960, p. 170017. DOI: 10.1063/1.5035074.

Volz, T.; Schwaiger, R.; Wang, J.; Weygand, S. M. (2018): Numerical studies of crystal lattice rotation and pile-up patterns during nanoindentation of tungsten single crystals. In Forschung aktuell 2018, pp. 48-51